Revisiting Unsolved Mysteries: A Journey Into Bulk and Surface Characteristics of Samarium Hexaboride Using Transport Measurements

by

Alexa Isabel Rakoski Mihaliov

A dissertation submitted in partial fulfillment
of the requirements for the degree of
Doctor of Philosophy
(Physics)
in the University of Michigan
2021

Doctoral committee:
Professor Cagliyan Kurdak, Chair
Assistant Professor Elaheh Ahmadi
Professor James W. Allen
Professor Lu Li
Associate Professor Kai Sun

Alexa Isabel Rakoski Mihaliov

ralexa@umich.edu

ORCID iD: 0000-0001-9654-2346

Dedication

For Vyetkov

Acknowledgements

First and foremost, I am indebted to my adviser, Professor Çağlıyan Kurdak. Most importantly, he taught me to think about physics intuitively and to study the topics I was most interested in. I have learned so much about critically analyzing data even while it was being collected, understanding transport, and communicating my findings clearly from him. Professor Kurdak always encouraged me in the many research and professional aspects of my work at Michigan, and I have greatly appreciated his guidance and support throughout the past five years.

I feel very fortunate to have studied SmB_6 at the University of Michigan. Professor James W. Allen, Professor Lu Li, and Professor Kai Sun are all experts on SmB_6 and on many of the experimental methods used to study it. I would especially like to thank Professor Lu Li for advising me during my Research Experience for Undergraduates (REU) at the University of Michigan in 2014, and for helping me become interested in studying SmB_6. Much of the theoretical work in this dissertation would not have been possible without enlightening discussions with Professor Kai Sun. It was also always interesting to learn about historical perspectives, mixed valence, and photoemission on SmB_6 from Professor James W. Allen. I would also like to thank Professor Allen for providing many thoughtful and insightful comments that helped improve my dissertation.

My research group members have been wonderful to collaborate with throughout my time at Michigan. Dr. Yun Suk Eo deserves special thanks, as much of the work in this dissertation would not have been possible without building on his previous studies. He also helped me learn experimental techniques in the clean room and about electrical transport when I first started working in the lab. I additionally enjoyed working with Juniar Lucien, Dmitri Mihaliov, Sandra Diez, and Shriya Sinha.

Outside of my research group, I would like to thank the many other people I interacted with at the University of Michigan. I especially learned a lot from Dr. Gang Li, Dr. Ziji Xiang, Dr. Colin Tinsman, and Dr. Benjamin Lawson. Professor Myron Campbell and Professor James Liu provided support during my REU in 2014. I enjoyed learning about gallium nitride from Professor Elaheh Ahmadi and working with Zumrad Kabilova on gallium oxide. Many of my classmates also supported me, especially Christopher Barnes, Riley Sechrist, and Ceren Dag. Carol Rabuck helped me learn about science communication and improve the clarity of my writing.

This work would not have been possible without collaborating with experts at many other institutions. I would like to thank Dr. Priscila Rosa for many valuable discussions and sharing her expertise on sample growth and strongly correlated materials, and Dr. Jonathan Denlinger for helpful discussions about modern photoemission measurements. It was also interesting to talk with Dr. Wesley Fuhrman about thermal transport and impurities in SmB_6. Most importantly, I was fortunate to study samples from a variety of sources. Dr. Priscila Rosa, Professor Zachary Fisk, Professor Beongki Cho, Dr. Boyoun Kang, and Myungsuk Song provided samples grown by the aluminum flux method, and floating zone grown samples were provided by Professor Geetha Balakrishnan, Dr. Monica Ciomaga Hatnean, Professor Tyrel McQueen, Dr. Seyed Koohpayeh, Dr. Wesley Fuhrman, Dr. W. Adam Phelan, and Juan Chamorro. I also learned interesting and detailed information about sample growth from many presenters and from practical activities at the University of Maryland's Fundamentals of Quantum Materials Winter School in 2018.

At the University of Notre Dame, I would like to thank my undergraduate physics professors for encouraging me to continue studying physics. I am especially grateful to Professor Mark Caprio for teaching me computational physics methods in Python and providing me with my first research opportunity.

At the Lurie Nanofabrication Facility, I would especially like to thank Dr. Vishva Ray for providing his expertise in e-beam lithography and processing small samples. Dr. Nadine Wang and Dr. Pilar Herrera-Fierro were also helpful in providing expertise on the tools and techniques available in the LNF. At the Michigan Center for Materials Characterization, I would like to thank Dr. Allen Hunter for training me in imaging and processing using the

scanning electron microscopes and focused ion beams, and for developing the technique that allowed us to create micro-sized samples.

My opportunities to study physics would not have been possible without the support of my family. I would especially like to thank my parents, Joseph and Sharon Rakoski, for their love, advice, and assistance. Special thanks go to my husband, Dmitri Mihaliov, who encouraged and supported me considerably during my final two years at Michigan. I am also grateful for support from my sister Rachel Rakoski, my brother Toby Nye, and for advice about graduate school from my uncle Dr. Richard Gorczynski and my cousins Dr. Michael Gorzynski and Dr. Jessica Gorczynski.

Funding for this work was provided by NSF grants #DMR-1441965 and #DMR-1643145 as well as funding from the NSF Graduate Research Fellowship Program, #DGE-1256260. The PPMS system, which was used for cryogenic measurements, was acquired through the NSF MRI Award No. 1428226. For SEM/FIB work done on the FEI Nova, I acknowledge the financial support of the University of Michigan College of Engineering and NSF grant #DMR-0320740, and technical support from the Michigan Center for Materials Characterization. For SEM/FIB work done on the FEI Helios, I acknowledge the University of Michigan College of Engineering for financial support and the Michigan Center for Materials Characterization for use of the instruments and staff assistance. I would also like to thank the Physics Department at the University of Michigan for providing financial support through fellowships and teaching opportunities.

Table of Contents

List of Figures

List of Tables

Abstract

Samarium hexaboride (SmB_6) is a correlated material in which strong f-d interactions lead to the opening of a small hybridization gap below 100 K at the Fermi energy. A long-standing mystery in SmB_6 was the plateau in resistivity below 4 K; this was recently determined to arise from a crossover from bulk to surface conduction due to possible topological effects. In this work, results concerning both bulk and surface conduction channels in SmB_6 are reported. First, SmB_6 is modeled as an intrinsic semiconductor with a layer of surface charge. Solving this model self-consistently yields band bending across the width of the bulk and reveals that a feature observed around 10-15 K observed in transport data can be explained by a crossover from bulk-dominated transport above this temperature to surface-dominated transport below. The temperature at which the feature occurs is expected to increase for thin samples and decrease for thick samples. This was tested and no difference between samples of different thicknesses was observed, but instead, questions about the role of sample growth technique arose. By comparing samples grown by two primary techniques, the aluminum flux method and floating zone method, using an inverted resistance geometry, a new bulk conduction channel at temperatures where surface conduction dominates is observed. This new channel is attributed to a combination of impurities and one-dimensional defects, or dislocations, and it is found to have a larger contribution in floating zone samples compared to Al flux grown samples. At higher temperatures, transport characteristics arise from the strong correlations, and no difference is found between samples grown by the two methods. Specifically, a well-known anomalous sign in the Hall coefficient is investigated in the context of skew scattering arising from the strong correlations. A model of skew scattering is presented, and the effect of skew scattering on calculating the Hall mobility is discussed. Finally, the characteristics of the surface conduction channel are investigated. One challenge

in surface studies of SmB_6 is precisely defining the transport geometry; conduction in sub-surface cracks and material defects always contribute. When conduction through cracks is accounted for, Hall bar geometry is demonstrated to be a powerful tool for accessing the lower mobility pocket on the SmB_6 surface. Further information is obtained by using ionic liquid gating in place of traditional metallic gating to tune the surface charge. This allows for more precise estimates of the carrier density and mobility of the lower mobility pocket. Overall, these results improve understanding of SmB_6, especially the roles of bulk effects and transport geometry. The new results also open further avenues for study, for example on the new bulk channel reported here and on the role of defects on the surface and bulk of SmB_6.

Chapter 1

Introduction

Samarium hexaboride (SmB_6) has long eluded classification due to its unique properties, beginning with its unusual spectroscopic characteristics and its temperature-resistivity curve.[1, 2, 3] Early research, beginning with X-ray spectroscopy, led to the classification of SmB_6 as one of the first rare-earth mixed valence compounds. [1, 4, 5] Later, a significant development identified SmB_6 as a Kondo insulator. [6] Kondo insulators are characterized by the opening of a small gap at the Fermi energy due to hybridization between f-electrons and conduction electrons. [7, 8]

Although the formation of the Kondo hybridization gap suggests that SmB_6 should be an insulator, transport results over 50 years have demonstrated that resistivity becomes temperature-independent in a conductive plateau below about 4 K. [3, 9, 10, 11] Initially this conduction was attributed to impurities, but a breakthrough came from the prediction that Kondo insulators can additionally be topological insulators. [12, 13, 14] Topological insulators undergo a crossover at low temperatures from a conventional state to a bulk insulating state with topologically protected metallic surface states. In SmB_6, evidence for such a protected surface state has been demonstrated by numerous experimental methods, especially transport [15, 16, 17, 18] and angle-resolved photoemission spectroscopy (ARPES). [19, 20, 21, 22, 23] However, recent work has challenged the identification of SmB_6 as a topological insulator and instead suggested that the observed physics comes from trivial surface states or exotic bulk states. [24, 25, 26, 27]

To frame current research, developments in understanding this unique material will be

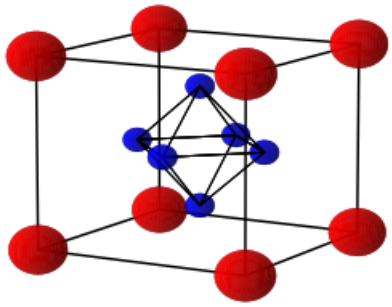

Figure 1.1: Sketch of cubic structure of SmB_6. Red spheres are Sm atoms and blue spheres are B atoms.

considered from a historical perspective. Emphasis will be given to discussing modern efforts to elucidate the properties of this fascinating and unique material, in some cases calling historical progress into question.

1.1 Early measurements

Metallic hexaborides, including SmB_6, crystallize in a simple cubic structure in the $Pm\bar{3}m$ point group. The B_6^{2-} octahedra are strongly bonded and form a cubic structure, [28] while the metallic ions form a second cubic structure with each ion at the body center of the structure formed by the boron octahedra. This structure is shown in Fig. 1.1. Most hexaborides can be classified as metals or insulators depending on the valence of the rare earth ion; divalent ions form insulating hexaborides while trivalent ions form metallic hexaborides. However, SmB_6 was found to behave differently. [2] It unexpectedly seemed to act like a metal near room temperature but demonstrate activated behavior characteristic of a semiconductor with a gap of about 3 meV below about 50 K. [9, 29] Below 4 K, a plateau was observed which was even more unexpected. [3, 9, 29] Early models interpreted this conduction as arising from impurity scattering as in conventional semiconductors, but these were insufficient to fully explain the conduction. [9] Hall effect measurements also showed a change from negative sign below 65 K to positive sign above 65 K, [9] which was not understood at the time.

Early magnetic measurements showed that SmB_6 is paramagnetic and follows Curie's law ($\chi(T) \sim 1/T$) for most of its temperature range, but it deviates at high and low temperatures. [30, 3, 31] At high temperatures, the deviation from Curie behavior is attributed to van Vleck susceptibility, which arises from the deformation or polarization of electron shells when magnetic fields are applied. This effect is quite common in $4f$ elements, and in SmB_6 the effect arises from the small splitting between the $J = 5/2$ and $J = 7/2$ sublevels. [3] Historical measurements also attributed low temperature features to van Vleck susceptibility, [3] but the modern understanding is that these are due to a superposition of Curie's law, the van Vleck deviation, and an Arrhenius behavior due to the formation of a spin gap. [32, 33]

The earliest spectroscopic measurements on SmB_6 were done by X-ray L-edge absorption and Mössbauer spectroscopy, which both provide information about the electron configurations and valence of a material. In SmB_6, the X-ray measurements showed that the L-edge had two overlapping peaks corresponding to 2+ and 3+ valence states in the Sm ions. This was initially interpreted as the presence of a mixture of Sm^{2+} and Sm^{3+} states in the lattice. [1, 4] However, this did not agree with magnetic susceptibility; magnetic ordering would have been observed if there were a significant number of Sm^{3+} ions. Later X-ray results also showed that all Sm sites were equivalent, countering the idea of a mixture of the two valence states. [34] Measurements of the Mössbauer isomer shift, which probes the average valence via local electron configurations near lattice sites, helped resolve this; data showed that the average Sm valence at each site was between 2+ and 3+. [5] These results led to the identification of SmB_6 as a homogeneous mixed valence material.

1.1.1 Mixed valence

Mixed valence (MV) materials are characterized by metallic ions with a non-integer valence. There are two types of MV: inhomogenous MV materials have a mixture of two valence states occuring in the lattice, whereas in homogeneous MV materials each atom fluctuates rapidly between the two valence states, creating a superposition of the two states. MV often occurs in compounds with an f band coexisting with an s, p, or d band at the Fermi energy. [35] Thus, many MV compounds contain rare-earth elements; SmB_6, pressurized samarium chalcogenides like SmS or SmTe, and TmSe, were some of the first MV compounds identified

and studied. [36, 37, 38, 35]

In the measurements discussed in the previous section, the X-ray result showed that transitions to both Sm^{2+} and Sm^{3+} states can occur, while the Mössbauer results showed evidence for the superposition of these two states at each lattice site. Later X-ray spectroscopy and magnetic susceptibility measurements verifed that SmB_6 is homogeneous mixed valence at all temperatures. [39] In other experiments, intentionally doped SmB_6 samples were used to shift the Sm valence towards 2+ or 3+. [40, 41, 42] Doping with a divalent ion like Sr^{2+}, or with an Sm vacancy, causes the overall Sm valence to shift towards 3+. Conversely, doping with trivalent ions like La^{3+} shifts the Sm valence towards 2+. [42]

In other MV systems like SmS, the valence could be tuned with the application of pressure. [37, 43] At atmospheric pressure, the Sm ion in SmS is divalent, but with application of pressure SmS enters a mixed valence state and eventually becomes trivalent. [44] However, in SmB_6, the Sm ion was found to remain mixed valence at all pressures studied. [43, 45, 39, 10, 46]

1.2 Hybridization and the Kondo effect

Besides valence, the electronic structure of SmB_6 was similarly initially not well-understood. Transport results showing metallic behavior at room temperature but activated behavior below about 60 K suggested a transition or crossover, but the mechanism was unknown. Two early theories were based on f-d hybridization in MV compounds [8] and Wigner crystallization. [47] Later work favored the hybridization model, and the description of the hybrid electronic structure was extended to the framework of the Kondo lattice model. [6] In the Kondo lattice model, each local moment (f electron) pairs with a conduction electron (d electrons in the case of SmB_6) to form a Kondo singlet. This pairing opens a small gap; in the case of SmB_6, the Fermi energy is in the hybridization gap, classifying it as a Kondo insulator. A schematic of the electronic structure before and after hybridization is shown in Fig. 1.2.

Experimentally, evidence for SmB_6 as a Kondo insulator was provided by spectroscopy, pressure, and magnetoresistance measurements. Photoemission results showed a shift in

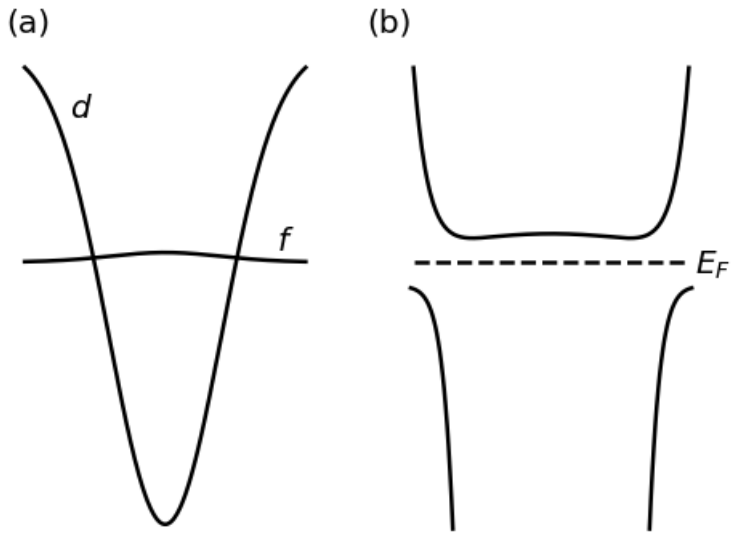

Figure 1.2: (a) Sketch of the unhybridized band structure of SmB_6. (b) Sketch of the hybridized band structure of SmB_6. Diagrams are not drawn to scale.

spectral weight with temperature, consistent with the formation of a gap. [4, 48, 49] Angle-resolved photoemission spectroscopy (ARPES) additionally showed that this gap formed around the X point. [50] In pressure measurements, a metal-insulator transition with a sample-dependent critical pressure around 40-80 kbar was observed. [45, 43, 10] This transition was linked to the closing of the gap under pressure, rather than to a structural or valence transition as in SmS. [45] Evidence showed that the gap does not close continuously with pressure in the 40-80 kbar range, which would be inconsistent with Kondo hybridization. However further work revealed the formation of magnetic order above the critical pressure with a clear ordered state forming above 100 kbar. [51] The clear ordered state was eventually identified with the RKKY interaction, suggesting that the Kondo effect was primarily responsible for the gap. [52]

Magnetoresistance measurements have also supported a gap at low temperatures. Measurements have consistently shown negative magnetoresistance, consistent with insulating behavior. [53, 54, 55, 56] Initially, this behavior suggested that SmB_6 is a Kondo insulator and verified the metal-insulator transition under pressure, [54, 57] but surprisingly, the mag-

netoresistance remains negative even when SmB_6 becomes conductive below about 4 K. Like in electrical transport, this behavior was initially attributed to impurities [54] or the formation of an electron-polaron complex. [58] The low-temperature magnetoresistance behavior is still an open question today, but the identification of Kondo insulators (or more generally, hybridized insulators) as possible topological insulators led to much greater understanding of the low-temperature behavior as a whole.

1.3 Topological Kondo insulators

From a geometrical perspective, topology is a way of classifying objects based on their shape. Essentially, if one object can be smoothly deformed into another object, the two objects are topologically equivalent. However, if the deformation is not smooth, for example, if a hole is created or closed up, the two objects are not topologically equivalent. A common illustration is that a doughnut and a coffee mug are topologically equivalent, but a sphere and a doughnut are not topologically equivalent. Mathematically, the topology of an object is represented by an integer. Two objects represented by the same integer are then topologically equivalent.

The idea of topology is not limited to geometrical objects; solids can also be classified by their topology via an integer or set of integers. The first use of topology in a solid system was the integer quantum Hall effect (IQHE), discovered in 1980 in a two-dimensional electron gas (2DEG). In the IQHE, the electrons undergo circular motion due to the application of a magnetic field. However, near the edges of the piece, the electrons cannot form full orbits, so instead they bounce along the edge in one direction. This phenomenon is known as a chiral edge state. Experimentally, the IQHE is observed as quantization of the Hall conductivity in integer multiples of e^2/h. [59] Subsequent work showed that the chiral edge state makes the IQHE topological; the integer classifying the topology also matches the integer multiple in the quantization of the Hall conductivity. [60]

An important aspect in the IQHE is the presence of time-reversal symmetry (TRS) breaking when the magnetic field is applied. However, it should be possible to also have a topological system that does not have external TRS breaking. One way of doing this is by combining two spin polarized integer quantum Hall systems. If the electrons in the two

systems have opposite spin polarization, the chiral edge states form a time-reversed pair, theoretically allowing a topological system to exist when magnetic field (TRS breaking) is not present. This system is known as the quantum spin Hall (QSH) insulator. The original example of such a system was in graphene with spin-orbit coupling, proposed by Kane and Mele. [61] Their model allowed spin polarization in the edge states via the spin-orbit coupling, a phenomenon known in modern studies of TIs as spin-momentum locking. Most importantly, the topological index that arises from this model is the Z_2 index. [62] It represents the number of times the chiral edge states cross the Fermi level, meaning that information about topology can be contained within the band structure of a material. While the QSH insulator was never observed in graphene, it was instead predicted to be present and subsequently verified experimentally in CdTe/HgTe/CdTe quantum wells. [63, 64]

The QSH insulator, like the IQHE, is still a two-dimensional system; soon after its theoretical development, similar ideas were extended to three-dimensional systems. [65, 66] Three-dimensional TIs have similar properties to the QSH insulator. First, the topology is still classified by the Z_2 index; this is related to the number of times a surface state crosses the Fermi energy for the 3D case. The crossings come about via inversion of the valence and conduction bands, which can only occur in materials with strong spin-orbit coupling. This band inversion forms a Dirac point. To be topologically non-trivial, the surface state must cross an odd number of times, or in other words, there must be an odd number of Dirac points in the gap. [67] From an experimental perspective, the presence of the Dirac points that span the gap mean that the topological surface state is conductive while the bulk of the material is insulating. The 3D TI must also have spin-momentum locking in its surface state, as seen previously in the QSH insulator. [67] The first experimentally identified TI was $Bi_{1-x}Sb_x$, [68] but likely the best known 3D TIs are Bi_2Se_3 and Bi_2Te_3. These were identified by using angle-resolved photoemission spectroscopy (ARPES) to directly map the band structure and reveal the Dirac cones. [69]

These first 3D TIs were all band insulators, but later work proposed that Kondo insulators could also have topologically protected states. [12, 13, 14] In the topological Kondo insulator, the valence and conduction bands form from hybridization between f electrons and conduction electrons, and this hybridization provides the necessary spin-orbit coupling

needed for a TI. The surface state would exist within the gap formed during Kondo hybridization. SmB_6 was specifically predicted to have one Dirac cone at the Γ point in the surface Brillouin zone, and two equivalent Dirac cones at the X points, which are relevant to the (001) crystal surface, and three equivalent Dirac points at the M points, relevant in the (111) crystal surface. [70]

To test whether SmB_6 is in fact a topological insulator, a number of different methods have been used. Initial results showed that it is indeed a surface conductor, but little consensus has been reached on the other crucial properties like the number of Dirac cones or the presence of spin-momentum locking. Initial results seemed to favor the TI prediction, but later results called this identification into question. Results on SmB_6 and the ongoing debate about the topological nature of SmB_6 will be discussed in the next section.

1.4 Is SmB_6 a topological insulator?

1.4.1 Spectroscopy

Angle-resolved photoemission spectroscopy (ARPES) has been a powerful tool for identifying predicted band TIs as it can directly map the Dirac cones. Most band TIs, like Bi_2Se_3, have gaps on the order of a few eV, but the gap in SmB_6 is two orders of magnitude smaller. This makes it challenging to perform ARPES measurements on SmB_6. ARPES experiments in SmB_6 have primarily looked for the predicted topologically protected surface states near the Γ and X pockets on the (001) surface in the 2D Brillouin zone, [70] rather than the M points on the (111) surface. Experimental data on the (001) surface indicates features not arising from the bulk band structure at the Γ and X pockets, but wide disagreement still remains on the topological nature of these states.

Initial reports showed that there was a Dirac point at Γ and one at each of the two equivalent X points, making three pockets and suggesting confirmation that SmB_6 hosts topological surface states. [19] Further investigation of circular dichroism (differences in ARPES spectra between right and left circularly polarized light) indicated a spin texture as would be expected for topological surface states. [21, 20] Other studies have called into

question the initial confirmation that SmB_6 hosts an odd number of Dirac cones. One observes three metallic states but finds their origin to be trivial, [23] and many reports only observe pockets at the X points. [71, 22, 72] Some researchers have even argued for a purely trivial origin for the observed metallic states. Possible trivial sources include dangling B bonds introduced during cleaving [73], Rashba splitting, [24], or many-body resonances in the 4f band. [24, 25] One possibility for reconciling these disagreements is connected to STM and STS measurements.

Like ARPES, STM and STS are performed on samples cleaved *in situ*, and the cleaved surfaces host a variety of topographies. The most common are polar unreconstructed surfaces terminated by only B atoms or only Sm atoms, as well as a (2x1) nonpolar reconstructed surface, which appears as stripes of B and Sm atoms. [74, 75, 76] The polar surfaces, which have extra charge on them, can affect the band structure near the surface via band bending, and in fact STS measurements show that the features are shifted among the Sm polar, B polar, and nonpolar surfaces. In addition, the different types of topographies extend over distances of order 10 nm, but methods like ARPES are performed over areas of order 10 μm. This means that ARPES measurements could be averaging over the band structures of the different surface topographies, unintentionally smearing the band structures they observe. Averaging over different polarities combined with the difficulties in resolution in such a small gap in SmB_6 might prevent ARPES from obtaining clear features. [25, 77] In fact, one way to circumvent polarity issues is to cleave SmB_6 on the (111) surface. An ARPES study performed on a cleaved (111) surface found three equivalent M pockets with a spin texture consistent with a topological origin on the (111) surface. [78] This result has been overlooked as much of the debate about the topological nature of SmB_6 has focused on the characteristics of the Γ and X pockets. However, this result may indicate a turning point in TI studies of SmB_6 due to the relative ease of measuring and interpreting the (111) surface in comparison to the (001) surface.

Scanning tunneling microscopy (STM) and spectroscopy (STS) have also been used to probe for topological surface states using quasiparticle interference. Only one report so far has demonstrated that the observed in-gap states are topological. [79] This report reveals three Dirac cones at the Γ and 2X points, although the parameters of the states do not

match those given by ARPES.

1.4.2 Electrical transport

The prediction that SmB_6 could host topologically protected surface states was first tested on SmB_6 via transport. [15, 16, 18] Since topological insulators have an insulating bulk and a conductive surface, researchers could test whether the conduction below 4 K was coming from the bulk or the surface. One way to do this is to place contacts on the top and bottom surfaces of the sample and performing the measurements with different configurations for the current and voltage leads. Different results are expected for current that can travel through the bulk of the sample compared to current that must flow around the surface, and using this method, surface conduction was verified. [15]

An independent method of performing the same test is by varying the sample thickness. Since the Hall coefficient depends on thickness in three-dimensional systems but is independent of thickness in two-dimensional systems, Hall measurements at different locations on a wedge-shaped sample were performed. The Hall measurements collapsed to a single curve below 4 K, demonstrating that the conduction is on the surface. [16] In a related study, researchers found that the temperature at which the resistance plateau appears increases as the sample thickness decreases (or as the ratio of bulk to surface decreases). [18]

Although electrical transport showed that the low-temperature conduction was a surface effect, topological protection is still in question. One study has demonstrated signatures of spin-momentum locking in SmB_6, [80] but the results have not been reproduced. Instead, other experimental methods have been used to answer this question.

1.4.3 Magnetotransport

Another way to detect a topologically protected surface is by searching for features of weak anti-localization (WAL). A related effect, weak localization, occurs when there is constructive interference between electron paths and their time-reversed counterparts; WAL occurs when the interference is instead destructive. However, in materials where TRS is preserved, this interference can no longer occur. To probe whether WAL is present, a magnetic field can be

applied to break TRS. Then, an increase in resistance due to WAL would be observed as a peak near zero magnetic field. WAL is characterized by a dephasing length and a prefactor α. Each topological conduction channel is expected to contribute 1/2 to the prefactor, so with two spin states and three proposed pockets, SmB_6 would be expected to have $\alpha = 3$.

Experimental searches for WAL have had mixed results. [56, 81, 82, 55] Three claim to have observed WAL using Hall bar geometry, but in all three studies, the results for α are highly variable and not in agreement with the expected value of 3. [81, 82, 55] Other discrepancies are also present, for instance the observation of WAL-like features with in-plane magnetic field. [55] One possible source of the discrepancies, however, is the use of Hall bar geometry, since current can flow on all the surfaces. Thus, when magnetic field is in-plane to two surfaces of the Hall bar, it will be normal to two other surfaces, so if WAL is present, features would still be observed. A fourth study performed magnetoresistance measurements on Corbino geometry both to confine current to a single crystal surface and because it is not sensitive to the sign of the carriers. In this study, features were observed near zero magnetic field, but these features were found to be dependent on the sweep rate of the magnetic field. Since WAL should be intrinsic to the sample, the authors concluded that no WAL was observed. [56] In these studies, the authors have mainly attributed the lack of WAL or the discrepancies in the values of α to impurity scattering. For example, the presence of magnetic impurities, including Sm^{3+} ions in a surface oxide, might provide scattering centers that overwhelm WAL. [56, 55]

Besides WAL, magnetoresistance has been used to study the idea of a TI in SmB_6. Recalling that the magnetoresistance in SmB_6 is negative, new data revealed that the maximum negative magnetoresistance occurs at about 5 K. [58, 83, 84] This has been used to support the idea of a transition to topological surface conduction below about 5 K. In a topological insulator, while metallic surface states might be expected to induce positive magnetoresistance, magnetic field breaks the time reversal symmetry of these states. Thus, negative magnetoresistance observed over a large range of magnetic field in SmB_6 is not unreasonable within a TI framework. In addition, one study performed angle-dependent magnetoresistance and observed a symmetry change near 5 K. [83] Above 5 K, their data showed fourfold symmetry, which is the expectation for a cubic bulk material. Below 5 K, however, they

observed a change to twofold symmetry, and the formation of a surface state is one possible origin for this symmetry change.

1.4.4 Quantum oscillations

De Haas-van Alphen (dHvA) oscillations, or quantum oscillations in magnetization, have been used to test the low-temperature conduction for possible topological origin. The angle dependence of dHvA oscillations allows the shape and dimensionality (2D or 3D) of the Fermi surface of a material to be mapped. In SmB_6, one study found that the Fermi surface giving rise to dHvA oscillations was two-dimensional, consistent with the TI picture of SmB_6, [85] while another found evidence of a 3D Fermi surface. [26] In the first of these studies, three main oscillation frequencies were observed in a flux-grown sample. Two of these were identified with the X pockets projected on different crystal surfaces, while one was attributed to the Γ pocket. However, the effective masses obtained for these pockets were much lower than what was observed in ARPES. [85] In the second study, oscillations were observed at much higher frequencies on floating zone samples, and the angular dependence was attributed to a 3D effect, due to its similarity to trivial hexaborides. The authors proposed that a Fermi surface of neutral quasiparticles was responsible for these results. [26] Later studies from both collaborations provided further evidence for each side of the debate. [86, 27]

Many researchers have attempted to explain these conflicting results. First, thermal transport has been used to search for neutral quasiparticles, which would be manifested as a nonzero thermal conductivity as temperature approaches zero. SmB_6 also has an unexplained excess in specific heat below 4 K, [87] which could be due to neutral quasiparticles. One study found evidence for charge-neutral quasiparticles in floating zone samples [27] while another finds no evidence for them in flux grown samples. [88] A further study comparing flux and floating zone grown samples found no evidence for charge-neutral quasiparticles in either type. [89] Besides charge-neutral quasiparticles, one possibility is that flux grown samples have non-percolating domains to which dHvA is sensitive but thermal transport is not. [88] Alternatively, results at zero and non-zero magnetic fields could be explained by two scattering channels, one magnetic and one non-magnetic, that might affect dHvA results. [89]

Besides thermal considerations, ARPES data showed a 2D Fermi surface which corresponded to frequencies seen by Tan, et al., [72] suggesting that the 3D interpretation was incorrect. Another experimental study found that aluminum inclusions in flux-grown samples could play a role. When the aluminum was removed, the oscillations disappeared, suggesting that inclusions were the source of the 2D dHvA data and that SmB_6 does not give rise to intrinsic quantum oscillations. [90] Oscillations arising from rare-earth impurities (rare-earth elements are notoriously difficult to purify when preparing them for crystal growth) have also been recently ruled out. [91]

To explain these conflicting results, theoretical proposals have considered both an intrinsic origin, for example charge-neutral quasiparticles, and an extrinsic origin, like pockets of an unknown metallic phase. Some of the intrinsic-origin scenarios have included oscillations by excitonic states [92, 93] or a Majorana fermion band that breaks gauge symmetry. [94, 95] Others have proposed breakdown of the gap under magnetic field, [96, 97] or ways for oscillations to occur in gapped systems based on the unhybridized band structure or as an effect of the band edges. [98, 99] The other possibility is that the quantum oscillations have an extrinsic origin from disorder or impurities. One interesting proposal was that of a nodal semimetal, in which states from the conduction and valence band could spill into the gap in the presence of generic short-range disorder. [100, 101] Alternatively, magnetic impurities could be responsible for the excess heat capacity at low temperatures. [102] These local moments in the lattice would be screened, and the amount of screening, and thus the magnetization, would oscillate in magnetic field. [103] Still another report focused on nonmagnetic impurities, which were found to form a deep impurity band as in a metal as well as an in-gap band, [104] and another proposal revisited the idea of in-gap impurity states specific to the type of band structure in Kondo insulators. [105] No consensus has yet been reached on a full theoretical description of dHvA oscillations in SmB_6.

As a final note on quantum oscillations, these studies have all focused on dHvA oscillations, but in most materials, Shubnikov-de Haas (SdH) oscillations in resistivity are much easier to observe and should appear near the same magnetic field as dHvA oscillations. In SmB_6, no SdH oscillations have been observed up to 80 T. [106] This is another open question in SmB_6 quantum oscillations, as both effects are expected to appear at similar magnetic

fields.

1.5 Open questions in SmB_6

1.5.1 Dependence of results on sample growth method

Many of the results in the above sections can be divided along the lines of sample growth method. In SmB_6, two primary techniques for sample growth are used: aluminum flux growth and optical floating zone growth. These techniques will be discussed in more detail in Chapter 2. In general, samples can be grown below the melting point by the Al flux method, which may enhance the stoichiometry of the target sample by preventing vaporization of Sm at high temperatures. [107] Flux grown samples are small (a few mm in each direction) and can contain inclusions of the flux. [108] In contrast, floating zone samples are grown at or above the melting point, and the high temperatures used can introduce defects due to thermal stresses [109] or through vaporization of Sm. Floating zone samples are quite large (a few cm long) and are uncontaminated by flux.

In general, characterization methods like powder X-ray diffraction show no obvious difference between samples grown by the two methods. [11, 107] However, many of the experimental results that disagree as to the origin (topological or trivial) of the low-temperature physics in SmB_6 can be also separated by sample growth technique. ARPES results that find evidence for a trivial surface in SmB_6 are done on floating zone samples, [24] although some results on floating zone samples do provide evidence for a topological surface. [78]. However, the majority of the compelling photoemission evidence for a topological surface comes from flux grown samples. [21, 20] Similarly, dHvA results indicating a 2D Fermi surface were performed on Al flux grown samples, while the 3D Fermi surface results were performed on floating zone samples. [85, 26] Related to this, thermal transport results are fairly consistent among Al flux grown samples but vary widely on floating zone samples. [27, 88, 89] Transport results on both flux and floating zone samples show differences as well, but a detailed discussion will be reserved for Chapters 4 and 5.

1.5.2 Characteristics of the energy gap

Besides the question of whether SmB_6 is indeed a topological insulator, inconsistencies also remain in understanding the hybridization gap. Transport measurements have consistently found activated behavior with an activated energy of 3-5 meV, [3, 9, 15, 110] while spectroscopic measurements have shown a larger gap of about 20 meV. [111, 22, 112] Detailed transport studies of the activated behavior subsequently identified two activated regions separated by a feature near 10-15 K. From about 4-10 K, the extracted activation energy is 3-5 meV, but from 15-50 K (where the gap starts to close) the extracted activation energy is 5-10 meV. [113] A picture of a 20 meV total gap with an impurity level about 3 meV below the conduction band emerged to connect all these results [111, 114, 115] In this model, the total gap size of 20 meV corresponds with the spectroscopic results and is twice the activation energy measured from 15-50 K in transport, while the 3 meV difference between the impurity and conduction bands would correspond with the activation energy measured from 4-10 K.

However, other evidence indicates that the two gaps behave differently under magnetic field and that the small gap of 3-5 meV actually corresponds with Kondo hybridization rather than an impurity level. [84, 83] One point-contact spectroscopy measurement found a total gap of 7 meV, and both the temperature dependence of the gap and the nonzero spectral weight seen inside the gap suggested that this was a clean gap arising from Kondo hybridization. [116]. Pressure measurements also reveal a metal-insulator transition as the 3-5 meV gap closes with pressure at around 60 kbar, consistent with what should be seen for a Kondo insulator. [117, 46] Other pressure measurements show that the 20 meV gap closes at about 100 kbar, but the origins of this mechanism are not well-understood. [46] One hypothesis is that a magnetic state that forms near the same pressure causes bulk metallization, [118], although studies of magnetic order in SmB_6 at high pressures are still ongoing.

Other than the model of an impurity band in the gap, other scenarios like an indirect gap have been proposed. [119] In this case, the indirect gap would be associated with the 3-5 meV activation energy, while the direct gap would be associated with the 20 meV gap seen in spectroscopy. In Chapter 3, the possibility of a clean, direct gap with band bending

of the bulk band structure near the metallic surface will be discussed. Since that work was completed, another model of in-gap impurity states that undergo activated hopping conduction has been proposed. [105] This model and its relevance to our bulk conduction studies will also be discussed.

1.5.3 Role of impurities

The role of impurities in SmB_6 has long been puzzling. Early studies attributed the plateau below 4 K to impurity conduction, but this was found to be untenable. [9] Recently, however, the role of impurities has come to the forefront once again. Our recent measurements on samples with Sm vacancies suggested that the gap in SmB_6 is protected against disorder. [110] Other results, however, suggest that both magnetic and nonmagnetic impurities could be responsible for the dHvA oscillation results as well as some of the unusual thermal behavior of SmB_6. [120, 104]

The most common source of impurities in SmB_6 is other rare-earth elements, as they are very difficult to purify out of Sm. During growth, vacancies, higher-dimensional defects, or other phases could also be introduced due to stresses (thermal, vibrational, chemical) in the environment. One approach to improve sample purity is to isotopically purify the Sm, keeping only Sm-154; then the only remaining impurity would be Gd-154. [102]

Magnetic impurities, like Gd remaining even after purification, are an important consideration. First, if SmB_6 is a topological insulator, magnetic impurities naturally present in samples could destroy time reversal symmetry, meaning that the observed surface conduction is trivial. If SmB_6 is not topological, magnetic impurities could provide a source of disruption to the Kondo effect. These magnetic ions could act as local magnetic moments and would be screened by the surrounding conduction electrons. One report has suggested that the amount of screening could oscillate in magnetic field, leading to observation of bulk oscillations in magnetization. [103] Another recent work finds that Gd impurities at very low concentrations create enough screening to destroy the Kondo effect locally. These metallic ions can then percolate, which would explain why dHvA oscillations are seen but SdH are not. [121]

Nonmagnetic impurities, including rare-earth elements and Sm vacancies, also play a

major role. Systematic transport studies of Sm doped with nonmagnetic rare earth elements has shown that the Kondo effect and the surface conduction are interrupted even with less than 0.5% doping. [122] One study of SmB_6 with Sm vacancies found that the vacancies provided scattering centers that increased the resistivity by about an order of magnitude compared to a pure sample. [123] In Chapter 5, results suggesting that Sm vacancies play a role in bulk conduction at temperatures below 2 K will be presented, [110] and the role of Sm vacancies and other defects will be considered in more detail.

Chapter 2

Methods and Techniques

2.1 Introduction

The primary method used to probe Sm_6 in this work is electrical transport in the dc limit, close to zero frequency. Transport measurements are performed in the linear response regime, where an electric field $\mathbf{E}$ applied to the sample yields a proportional response in the current density, $\mathbf{j}$. In the linear regime, these are related by the conductivity matrix, σ, via Ohm's law:

$$\mathbf{j} = \sigma \mathbf{E}. \tag{2.1}$$

In the next sections, Ohm's law will be discussed using classical transport theory, and the conductivity matrix will be connected to parameters measured in experiment. An important consideration in relating theory to experiment is the transport geometry, or location of contacts used to apply the electric field and measure the response. Various transport geometries will be introduced, and the measured quantities will be presented.

In the following sections, practical considerations for preparing samples for transport measurements will be discussed. These include techniques for growing SmB_6 samples, preparation of crystal surfaces before measurement, and defining the transport geometry. Finally, a technique for preparing micro-sized pieces using a focused ion beam will briefly be described.

2.2 Classical transport

In this work, we primarily use the Drude model to analyze transport parameters. The conductivity tensor for particles with charge e can be derived from Newton's equations:

$$\frac{d\mathbf{p}}{dt} = e(\mathbf{E} + \mathbf{v} \times \mathbf{B}). \tag{2.2}$$

For particles with effective mass m^* and scattering time τ, this becomes

$$m^*(\frac{d}{dt} + \frac{1}{\tau})\mathbf{v} = e(\mathbf{E} + \mathbf{v} \times \mathbf{B}). \tag{2.3}$$

Transport occurs at steady state, and if we assume that the magnetic field is $\mathbf{B} = B\hat{z}$, Eq. 2.3 can be decomposed in the three dimensions as:

$$\begin{aligned} \frac{m^* v_x}{\tau} &= e(E_x + v_y B) \\ \frac{m^* v_y}{\tau} &= e(E_y - v_x B) \\ \frac{m^* v_z}{\tau} &= e(E_z). \end{aligned} \tag{2.4}$$

The velocity components can be related to the current density in Ohm's law (Eq. 2.1) by $\mathbf{j} = -ne\mathbf{v}$, where n is the electron (carrier) density, so that the conductivity matrix in Eq. 2.1 can be obtained for a general case. This is

$$\sigma = \begin{pmatrix} \frac{ne\mu}{1+\mu^2B^2} & \frac{ne\mu^2B}{1+\mu^2B^2} & 0 \\ -\frac{ne\mu^2B}{1+\mu^2B^2} & \frac{ne\mu}{1+\mu^2B^2} & 0 \\ 0 & 0 & ne\mu \end{pmatrix}, \tag{2.5}$$

where $\mu = e\tau/m^*$ is the mobility. Usually, the quantity μ^2B^2 is very small, and it can be neglected. Also, when magnetic field is applied in the z-direction, measurements are performed only in the $x - y$ plane. With these considerations, the conductivity matrix can

be simplified as

$$\sigma = \begin{pmatrix} ne\mu & ne\mu^2 B \\ -ne\mu^2 B & ne\mu \end{pmatrix}. \tag{2.6}$$

The resistivity can be obtained by inverting this matrix,

$$\rho = \frac{1}{1+\mu^2 B^2} \begin{pmatrix} \frac{1}{ne\mu} & -\frac{B}{ne} \\ \frac{B}{ne} & \frac{1}{ne\mu} \end{pmatrix}. \tag{2.7}$$

Again, the prefactor is usually small and can be neglected. Thus, the basic Drude transport equations are

$$\begin{aligned} \rho_{xx} &= \frac{1}{ne\mu} \\ \rho_{xy} &= -\frac{B}{ne} \end{aligned} \tag{2.8}$$

Depending on the transport geometry used, ρ_{xx} and ρ_{xy} can be calculated from the data and used to find the carrier density n and mobility μ. Often, the Hall coefficient $R_H = -1/(ne)$ is used in place of ρ_{xy}, and the sign of the Hall coefficient gives the sign of the charge carriers. In this derivation, negative Hall coefficient corresponds to negative charge carriers, but in practice, the setup of the measurement must be considered to determine whether this convention applies.

2.2.1 Two-channel conductivity

One important example where Eq. 2.8 cannot be used is when a material has both positive and negative charge carriers. The signs of the carriers cancel each other out in ρ_{xy}, meaning that the magnitude of the carrier density will be wrong and the sign will only indicate the dominant carrier. Instead, Eq. 2.8 can be modified starting from Eq. 2.6. The diagonal terms are additive, but the off-diagonal terms depend on the signs of the carriers. The new matrix becomes

$$\sigma_{n,p} = \begin{pmatrix} ne\mu_n + pe\mu_p & ne\mu_n^2 B - pe\mu_p^2 B \\ -ne\mu_n^2 B + pe\mu_p^2 B & ne\mu_n + pe\mu_p \end{pmatrix}, \tag{2.9}$$

where n denotes electrons and p denotes holes. When this matrix is inverted, we obtain:

$$\begin{aligned} \rho_{xx} &= \frac{1}{ne\mu_n + pe\mu_p} \\ \rho_{xy} &= \frac{B}{e}\frac{p\mu_p^2 - n\mu_n^2}{(p\mu_p + n\mu_n)^2}. \end{aligned} \tag{2.10}$$

This process can be carried out for any number of channels of both signs of carrier. For exotic materials like SmB_6, more nuanced analysis of the data will be necessary, and the corresponding modifications to the above models will be discussed in depth in later chapters.

2.2.2 Connection to measurement

Transport measurements are usually performed by exciting the sample with a current, I, and measuring the resultant voltage, V. The ratio of these two quantities gives the resistance, $R = V/I$. Resistance is the primary parameter that is obtained from a transport measurement, and it can be measured under different conditions. For example, resistance is often measured as a function of temperature, magnetic field, or pressure; in this work we mainly consider temperature and magnetic field. Resistance is also closely related to the resistivity ρ obtained from classical transport theory. To relate ρ and R, it is necessary to use a well-defined transport geometry, which will be discussed in the following section.

2.3 Transport geometry

In general, ρ_{xx} and ρ_{xy} can be obtained from a measurement as long as the geometry of the sample and measurement is known. Three types of well-defined transport geometries will be considered here: Hall bar, van der Pauw, and Corbino disk. Hall bar geometry is used for needle-like samples and employs measurements of both transverse and longitudinal resistance, which are then used to obtain carrier density and mobility. Van der Pauw geometry is closely related, also making use of both transverse and longitudinal resistance, but it is optimal for plate-like or oddly-shaped samples. Corbino disk geometry is comprised of concentric circular contact pads deposited on the sample. It can be used on any flat surface of a sample to find ρ_{xx}, and it can be used to characterize single crystal surfaces of samples

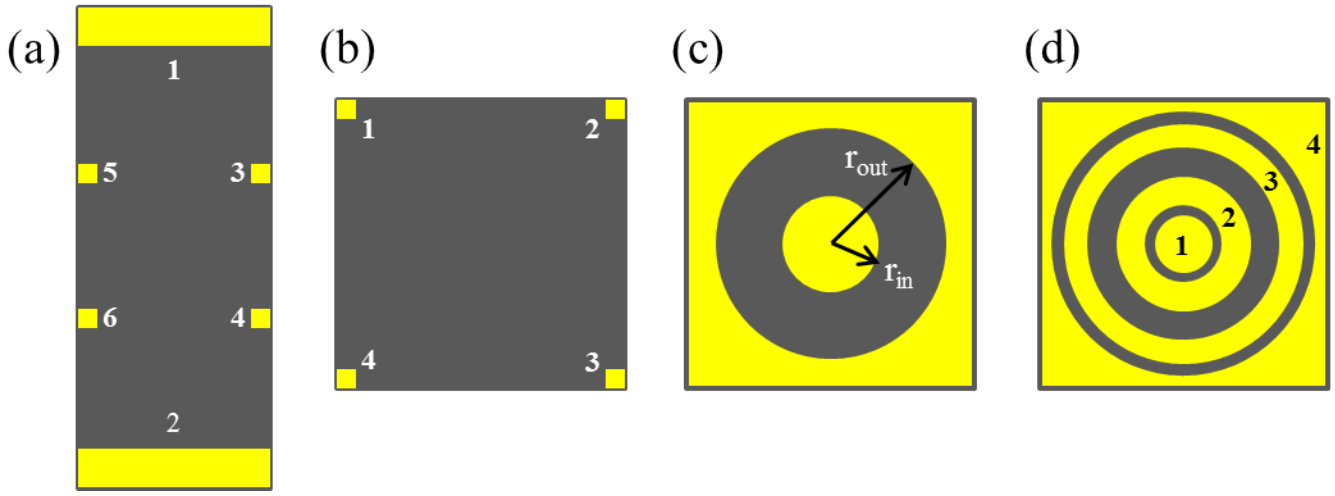

Figure 2.1: Top views of (a) Hall bar geometry, (b) van der Pauw geometry, and (c) two-terminal and (d) four-terminal Corbino disk geometry. The samples are shown in gray and the contacts are shown in yellow.

or to separate contributions from bulk and surface channels.

2.3.1 Hall bar geometry

The layout of Hall bar geometry is shown in Fig. 2.1(a). R_{xx} is measured by $R_{1,4;2,3}$ (with numbers in reference to the figure), meaning that current is passed from 1 to 4 while voltage is measured between 2 and 3, or by $R_{1,4;6,5}$. R_{xy} is measured by $R_{1,4;2,6}$ or $R_{1,4;3,5}$.These are converted to ρ_{xx} and ρ_{xy} by

$$\begin{aligned} \rho_{xx} &= \frac{wt}{\ell} R_{xx} \\ \rho_{xy} &= tR_{xy} \end{aligned} \tag{2.11}$$

where w, t, and ℓ are the width, thickness, and length of the sample. The prefactor of ρ_{xx}, in this case wt/ℓ, is called the "geometric factor" of the transport geometry. Often, the quantity of interest is the Hall coefficient, R_H, rather than the transverse resistance, R_{xy}. The Hall coefficient is related to the above parameters by

$$R_H = \frac{\rho_{xy}}{B} = \frac{t}{B} R_{xy}. \tag{2.12}$$

2.3.2 Van der Pauw geometry

Van der Pauw geometry [124] can be used for any sample shape, but in this work it is used for square samples, as shown in Fig. 2.1(b). R_{xx} is obtained by an average of $R_{1,2;4,3} = R_{xx,1}$ and $R_{1,4;2,3} = R_{xx,2}$, while R_{xy} requires either $R_{1,3;2,4}$ or $R_{2,4;1,3}$. In this notation, ρ_{xx} and ρ_{xy} are obtained by

$$\begin{aligned} \rho_{xx} &= f\frac{\pi t}{\ln 2}\frac{R_{xx,1}+R_{xx,2}}{2} \\ \rho_{xy} &= tR_{xy} \end{aligned} \tag{2.13}$$

where f satisfies the transcendental equation

$$\frac{R_{xx,1}-R_{xx,2}}{R_{xx,1}+R_{xx,2}} = f\cosh^{-1}(\frac{\exp \ln 2/f}{2}). \tag{2.14}$$

If the measurements of $R_{xx,1}$ and $R_{xx,2}$ are identical, $f = 1$. In square samples, f is usually approximated as 1, although a few percent correction can be made by including this factor.

2.3.3 Corbino geometry

The simplest version of Corbino geometry is made up of two concentric circular contact pads, as shown in Fig. 2.1(c). Current flows from the inner ring (1) to the outer ring (2), confining the current to the annular region between the currents. [125] To find resistance, voltage is measured in the region between the two disks. The measured R_{xx} is related to transport parameters by

$$R_{\text{Corbino}} = \frac{\ln(r_{out}/r_{in})}{2\pi}\frac{1+\mu^2B^2}{ne\mu} = C\rho_{xx}, \tag{2.15}$$

where the inner (r_{in}) and outer (r_{out}) radii are the radii of the two current contacts, as shown in Fig. 2.1(c). One way of performing this measurement is to add more rings, for example making a four-terminal Corbino disk as shown in Fig. 2.1(d). In this configuration, the resistance $R_{1,4;2,3}$ gives R_{xx}.

Unlike Hall or van der Pauw geometry, Corbino geometry cannot be used to measure R_{xy}, and Eq. 2.15 depends on the magnetic field. This means that the magnetoresistance is

expected to be quadratic for a Corbino disk. Angle-dependent magnetoresistance measurements, where B is replaced by $B\cos\theta$, can also be used to extract the mobility and then the carrier density.

2.3.4 Inverted resistance measurements

The property of confining current to an annular region allows Corbino disks to be used in a number of ways. For example, in a material with different transport characteristics on different crystal planes, Corbino disks can be used to study each plane individually. In materials with conductive surface states, like SmB_6, Corbino disks can be used to study the properties of a single surface. This also eliminates uncertainty in the geometry in a topological material due to corners and edges.

In addition, Corbino disks can be used in materials with both surface and bulk conduction to study bulk physics at temperatures where surface conduction is dominant. It can also identify whether conduction is coming from the bulk or the surface of a sample. This technique is known as inverted resistance. [126, 127] To perform an inverted measurement, the voltage is measured *outside* of the annular region where current is flowing.

To understand how the inverted resistance method works, first consider the geometry of Fig. 2.1(d) on a two-dimensional material. A standard measurement would be made by passing current between 1 and 4 while measuring voltage between 2 and 3 ($R_{1,4;2,3}$). For the inverted measurement, current is instead confined between 1 and 2. If the material is two-dimensional, no voltage will be measured between 3 and 4; that is, $R_{1,2;3,4} = 0$. In this case, contact 2 behaves like a Faraday cage, so no current can flow outside of it.

However, if the same measurement is done on a three-dimensional material, some current could flow outside of contact 2 through the bulk. In a material with both bulk and surface conduction, all the surface current is confined between contacts 1 and 2. Thus, the measured voltage is a purely bulk signal. This signal will be quite small, especially in regimes where the surface conduction dominates.

To improve the signal, different types of Corbino geometry can be used. [127] The optimal configuration is two-sided, with a four-terminal Corbino disk on one side and a two-terminal Corbino disk on the other, as shown in Fig. 2.2. The standard measurement can be made

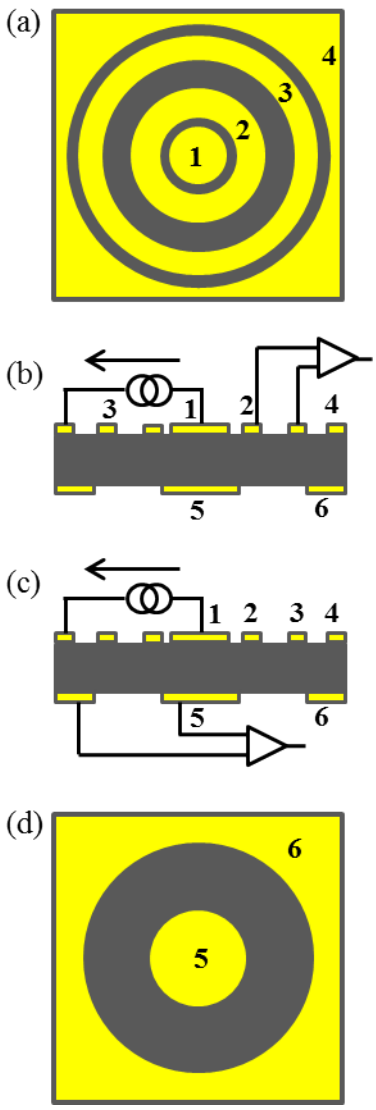

Figure 2.2: (a) Four-terminal Corbino on top surface of sample. (b) Side view of the sample showing a standard measurement, $R_{1,4;2,3}$. (c) Side view of the sample showing an inverted measurement, $R_{1,4;5,6}$ (d) Two-terminal Corbino on bottom surface of sample.

as before ($R_{1,4;2,3}$) using only the four-terminal side, as shown in Fig. 2.2(b). The inverted measurement is made by passing current on one side fo the sample and measuring voltage on the opposite side ($R_{1,4;5,6}$), as shown in Fig. 2.2(c).

To understand how resistance and resistivity are related in Corbino measurements, we consider three cases. First, if the material is a purely bulk conductor, the resistance is proportional to the bulk resistivity as in Eq. 2.15:

$$R = C_b \rho_{xx}, \tag{2.16}$$

where C_b is a geometric factor (as in Eq. 2.15). In this case, standard and inverted measurements differ only by the choice of electrode, so only the prefactor differs between the two measurements. Thus, in data, the standard and inverted resistance-temperature curves have the same shape and are parallel to each other.

However, if surface conduction is dominant, the standard measurement will be proportional to the surface resistivity (also known as sheet resistance), R_{sq}:

$$R = C_s R_{\mathrm{sq}}, \tag{2.17}$$

where C_s is also a geometric factor but with different form than C_b due to the reduced dimensionality. As discussed previously, in the presence of surface conduction, inverted resistance will only pick up signal coming from the bulk. This signal depends on both the bulk and surface resistivities:

$$R_{\mathrm{Inv}} = C_{\mathrm{Inv}} \frac{R_{\mathrm{sq}}^2}{\rho_{xx}}, \tag{2.18}$$

where C_{Inv} is yet another geometric factor. Because Eq. 2.18 is inversely proportional to bulk resistivity, the temperature dependence of the inverted measurement will be inverse to the temperature dependence of the bulk measurement in regions where bulk conduction dominates. For example if the bulk exhibits activated behavior, $\rho(T) \propto exp(E_a/T)$, the inverted measurement will exhibit the opposite, $\propto exp(-E_a/T)$). However, the presence of a third conduction channel in the bulk can change this expected temperature dependence of the inverted resistance. This will be revisited in Chapter 5.

2.4 Growth methods

Modern SmB_6 samples are typically grown either by the aluminum flux method or the optical floating zone method. Aluminum flux growth allows SmB_6 to crystallize at equilibrium in a solution of molten aluminum and produces millimeter-sized crystals. On the other hand, growth in the floating zone method occurs when Sm and B are directly melted together and cooled, and it produces crystals up to 10 cm long. Both techniques make use of the samarium-boron phase diagram. [128]

2.4.1 Flux growth

Flux growth employs a stoichiometric mixture of the target crystal dissolved into molten metal (the flux). The material chosen as flux depends on the target crystal; for SmB_6, aluminum is almost always used. In many flux growths, the components are sealed into a quartz ampoule to prevent contaminants from the environment from being incorporated into the crystal. However, aluminum flux cannot be used in quartz, and SmB_6 requires a higher temperature than can be used for sealed quartz. [108] Instead, a tantalum or alumina crucible is typically used, and these crucibles are chosen to minimize their effect on the crystals. Since the crucibles are not sealed, growth is performed under an inert gas, often argon. [129]

For SmB_6, powders of boron and samarium are placed into the crucible along with aluminum pellets. The components are heated and stirred thoroughly to ensure that the Sm and B powders are dissolved in the flux. The mixture is held at about 1600°C before being cooled slowly back to room temperature. The most important factor affecting the quality of Al-flux grown SmB_6 is the cooling rate. Fast cooling rates can lead to low-quality crystals; cooling rates reported in the literature vary from a few hours to two weeks. [130, 131] After the mixture reaches room temperature, the remaining Al is removed with a strong acid or base, usually sodium hydroxide (NaOH). [108]

Crystals of SmB_6 prepared by the Al-flux method are typically a few millimeters in each dimension, and they can have a needle- or plate-like shape. [132] Examples can be seen in

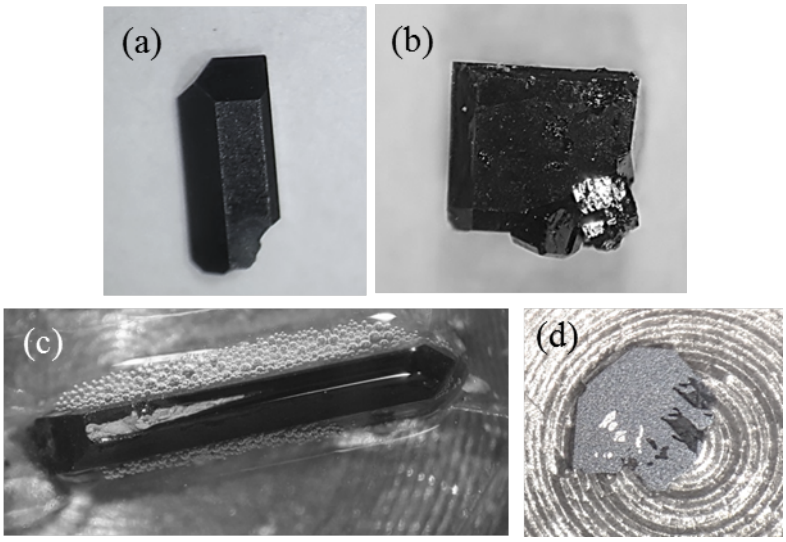

Figure 2.3: Al flux-grown samples. (a) As-grown sample showing clear crystal planes. (b) As-grown sample with 2.85% Eu doping, with polycrystals in the lower right-hand corner. (c) Al inclusions in a needle-like sample. (d) Al inclusions and voids in a sample grown with 10% Sm vacancies.

Fig. 2.3(a) and (b), respectively. Flux-grown samples are favorable because their growth takes place at equilibrium, leading to consistent crystal quality and little susceptibility to impurities and other phases. In fact, crystals of the related phase of samarium tetraboride (SmB_4) can also be produced by Al-flux growth, but attempts to grow SmB_4 often produce SmB_6 or crystals with a mixture of the two phases. [130, 133]

The main drawback to flux-grown crystals is inclusion of the flux in the samples. In SmB_6, nearly every crystal contains small pockets of Al. In our crystals, we have observed that the needle-like pieces contain needle-like Al inclusions and the plate-like pieces contain plate-like Al inclusions, as shown in Fig. 2.3(c) and (d), respectively. Literature reports also show that the Al inclusions are epitaxial to the samples and that Al and SmB_6 have the same lattice parameter at the melting temperature of Al. [107] Some reports have also suggested that Sm_3Al_{11} can be found in inclusions from flux growth, especially when an alumina crucible is used in the growth. [108] However, the lattice parameter and crystal structure of Sm_3Al_{11} [134] are quite different from those of SmB_6, and such inclusions have not been detected. Besides inclusions, flux-grown samples occasionally contain voids, twinned crystals [110] or polycrystals arising from two pieces that grew together from separate seeds in the flux. In our crystals, we have observed voids in samples grown with off-stoichiometry (Fig. 2.3(d))

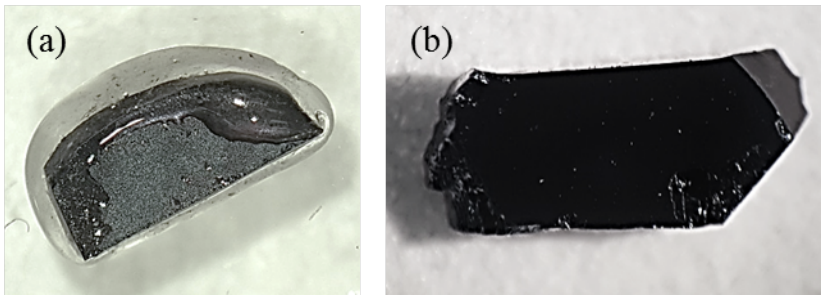

Figure 2.4: Floating zone grown samples (a) Floating zone sample grown with the single isotopes ^{154}Sm and ^{11}B. (b) Floating zone sample cleaved from larger piece.

and polycrystals in samples grown with intentional doping with other rare-earth elements (Fig. 2.3(b)).

2.4.2 Floating zone growth

Optical floating zone samples are grown at the melting point of SmB_6, which is about 2500°C. Sm and B powders are packed into a "feed rod," and a small single crystal of SmB_6, called a seed, is placed at the bottom of the rod inside a furnace. The furnace heats the tube via halogen or xenon arc lamps which are focused to the center of the rod. Starting from the seed crystal, the rod is heated to the melting point. The rod is slowly passed downwards so that the molten zone moves upwards and a crystal forms from the bottom of the rod. Like flux growth, floating zone growth is generally performed under argon gas.

An important consideration in floating zone growth is the rate at which the feed rod is passed through the molten zone. In SmB_6, slower rates tend to yield higher quality crystals with less possibility of polycrystallinity, twinning, and cracks. [109] Counter-rotating the feed rod and the already-formed crystal can also improve quality by ensuring that the components mix well in the molten zone. [135] Reports also show that passing the grown crystal, or boule, through the furnace a second or even third time can improve the quality. However, since growth occurs at such a high temperature in SmB_6, one problem that must be considered is loss of material via evaporation, which naturally becomes more of an issue the longer the boule is kept in the furnace. SmB_6 is most susceptible to loss of Sm via evaporation as Sm metal or in the SmB_4 phase. To combat this, growers often use slightly more Sm than the expected 1:6 ratio when initially preparing the growth.

Floating zone-grown SmB_6 samples can be up to 10 cm long and about 1 cm in diameter. Since they are so large, quality can still vary along the boule despite precautions taken during growth. One well-known issue is that the lattice constant decreases moving farther away from the seed crystal. [107] Changes in lattice constant in SmB_6 are known to correlate with Sm vacancies, [136] but more importantly, they imply that one-dimensional defects, or dislocations, are present.

Another possible issue affecting the quality of floating zone crystals is inconsistency in the cross-section of the boule. Floating zone growth was initially developed for one-element materials like silicon. [135] In two-element materials, one possible effect is that the center of the rod is one phase, and another phase forms an outer ring. This has never been detected in SmB_6, as the only other possible phase, SmB_4, is not the preferential product, especially under slight Sm deficiency as in floating zone conditions.

Floating zone crystals are generally preferred over flux grown crystals in experiments like neutron scattering or THz spectroscopy which require a large sample surface area. For use in transport experiments, floating zone SmB_6 must be cleaved. Due to the extreme hardness of the hexaborides, spark erosion is a commonly used technique for cleaving a boule into small pieces. [11] Examples of floating zone crystals cut to size for transport experiments are shown in Fig. 2.4.

2.4.3 Point defects and dislocations

Both Al flux and floating zone grown SmB_6 contain point defects. A major source of impurities is the samarium powder used in the growth, since rare earth materials are difficult to purify. Sm vacancies can also form during growth, and floating zone samples are more susceptible than Al flux samples due to possible material evaporation at high temperatures. This can lead to Sm vacancy concentrations of up to a few percent. While impurities are recognized, there is little consensus on the extent of their role in the physics of SmB_6.

SmB_6 also likely contains one-dimensional defects, or dislocations. Dislocations have been studied extensively in semiconductor thin films such as GaN, where they are a significant source of scattering. [137] In thin films, dislocations form during growth, especially at the interface between a substrate and a film with different lattice constants. This lattice

mismatch between the two materials strains the layer, leading to the formation of dislocations. [138] However, dislocations are also present in crystals. They can form from internal stresses in the growth, especially stresses due to thermal fluctuations, local impurities in the growth, or even vibrations in the environment. [138] Impurities in the growth can provide nucleation sites where dislocations start to form, and high temperatures used in the growth can compound the effect of internal stresses as well. [139] Additionally, dislocations can extend from a seed crystal containing dislocations to new growth based on that seed. [139] Dislocations are almost certainly present in SmB_6, although they have not been well-studied. Preliminary investigations of dislocations in SmB_6 will be presented in Chapter 5.

2.5 Preparation of crystal surfaces

As-grown surfaces of single crystal SmB_6 and cleaved surfaces of floating zone-grown SmB_6 are typically large enough that transport experiments could be performed directly. However, with the prediction that SmB_6 could be a topological insulator, having a well-defined transport geometry becomes very important for understanding surface conduction. A rough surface would have a larger total surface area than a smooth surface, so smoothing the surface via polishing helps ensure that the transport geometry is well-defined.

However, simple polishing does not achieve this goal in SmB_6. Polishing, especially rough polishing (done by a lapping machine, for example), places stress on the crystals and causes cracks to develop under the surfaces. [140] In a topological insulator all surfaces would be conductive, and these cracks provide extra surfaces. This means that subsurface cracks also contribute to uncertainty in the geometric factor for transport, and that surface preparation is essential in understanding electrical transport.

To polish our samples, we used SiC grits and aluminum oxide slurry. The roughest grit, P1200 (10.6 microns) was used for thinning or removing sharp edges from as-grown crystals, as needed. Then, samples were polished with smaller grit sizes, P2500 (3.8 microns) and P4000. Finally, the aluminum oxide slurry (0.3 microns) was used until no defects could be seen under 10x magnification. When Hall bar geometry was used, the top, bottom, and sides were polished using this method, and when van der Pauw geometry was used, the top

and bottom surfaces were polished.

Some reports have additionally proposed that etching in dilute nitric acid may improve surface quality in SmB_6, removing any Sm oxide that may have formed as well as a thin layer of the sample itself. [141] This method would be especially useful in as-grown or roughly polished samples. We also tested etching on one of our samples that had been finely polished as described above, but we found no significant difference in the transport characteristics before and after etching.

2.6 Defining transport geometry

After polishing and etching, contact pads are deposited on the sample in the appropriate transport geometry. To prepare a sample with Corbino disk geometry, standard photolithography techniques at the Lurie Nanofabrication Facility are used. The CEE 100 manual spinner is used to deposit S1813 photoresist with a thickness of 1.3 microns on the sample. Then, the Corbino pattern is exposed using the MJB-3 contact aligner with an exposure time of 6 seconds. The exposure is developed in AZ726 on the CEE developer. Then, the sample is cleaned in the YES plasma stripper to ensure that no organics remain in the area where contacts will be deposited. The contacts are metallized in the Enerjet evaporator with 50 Å titanium and 1500 Å gold. Liftoff is performed using acetone in an ultrasonic tank.

A challenge when performing photolithography on SmB_6 crystals is the size of the crystals. Most clean room processes are optimized for wafers, but SmB_6 crystals are usually no more than a few mm on a side. One of the primary challenges is in spinning the sample. Due to the small size, a thicker section of photoresist, known as a bead, can form on one edge of the sample. If the Corbino pattern is placed over the bead, the exposure and development recipes will be unsuccessful. To prevent beads, some samples are polished while surrounded by pieces of glass or Si to create a single larger piece. When this is done, the bead usually forms on the Si or glass pieces rather than on the sample.

For Hall bar and van der Pauw geometry on SmB_6, it is challenging to use a single mask as the single crystals have a variety of sizes. Instead, the contacts are defined by painting the sample with S1813 photoresist such that only the areas that will be metallized are exposed,

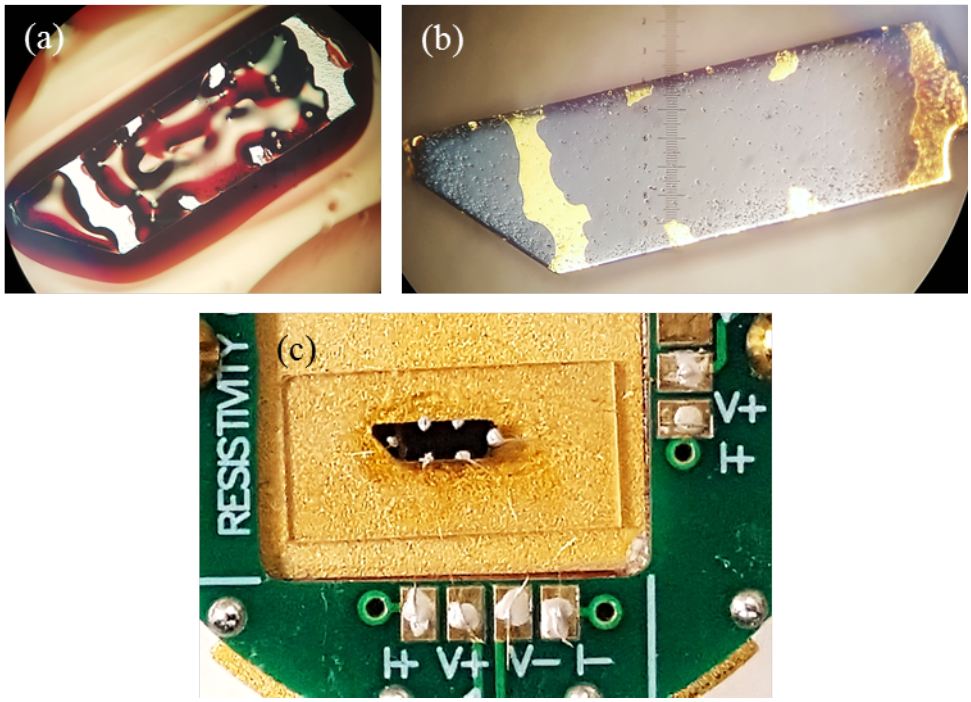

Figure 2.5: (a) Painted photoresist on a Hall bar sample. (b) Contacts after metallization. (c) Wiring with silver paste and gold wires.

as shown in Fig. 2.5(a). These samples are cleaned and metallized using the same recipes as for the Corbino disk. An example of completed contact pads is shown in Fig. 2.5(b).

Although painting can be useful, a drawback is that the contacts do not have perfectly uniform shapes or sizes. Contacts made with painting are usually 200 to 250 μm on a side, but they are not necessarily square (for Hall bar) or triangular (for van der Pauw). The finite size of the contacts leads to an imperfect geometry which can have an effect of up to 10% on the measurements, and the nonuniform shape makes it difficult to calculate the appropriate corrections. The placement of the contacts can also be challenging. When contacts used to measure Hall coefficient are not at an equipotential, the data has some offset, although this can easily be corrected for in analysis. To improve alignment and uniformity of contact size, one of the samples presented in this work was prepared using e-beam lithography (with assistance from LNF staff). Another option is to use shadow masking rather than painted photolithography to cover the non-metallized regions, although this technique was not used in this work.

Once contact pads are defined, gold wires are attached using silver paste, indium, or wire

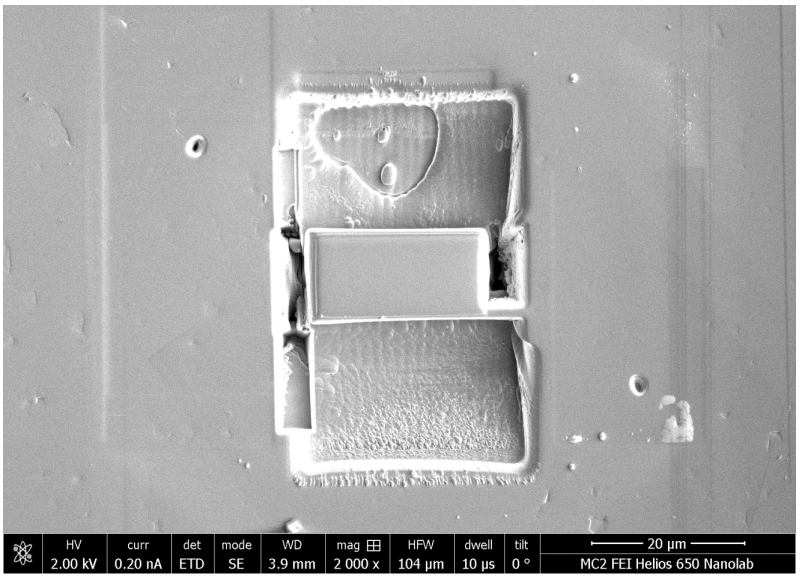

Figure 2.6: Top view of sample showing the preparation of the micro Hall bar with milling pits and carbon protection.

bonding. Wire bonding is ideal for Corbino disks as the width of each contact can be quite small. For Hall and van der Pauw samples, hand wiring with silver paste is simplest to work with and was used for the majority of measurements. An example is shown in Fig. 2.5(c). Indium provides a stronger contact, so it was used in some cases to prevent the leads from breaking during the measurements. Both silver paste and indium contacts are deposited by hand, and it is important to stay within the boundaries of the contact pads to avoid further compounding the geometry problems of hand-defined contact pads.

2.7 Preparing micro-Hall bars with a focused ion beam

Micro Hall bar preparation was performed at the Michigan Center for Materials Characterization at U-M, and we used both an FEI Helios 650 NanoLab DualBeam and an FEI Nova 200 NanoLab DualBeam. Both tools are equipped with an electron (SEM) column and a focused ion beam (FIB) column with a gallium beam. The tools each include an OmniProbe manipulator and carbon and platinum injectors, among other imaging and characterization attachments.

First, a clean region of about 30 μm x 15 μm of the crystal surface is selected. In the

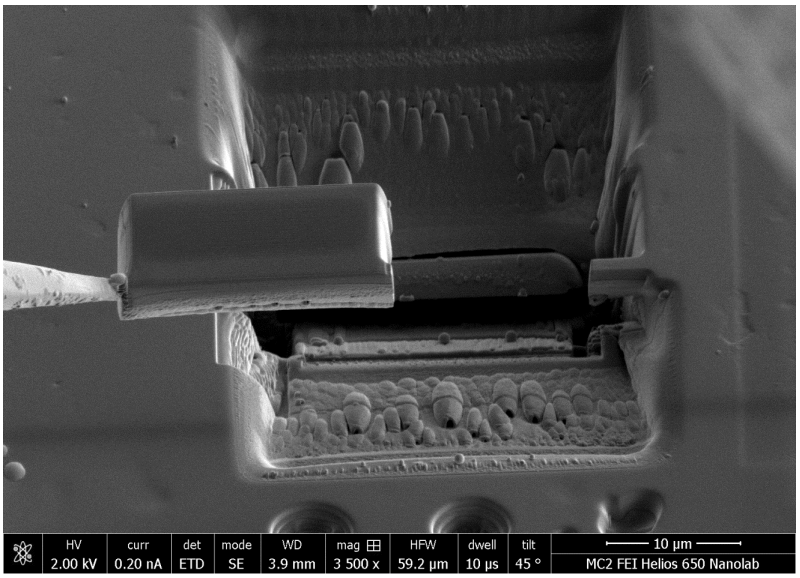

Figure 2.7: Liftout of of the micro Hall bar using the OmniProbe manipulator.

clean region, first the SEM and then the FIB are used to deposit layers of carbon to serve as a protective layer from FIB damage. The carbon is 20 μm x 10 μm, with a thickness of about 1 μm. Then, the FIB is used to mill material around the sides of the protected area. The sample is tilted and the FIB is used to cut underneath the sample, forming a triangular section extending down into the crystal. Fig. 2.6 shows a sample after these milling steps have been completed.

Next, the OmniProbe manipulator is used to remove the piece from the crystal (Fig. 2.7) and attach it to a TEM grid. Once on the TEM grid, the piece is milled to the desired geometry with a thickness of about 2 μm, and the protective layer of carbon is trimmed from the sample. An example of a thinned sample on the TEM grid is shown in Fig. 2.8. Finally, the OmniProbe manipulator is used to transfer the sample from the TEM grid to a Si chip with prepared lithographic (Ti/Au) contacts. Platinum is deposited to connect the sample to the lithographic contacts and to define the transport geometry of the sample. An example of a completed sample is shown in Fig. 2.9.

This process is closely related to standard TEM sample preparation performed in the same instrument. However, a key difference is the orientation of the sample. TEM samples are prepared with the largest surface perpendicular to the surface of the original crystal, but our micro Hall bars are prepared with the 20 μm x 10 μm surface taken directly from the

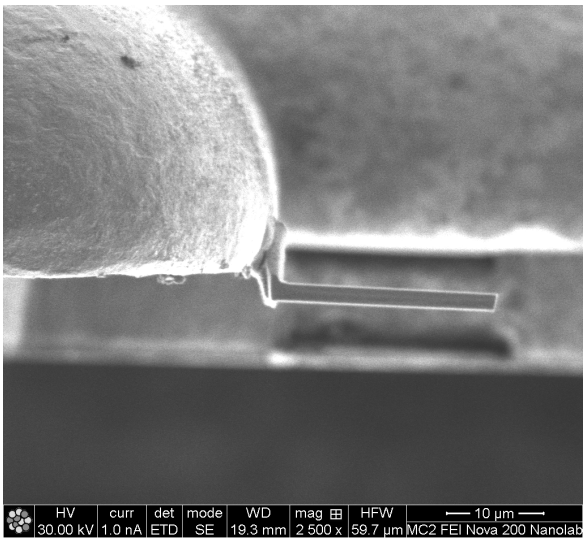

Figure 2.8: Thinned sample attached to TEM grid finger. The lower part of the piece was formerly the top surface of the crystal where carbon was deposited.

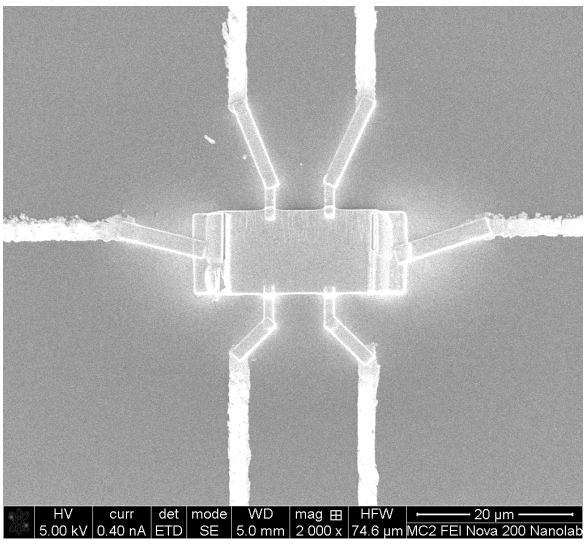

Figure 2.9: Pt contacts and pre-defined Ti/Au lithography on the micro Hall bar and the Si chip.

surface of the original crystal.

An important consideration in both TEM preparation and in our micro Hall bar process is the effect of beam damage. It is well-known that the ion beam can damage the sample surface, primarily through deposition of Ga ions into the crystal. This always causes the formation of a deformed or amorphous layer at the sample surface, but it can also induce point defects or dislocations. In semiconductors, the layer is reported to have a thickness of about 1 nm to 50 nm depending on the material and the beam parameters. For example, reducing the beam energy and rotating the beam angle away from normal to the sample surface can reduce the thickness of the layer. Reducing the beam current used can also prevent Ga implantation in the form of point defects. [142, 143, 144]

In the process described here, beam damage is not anticipated to be especially problematic, as certain steps have been implemented to account for it. First, the carbon layer deposited initially acts as a buffer against the very high beam currents used to perform the milling shown in Fig. 2.6. In addition, the final thinning steps are performed at a low beam current to prevent point defects. Based on the beam energies used in our process, we expect a damaged layer of about 20 nm thickness. In a 2 μm thick micro Hall bar, ion damage would affect 1% to 1.5% of the thickness of the sample on each surface. Because of this, our micro Hall bars are not suitable for surface studies, but they can still be used to characterize bulk properties.

Eight micro Hall bars were attempted; only two were successfully transferred to the Si chip with prepared contacts. The majority of the failed samples were dropped or damaged during transfer of the milled sample to the Si chip. Due to the steps required to process each sample, the final transfer had to be completed with the chip at 45°. Some samples slid off because the stage couldn't be moved to check if the welding was secure before moving the stage back to 0°. Other samples were unintentionally milled at a slight angle compared to the chip, and could only be welded on one corner. The OmniProbe could be used to gently press the sample flat, but in some cases the stress was too great and the sample snapped off. Besides these technical challenges, one sample disconnected from the TEM grid between sessions, and another detached from the OmniProbe during retraction and insertion.

Of the two samples for which the entire process was completed, one failed to make proper

electrical contact between enough the Pt deposits and the Ti/Au pads; this sample was tested using three leads but no conclusive results were obtained. The one successful sample was measured to obtain R_{xx} and R_{xy}. Results will be presented in Chapter 3. This sample (shown in Fig. 2.9) had visible milling marks on it, so only bulk properties could be tested.

Chapter 3

Bulk Transport Model from 4-40 K: Band Bending in the Presence of a Clean Gap

3.1 Introduction

In this chapter, a model for bulk transport in SmB_6 between 4 K and 40 K will be presented. This work was previous published in Physical Review B, vol. 95, p. 195133 in 2017. [145] In this temperature range the Kondo gap is fully formed and activated behavior is consistently observed, and bulk conduction is the dominant transport channel. As discussed in the introduction, within this temperature range, two activated regions can be observed, separated by a feature at around 10-15 K. The activated region from about 4-10 K yields an activation energy of about 3 meV and is associated with historical transport measurements. The region from about 15-40 K yields an activation energy of 5-10 meV and could correspond to the 20 meV gap consistently seen in spectroscopic measurements. One common picture is of a 20 meV gap with an impurity state about 3 meV below the conduction band, [111], although other proposals like a small indirect gap but a larger direct gap have also been proposed.

Here, we consider the bulk electronic structure of SmB_6 to be semiconductor-like and host a clean gap. Additionally, the effects of a metallic surface, regardless of whether this surface

is of a topological or trivial origin, is explored. This problem is analogous to band bending near a Schottky barrier in semiconductors. The effects of band bending in SmB_6 is considered in different temperature ranges and connected to measurable transport parameters including the Hall coefficient. The calculated results are compared to experiment and we find that band bending reproduces a feature at about 10-15 K in transport. Finally, methods of testing whether band bending is actually present in SmB_6 are discussed. Improvements on understanding the SmB_6 gap since the publication of this work are also included.

3.2 Bulk transport and the effective mass approximation

Before discussing some of the unusual properties of SmB_6 that arise from its small gap and hybridized bands, it is instructive to discuss bulk transport in standard topological insulators (TIs). Such "standard" TIs (for example, Bi_2Se_3 or Bi_2Te_3) are characterized by a bulk band gap as in conventional semiconductors, and after undergoing the crossover to the topological phase, there are an odd number of surface states located in the gap. [68, 146] If the topological surface states are not considered, all standard TIs can be treated as semiconductors. In this picture, charge neutrality must be enforced, so the Fermi energy (E_F) is initially expected to be exactly halfway between the top of the valence band and the bottom of the conduction band. As in semiconductors, impurity states may also be present in the gap. For an n-type material, donor states would be in the gap near the conduction band, and for a p-type material, acceptor states would be in the gap near the valence band. Because charge neutrality must also be enforced, the presence of these extra states shifts E_F towards the conduction band for donor states and towards the valence band for acceptor states. [147]

Impurity states in semiconductors and standard TIs can be treated quantitatively using the effective mass approximation. [148] In this picture, impurities are assumed to be hydrogenic, but with the substitution of effective mass for electron mass ($m \rightarrow m^*$) and dielectric

constant for vacuum permittivity ($\varepsilon_0 \to \kappa\varepsilon_0$). The results are an effective Bohr radius

$$a_B^* = \frac{4\pi\kappa\varepsilon_0\hbar^2}{m^* e^2} = \frac{\kappa}{m^*/m}(0.53\ \text{Å}) \tag{3.1}$$

and an effective ground-state energy

$$E^* = -\frac{m^* e^4}{2(4\pi\kappa\varepsilon_0)^2\hbar^2} = -\frac{m^*/m}{\kappa^2}(13.6\ \text{eV}). \tag{3.2}$$

Once these parameters have been calculated, the initial assumption of hydrogenic impurities can be verified. In a donor state, for example, the extra electron must have an extent much larger than one lattice constant for the donor to be hydrogenic. If this were not the case, contributions from the donor itself would also have to be considered, and the hydrogen model could not be used. Therefore, when comparing the effective Bohr radius to the lattice constant, we must satisfy the condition $a_B^* \gg a$ for the approximation to be valid.

The effective mass approximation has been used successfully in all standard TIs. Standard TIs exhibit residual bulk conduction after undergoing the crossover to the topological state, and this is well-understood as arising from impurity states that can be treated using the effective mass approximation. Many researchers have applied the idea of impurity states in the gap to SmB_6 to try to understand the plateau at 4 K before it was thought to be a TI, [3] and later to explain experimental discrepancies in the size of the Kondo hybridization gap. While the presence of the gap is well-known, transport and spectroscopic methods disagree on the size. Transport measurements, which probe the energy difference between E_F and the conduction band (the activation energy), report 3-4 meV. [9, 29, 10, 16, 15] In analogy with semiconductors and standard TIs, it is expected that E_F is exactly halfway between the valence and conduction bands, suggesting that the total transport gap is 6-8 meV. On the other hand, spectroscopy and tunneling experiments measure the full gap near the surface, and they report 16-20 meV. [113, 111, 20, 149, 150, 151, 112]

This discrepancy has been interpreted as arising from the presence of in-gap bulk impurity states. [8, 151, 149, 150, 152, 111, 114, 113, 75] In this scenario, transport would measure the difference between the impurity state and the conduction band, yielding an incorrect result for the total gap. Since the effective mass approximation is usually so successful, it has

been applied to SmB_6 to understand this proposed in-gap impurity state. However, reported values [111, 151] of the dielectric constant κ range from 600-1500, and as we have seen, activation energy (which can be used to obtain effective mass) ranges from 3-10 meV. Using these values with Eqs. 3.1 and 3.2, we obtain a minimum a_B^* of 0.5 Å and a maximum a_B^* of 4 Å. Reports of the effective Bohr radius are usually in this range; for example, Sluchanko *et al.* report 3 Å. [152] Additionally, most reports agree that the lattice constant a of SmB_6 is about 4.13 Å, so we find that the condition $a_B^* \gg a$ required to verify the effective mass approximation is not satisfied anywhere in the range of Bohr radii that can be calculated. Because the effective mass approximation fails, in-gap hydrogenic impurity states in SmB_6 are not justified.

Since semiconductor theory and the effective mass approximation are successful in most cases, this result is startling. However, upon closer examination, we find that it is perhaps not completely unexpected. Because the gap in SmB_6 arises due to hybridization, its band structure is very different from that of a conventional semiconductor. Unlike a semiconductor, SmB_6 has a non-quadratic and asymmetric dispersion, because its band structure arises due to Kondo hybridization. Both the valence and conduction bands have nearly flat regions characterized by the localized f states as well as low-mass regions characterized by the d states. Because of this unusual composition, while the gap and band structure effects in SmB_6 arise based on contributions from all the carriers, transport is dominated only by the low-mass carriers. Additionally, both bands have positive curvature, unlike in a semiconductor, where only the conduction band has positive curvature. As we will see, this has a significant effect on how we understand transport. The gap is also much smaller than that of standard semiconductors or TIs. Because of these differences in the band structure, we will see that SmB_6 must be treated much more carefully than standard gapped materials. (In contrast, other hexaboride materials can be treated as standard gapped materials, and in these cases, impurity states are present within the bulk gap. [153])

In the context of in-gap bulk states, we can gain insight into SmB_6 by analogy with superconductors. When a material undergoes a transition to a superconducting state, some of the electrons near the Fermi energy condense into Cooper pairs. Formation of the condensate opens up a gap at the Fermi energy. [154] Even though this gap is so small, tunneling

measurements [155] have shown that the addition of impurities to a superconductor does not destroy superconductivity (until the impurity concentration becomes sufficiently high). This suggests that the impurity states are not in the gap, or that superconductors exhibit a small and clean gap and are not vulnerable to impurity conduction. Although the mechanism for gap formation (the Kondo effect) is very different in SmB_6, the gap is also much smaller than a semiconductor bulk gap. This, combined with the failure of the effective mass approximation, suggests that SmB_6 should have a clean gap that is not vulnerable to impurity conduction at low temperatures. In fact, SmB_6 does not exhibit residual bulk conduction experimentally, and this can be taken as evidence for a clean bulk gap. [15]

Another interpretation of the gap discrepancy is that spectroscopy measures the direct gap while transport measures an indirect gap that forms during hybridization. Theoretical treatments of Kondo hybridization predict the presence of both a direct and an indirect gap, [119, 156, 70] and researchers have also used this idea to explain the gap discrepancy. [10, 112] This interpretation explains the gap discrepancy while avoiding the problem of the in-gap impurity states, but we will propose an alternative explanation that is consistent with features observed in transport. As we have seen, in-gap impurity states in SmB_6 are not justified by the effective mass approximation, nor are they consistent with the observation of no residual bulk conduction after the surface states become relevant. To achieve consistency, we propose another explanation of the gap discrepancy that does not rely on in-gap states and instead allows for a clean direct gap.

3.3 Simplified density of states and band bending calculations

3.3.1 Density of states

The dispersion in SmB_6 is well-known based on the success of recent high-resolution ARPES measurements. [22, 19, 21] The gap forms at low temperature, when the conduction band ($5d$) hybridizes with localized states ($4f$). In SmB_6, there are three $4f$ bands, and ARPES indicates that only one band participates in hybridization. A sketch of the band structure

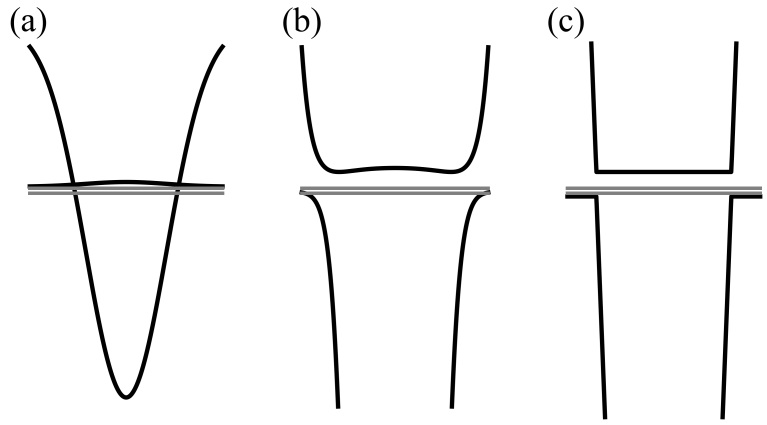

Figure 3.1: Dispersion relation of SmB_6 along the $\Gamma - X - \Gamma$ direction, focused where the hybridization takes place. (a) Band structure before hybridization. (b) Band structure after hybridization of the d band with one of the f bands. The vertical axis (energy) scale is zoomed in from the scale in (a). (c). Simplified band structure used in the calculation. The vertical scale is the same as in (b).

of SmB_6 before hybridization is shown in Fig. 3.1(a), and the hybridized band structure is shown in Fig. 3.1(b), both along the $\Gamma - X - \Gamma$ direction. SmB_6 is an insulator, so the Fermi energy is located in the gap in the hybridized band structure. As can be seen in the figure, the two unhybridized f bands are still present.

In addition to this basic structure, the hybridized dispersion has some subtle features, which can also be observed by ARPES. For example, ARPES demonstrates an indirect gap with a valence peak about 15 meV below the Fermi energy at the H point. [22] This feature can also be observed at nearby energies due to intrinsic and thermal broadening. Compared to the main features of the dispersion, however, this feature is small and close to the valence band. Although ARPES cannot probe far into the conduction band at the temperatures we are considering, there are likely some similarly small features present in the conduction band. We refer to the regions in which such small features exist as the "region of non-parabolicity."

In our model, we will use a dispersion that is simplified considerably from the actual dispersion. We neglect the small features in the region of non-parabolicity, such as the feature at the H-point and any similar features in the conduction band. To do this, we approximate the band structure using a piecewise function, as shown in Fig. 3.1(c). Here, the flat regions approximate the pieces of the hybridized dispersion that primarily come from

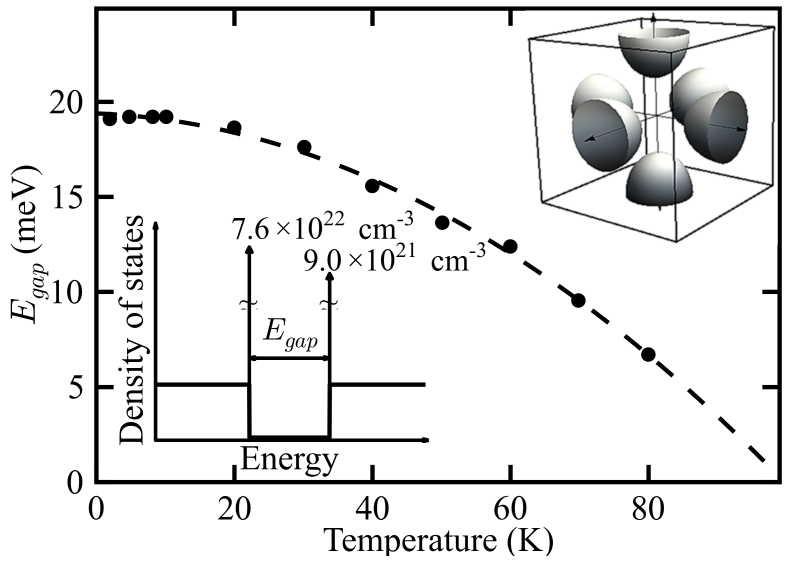

Figure 3.2: Parameters used in the calculation. Main plot: Data [112] for dependence of the gap size on temperature and a best fit (dashed line). Lower left inset: Simplified density of states used in the calculation. Upper right inset: Fermi surface and Brillouin zone of SmB_6 after hybridization. [71]

the $4f$ band, which we refer to as "f-like" states. The linear regions approximate the pieces of the hybridized dispersion that primarily come from the $5d$ band, which we call "d-like" states. Additionally, the two unhybridized $4f$ bands cannot be resolved separately from the valence band by ARPES, so we approximate them to be at the top of the valence band. Making these approximations introduces some error into the model, but the features in the region of non-parabolicity are small, so the error is not more than a few meV.

From this dispersion, we can calculate a simplified density of states (DOS). The DOS corresponding to our simplified dispersion (Fig. 3.1(c)) is shown in the lower inset of Fig. 3.2. In this figure, the peaks in the DOS correspond to the f-like regions of the dispersion, and these can be estimated from the size of the pockets in the SmB_6 Brillouin zone (BZ), shown in the upper inset of Fig. 2. The flat parts of the DOS correspond to the d-like regions of the dispersion. In the range E_{gap}, the DOS is zero, and the gap changes with temperature. Data for the gap as a function of temperature [112] is shown in Fig. 2, as is the fit to this data that was used in the calculation (dashed line).

We can represent the simplified DOS using delta functions (δ) for the f-like states and

step functions (θ) for the d-like states:

$$g(\epsilon) = N_{cf}\delta(\epsilon - E_C) + g_{cd}\theta(\epsilon - E_C) + N_{vf}\delta(\epsilon - E_V) - g_{vd}(\theta(\epsilon - E_V) + 1) \tag{3.3}$$

where E_C is the edge of the conduction band, E_V is the edge of the valence band, N is a density in cm^{-3}, g is a DOS in $\mathrm{cm}^{-3}\cdot\ \mathrm{eV}^{-1}$, and the Fermi energy E_F has been set to 0. The subscripts on the four factors refer to electron type and band; e.g. N_{cf} is the density of states for f-like electrons in the conduction band (c). The Fermi energy, which is in the gap, is defined to be zero.

The sizes of these four terms can be estimated using ARPES data. [71] According to this measurement, the hybridized f band BZ has six half-ellipsoid Fermi pockets (upper inset of Fig. 3.2), and the total volume of these yields the number of filled states in the conduction band, which we will denote n_{ell}. This implies that

$$N_{cf} = n_{ell} = 9.0 \times 10^{21}\ \mathrm{cm}^{-3}. \tag{3.4}$$

The remaining volume in that BZ, plus the total volume of the BZs for the two unhybridized f bands, yields the valence band contribution. We will denote the volume of the BZ as n_{BZ}, so this implies that

$$N_{vf} = 3n_{BZ} - n_{ell} = 7.6 \times 10^{22}\ \mathrm{cm}^{-3}. \tag{3.5}$$

The d-like states can be calculated from data above the hybridization temperature. [71] We approximate the dispersion to be quadratic and use the usual result for a 3D quadratic DOS,

$$g_{3D}(\epsilon) = \frac{m^*}{\pi^2\hbar^3}\sqrt{2m^*\epsilon} \tag{3.6}$$

In our simplified DOS we can approximate the d bands on both sides of the gap as constant. Specifically, we approximate this constant to be $g_{3D}(E_F)$, because E_F is in the gap and the gap is small. This also means that this value in both bands is about the same constant,

$$g_{cd} \approx g_{vd} \approx g_{3D}(E_F) = 1.8 \times 10^{19}\ \mathrm{cm}^{-3}\ \mathrm{eV}^{-1}. \tag{3.7}$$

We note that this term is 2-3 orders of magnitude smaller than the terms in Eqs. 3.4 and 3.5. We will define this value as g_0 for brevity.

3.3.2 Band structure calculation

As we have seen, the actual and simplified dispersions as well as the DOS of SmB_6 can be characterized by two types of carriers. The flat regions are dominated by f-like carriers, and the remainder is dominated by d-like carriers. In this section, we will outline a self-consistent calculation used to obtain the band structure. For such a calculation, we must take all the charges into account. However, the f-like terms (Eqs. 3.4 and 3.5) are 2-3 orders of magnitude greater than the d-like coefficients (Eq. 3.7). To get the total charge density, the d-like states require a factor of k_BT, so they become even smaller; because of this we neglect the d-like carriers for the band structure calculation. However, we will later see that transport is governed by the low-mass, d-like carriers.

The charge density can be calculated using usual methods for semiconductors. In semiconductors, the conduction band is nearly empty, so the Fermi-Dirac distribution $f^0(\epsilon)$ can be approximated by the Boltzmann distribution. The electron density is

$$n = \int_{E_C}^{\infty} f^0(\epsilon) g(\epsilon) d\epsilon = n_0 \, e^{-(E_C - E_F)/k_BT} \tag{3.8}$$

where n_0 is the average DOS. In SmB_6 we use Eq. 3.3 for the DOS, keeping only the delta function terms. This yields electrons in the conduction band with approximate density

$$n \approx N_{cf} \, e^{-(E_C - E_F)/k_BT}. \tag{3.9}$$

We can similarly calculate the approximate density of holes in the valence band to be

$$p \approx N_{vf} \, e^{-(E_F - E_V)/k_BT} \tag{3.10}$$

where E_V is the valence band edge. This result resembles the carrier density of a conventional semiconductor. For such semiconductors, charge neutrality, $n = p$, yields the intrinsic carrier

density

$$n = p = n_i \approx \sqrt{N_{cf} N_{vf}}\, e^{-E_{gap}/2k_B T}. \tag{3.11}$$

The intrinsic picture works well for SmB_6 at high temperatures. However, intrinsic materials are sensitive to surface effects, and at low temperature, these become relevant. All surface charges, such as TI states, if they are present, and localized surface charges associated with oxidation on the surface, contribute. Requiring charge neutrality with the addition of the surface charges forces the Fermi energy to be pinned in place, leading to band bending in the valence and conduction bands. This possibility has been suggested by recent experimental results, [157] but was not previously explored in depth.

To understand the effects of band bending, we perform a self-consistent calculation to obtain the band structure. In this calculation, we model the effects of band bending using a potential $\phi(z)$ of the form

$$e\phi(z) = E_C(z) - E_{gap}/2 \tag{3.12}$$

where the conduction band is now dependent on location z in the bulk, and $E_{gap} = E_C - E_V$. We can rewrite the carrier densities in terms of this potential to obtain

$$n(z) = N_{cf} \exp\left[-\frac{e\phi(z) + E_{gap}/2 - E_F}{k_B T} \right] \tag{3.13}$$

and a similar expression for $p(z)$. Using charge neutrality again, we obtain

$$\rho(z) = -en(z) + ep(z) = 2n_i e \sinh\left[\frac{e\phi(z)}{k_B T} \right] \tag{3.14}$$

for the total charge density. We then solve for the potential across the bulk using Poisson's equation in one dimension,

$$\frac{d^2\phi}{dz^2} = \frac{\rho(z)}{\varepsilon} = \frac{2n_i e}{\varepsilon} \sinh\left[\frac{e\phi(z)}{k_B T} \right]. \tag{3.15}$$

To solve this equation, we choose a "test sample" of thickness 200 μm, which is typical to a real SmB_6 sample. We define $z = 0$ as the center of the sample (so that $z = \pm 100\,\mu$m are the edges). In addition, we use $\kappa = 600$ as the dielectric constant. [111] To proceed

with the solution, we now require boundary conditions. For the first boundary condition, we simulate the band bending effects on the surface by introducing a pinning energy E_{pin}, which is defined with respect to the midpoint of the gap by $E_{pin} = (E_C + E_V)/2 - E_F$. This describes the energy difference between the band at zero potential and the minimum of the bent band. Therefore, the boundary condition can be expressed as $e\phi(z = 100\,\mu m) = -E_{pin}$. We can also define this pinning relative to the gap as $E_{pin} = E_{gap}/2 - E_a$. As we will see later, when temperature is sufficiently low, E_a corresponds to the activation gap measured by transport. The pinning energy must also be the same at both edges of the sample, and to enforce this, the second boundary condition is that $d\phi/dz = 0$ at $z = 0$, the center of the sample.

Additionally, we can define a "built-in potential," V_{bi}, as is commonly done for band-bending calculations in semiconductors. [147] V_{bi} describes the magnitude of the bending in terms of the difference between the maximum and minimum points on the conduction or valence band. Using this built-in potential, we can determine an associated length scale (the accumulation length) of Eq. 3.15, given by

$$l = \sqrt{\frac{2\epsilon V_{bi}}{e n_i}} = \sqrt{\frac{2\epsilon V_{bi}}{e(N_{cf}N_{vf})^{1/2}}}\, e^{E_{gap}/4k_BT}. \tag{3.16}$$

At low temperature, when E_{gap} is large, the accumulation length is large, and at high temperature, when E_{gap} is small, the accumulation length is small.

With these parameters, solutions to Eq. 3.15 were found for temperatures of 4-40 K and values of E_{pin} between 4 and 7 meV. From a solution $\phi(z)$, the conduction and valence bands can be obtained from Eq. 3.12, and the charge density can be obtained from Eq. 3.14. An example of these are shown for 8 K and $E_{pin} = 5.5$ meV in Fig. 3.3. Fig. 3.3(a) shows the calculated conduction and valence bands, as well as the relationships among the band structure and the parameters E_{pin}, E_{gap}, E_a, and eV_{bi}. We note that the valence band is always parallel to the conduction band and can be obtained by subtracting $E_C(z) - E_{gap}$. Because of this symmetry, the following discussion will be confined to the conduction band, although it will also apply to the valence band. Fig. 3.3(b) shows the calculated charge density corresponding to this band structure. Across the sample, the charge density is

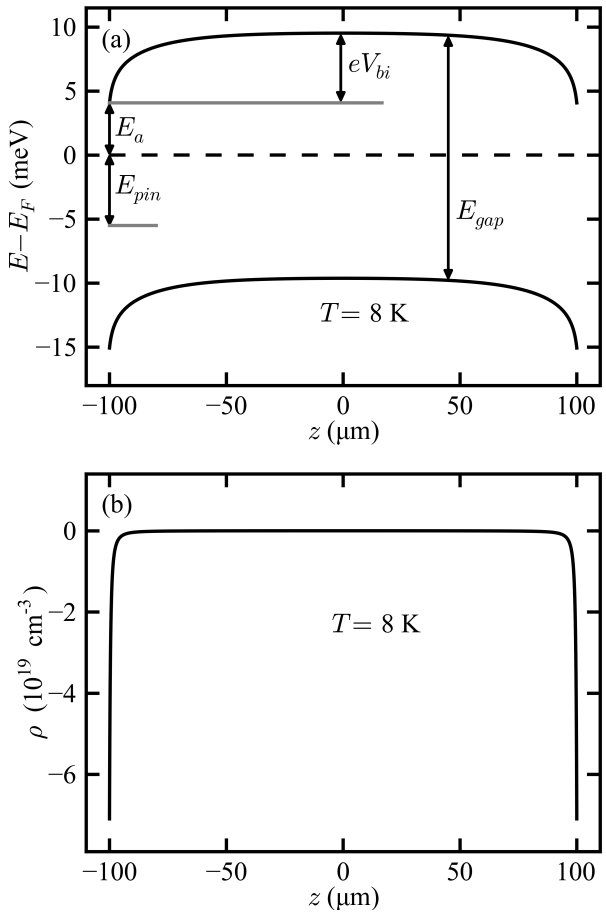

Figure 3.3: Parameters obtained from the self-consistent solution for $\phi(z)$ in a 200 μm sample with $E_{pin} = 5.5$ meV and $T = 8$ K. (a) Band structure obtained using Eq. 3.12. The relationship among the activation energy E_a, the built-in potential eV_{bi}, the pinning E_{pin}, and the gap E_{gap} are all shown. (b) Charge density obtained using Eq. 3.14.

negative, and its magnitude is largest near the surfaces. This is expected, because excess charge at the surfaces leads to band bending.

Fig. 3.4 shows how the band structure varies with temperature, again using $E_{pin} = 5.5$ meV; the valence band is omitted. At 12 K, the highest temperature shown, the conduction band for the majority of the bulk is $E_{gap}/2$ above the Fermi energy. There is a small amount of band bending at the edges, but it does not extend very far into the bulk, as expected from Eq. 3.16. This means that the band structure is similar to that of a standard gapped material, except near the surface. As the temperature is lowered, however, the band bending effects begin to extend farther into the bulk. At 2 K, the lowest temperature shown, these effects completely dominate the band structure. Here, the conduction band is much closer to the Fermi energy than the valence band is, and this result is very different from what is observed in a standard gapped material.

This process demonstrates a crossover between bulk conduction dominated by the usual bulk effects (at high temperatures) and bulk conduction dominated by surface effects (at low temperature). We can understand where the crossover occurs by comparing the charge densities and relevant length scales. At high temperatures, the bulk dominates bulk transport, and this can be characterized by the size of the sample (t) and the intrinsic carrier density (n_i). At low temperatures, the surface dominates bulk transport, and this can be characterized by the accumulation length (l) and the carrier density on the surface (n_s). From this, we can estimate the crossover as occurring when $tn_i \approx ln_s$. In our calculation, we estimate that the crossover occurs at about 10-15 K. Since the crossover depends on the relationship between the accumulation length and the sample, the crossover temperature is dependent on the thickness of the sample. For example, in a much thinner sample such as a thin film, the crossover would occur at a higher temperature than we have estimated in this calculation.

These band bending results and the crossover are able to explain the gap discrepancy between transport and spectroscopy. In our picture, spectroscopy still measures the full gap, which does not change based on where the measurement occurs in the sample. Transport, on the other hand, measures a different activation gap depending on temperature. Below the crossover, transport measures the activation gap on the surface, as shown in Fig. 3(a),

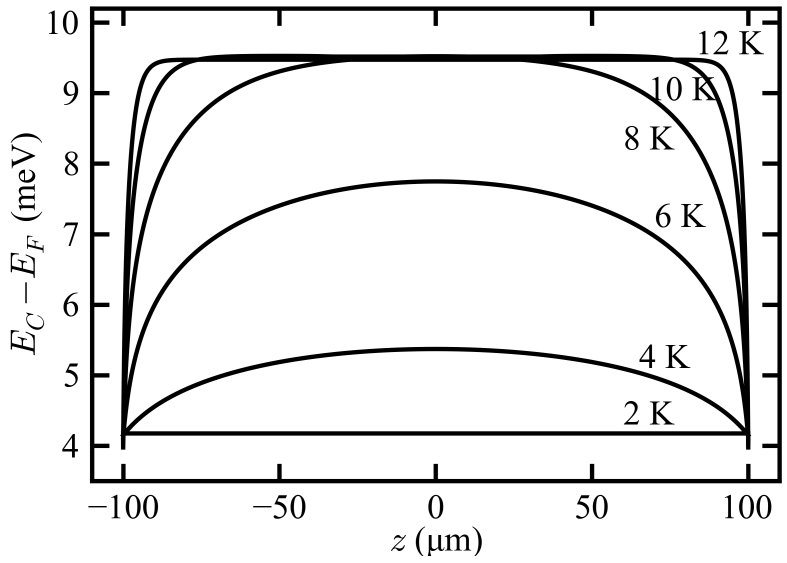

Figure 3.4: Calculated bulk conduction band at various temperatures for $E_{pin} = 5.5$ meV.

but above the crossover, transport measures the average gap across the entire bulk. As a rough estimate using our model's parameters, at 4 K the total gap is about 19 meV, and with a pinning of 5.5 meV the model yields $E_a = 4$ meV, in agreement with experiment. In this way, the gap discrepancy can be understood without using in-gap bulk impurity states.

The crossover also has interesting implications for the gap. As we have noted, the accumulation length extends through the bulk at low temperatures. As the temperature is lowered, the accumulation length diverges, and this can be thought of in analogy with semiconductors. In semiconductors, the accumulation or depletion length increases with purity, and a completely pure material would have an infinite accumulation or depletion length. [147] Our calculation shows that the accumulation length becomes large at cryogenic temperatures in SmB_6, consistent with the hypothesis that the gap is clean and the bulk is truly insulating.

We note that the effects of the surface, whether topological, trivial, or both, were all included in the parameter E_{pin}. In terms of our simulation, various surface effects including the crystal plane, polarity, disorder, TI states, or other predicted surface effects [158, 159] would simply change the value of E_{pin}. We do not predict which effects are strongest, but changes in E_{pin} due to such effects would change the strength of the band bending for the surface considered.

We further note that the Fermi energy pinning is not rigid, which means that fixing the

conduction band permanently at E_{pin} is not exact for all temperatures. Near the crossover, the Fermi energy is allowed to shift slightly. This means that competing with the surface-to-bulk crossover is a slightly shifting pinning. (If the surface effects are topological, we predict that the pinning would be more rigid than if the effects were trivial.) This type of shift does not affect the fully surface or fully bulk regions seen in the model, but if its effects were included, it would slightly change the temperature at which the crossover occurs. We have chosen not to include these effects, because the model is quite robust against changes. The band bending result is always present, and even a large variation in the parameters only slightly shifts the magnitude of the calculated effect. For example, reports of dielectric constant [111, 151] vary from 600 to 1500. When comparing these extremes in the calculation, the results above the crossover are exactly the same, and the results below the crossover differ only slightly.

3.4 Connection to experiment

To assess the validity of our model, we must connect the results of the self-consistent calculation to measurable parameters. Specifically, we examine Hall coefficient, resistivity, and thermopower, comparing the simulation results for each to data. Although we have used a semiconductor picture, SmB_6 is very different from a standard semiconductor due to its non-parabolic dispersion arising from the hybridized band structure. Because of this unusual band structure, its transport properties are unique and must be considered in detail. We must consider which carriers, d-like or f-like, contribute to transport phenomena, as well as the sign of these carriers.

In the discussion of the simplified DOS above, we saw that the f-like electrons dominate when calculating the carrier density, because their contribution to the DOS is much greater than the contribution of the d-like electrons. However, the f-like electrons have a flat dispersion, which must yield zero mobility. This means they cannot contribute to transport, so observed transport phenomena must be due to the d-like electrons. Looking back at the features of the actual band structure, we note that the f-like electrons do not have an exactly flat dispersion, and there is some curvature connecting the f- and d-like states. However,

based on ARPES data, these features are small compared to the size of the gap. [22] Thus the curvature of these features is small compared to the simplified band structure, so we can again neglect the effects.

We can understand this more quantitatively using semiclassical (Boltzmann) transport. First, we will consider the case of an intrinsic semiconductor in the conduction band to demonstrate the calculation, but the valence band result can be found similarly. We will then discuss modifications for the SmB_6 case. Using the elementary solution to the Boltzmann equation, the current due to an electric field applied in the z-direction is [160]

$$j_z = -\int_{E_C}^{\infty} v_z^2 e^2 \tau E_z \frac{\partial f^0(\epsilon)}{\partial \epsilon} g_C(\epsilon) d\epsilon \tag{3.17}$$

where v_z is the particle velocity, e is the electronic charge, τ is the scattering time, E_z is the applied electric field, $g_C(\epsilon)$ denotes the DOS for the conduction band, and ϵ is the energy. We use the relaxation time approximation, where τ is independent of energy, and the equipartition theorem, $v_z^2 = v^2/3$, to rewrite Eq. 3.17. Then, using $j_z = \sigma E_z$, we find the conductivity,

$$\sigma \approx -\frac{e^2\tau}{3} \int_{E_C}^{\infty} v^2 \frac{\partial f^0(\epsilon)}{\partial \epsilon} g_C(\epsilon) d\epsilon. \tag{3.18}$$

The derivative of the Fermi-Dirac distribution is [160]

$$\frac{\partial f^0(\epsilon)}{\partial \epsilon} = -\frac{1}{k_B T} f^0(\epsilon)(1 - f^0(\epsilon)) \tag{3.19}$$

and for a general intrinsic semiconductor, the conduction band is almost empty, so the term in parentheses can be approximated as 1. Then the conductivity becomes

$$\sigma \approx \frac{e^2\tau}{3k_B T} \int_{E_C}^{\infty} v^2 f^0(\epsilon) g_C(\epsilon) d\epsilon. \tag{3.20}$$

Since only electrons near the Fermi energy are mobile, we can approximate their velocity as the Fermi velocity v_F, and this is a constant. The remaining integral is just the usual

method for calculating carrier density, so we find

$$\sigma \approx \frac{e^2\tau}{3k_BT}\, v_F^2 n \tag{3.21}$$

where n is given by Eq. 3.8. To further simplify, we can use the Einstein relation for semiconductors, which relates the diffusion constant, $D = v^2\tau/3$, to the mobility by

$$\frac{\mu k_B T}{e} = \frac{v^2\tau}{3} \tag{3.22}$$

where μ is the mobility, v is the average velocity, and 3 represents the number of dimensions (the right-hand side of this equation can be derived using the equipartition theorem). So we find, for average velocity v_F, the familiar result, written for an intrinsic semiconductor,

$$\sigma = ne\mu. \tag{3.23}$$

In SmB_6, the picture is a little more involved. We will now re-derive the general result of Eq. 3.23 with modifications for SmB_6. First, we consider the carriers. Since there are two types of carriers (f-like and d-like), a small displacement of the Fermi surface due to an applied electric field is not uniform. For our simplified dispersion (Fig. 1c), say the field is being applied from right to left (so that electrons move from left to right). Then the electrons in d-like states on the right are mobile as they would be in a conventional semiconductor. However, the electrons in d-like states on the left are unable to move, as the f-like states are filled and have zero mobility. This means that only half of the carriers in the band can move when a current is present. Therefore we must include a factor of 1/2 relative to the usual result (Eq. 3.19).

Additionally, since only the d-like carriers contribute to transport, we should only consider the carrier density n coming from these. Using Eq. 3.8 and Eq. 3.7, we find that

$$n = g_0 k_B T e^{-(E_C - E_F)/k_B T}. \tag{3.24}$$

Now we can rewrite g_0 using Eq. 3.6. Also, the carriers should still move with an average

speed of v_F. We obtain

$$\sigma_{\mathrm{SmB_6}} \approx \frac{e^2\tau v_F^2}{6}\,\frac{m^*}{\pi^2\hbar^3}\sqrt{2m^*E_F}\,e^{-(E_C-E_F)/k_BT} \tag{3.25}$$

and this can be further simplified using $\sqrt{2m^*E_F} = \hbar k_F$ and $v_F = \hbar k_F/m^*$ to obtain

$$\sigma_{\mathrm{SmB_6}} \approx \frac{e^2\tau k_F^3}{6m^*\pi^2}\,e^{-(E_C-E_F)/k_BT}. \tag{3.26}$$

Next, we apply $k_F = (3\pi^2 n)^{1/3}$, which can be calculated by integrating to find the carrier density at zero temperature and rearranging. This means that n in this expression is the density of filled states up to E_F, and according to Eq. 3.4, this is just n_{ell}. We also use $\mu = e\tau/m^*$ to find

$$\sigma_{\mathrm{SmB_6}} \approx \frac{1}{2}n_{ell}\,e\,\mu_d\,e^{-(E_C-E_F)/k_BT} \tag{3.27}$$

where the subscript on mobility denotes that only d-like electrons are mobile.

This calculation can be repeated for the valence band, and the result is similar, except that the exponential is replaced by $\exp\left[-(E_F - E_V)/k_BT\right]$. To understand how the conduction and valence band contributions are related physically, we must consider the signs of the carriers in both bands. For a conventional semiconductor, the conduction band contributes electrons with positive effective mass and the valence band contributes holes with negative effective mass. These have opposite contributions to transport. In $\mathrm{SmB_6}$, we still have electrons in the conduction band and holes in the valence band, but both bands have positive curvature in the d-like electrons. Since we are just considering the d-like carriers, the conduction band case is the same as that of a conventional semiconductor, electrons with positive effective mass. However, the valence band has positive curvature rather than negative as it would for a conventional semiconductor. This means that although there are holes in the valence band, they have a positive effective mass as well, so they contribute with the same sign as the electrons in the conduction band.

Although this result was found by considering the simplified band structure, again we can neglect the details of the bands. For example, the H-point feature in the valence band observed by ARPES [22] shows up as a small bump with negative curvature in the f-like

part of the dispersion. As discussed previously, this feature is very close to the valence band, so although it creates some curvature in the valence band, the effect is small. This means that there are holes with negative effective mass at these points in the valence band, but we assume that the curvature is large, so that these carriers have a much smaller mobility than the d-like carriers.

Because the dominant (d-like) carriers in the valence and conduction band contribute to transport with the same sign, we can return to Eq. 3.27 and conclude that the total conductivity for all carriers in both bands is the usual result as in Eq. 3.23, with $\mu = \mu_d$, and n defined as

$$n = \frac{1}{2} n_{ell}\, e^{-(E_C - E_F)/k_B T} + \frac{1}{2} n_{ell}\, e^{-(E_F - E_V)/k_B T} \tag{3.28}$$

This means that we can use the usual transport relations to connect our model to the experimental results, provided that this expression is used to calculate the carrier density.

3.5 Transport in the model

3.5.1 Hall coeffcient and resistivity

We can now combine the results $E_C(z)$ and $E_V(z)$ of the self-consistent calculation with Eq. 3.28 to define an effective carrier density

$$n_{eff} = \frac{1}{t} \int_{-t/2}^{t/2} \frac{1}{2} n_{ell} \left(e^{-[E_C(z) - E_F]/k_B T} + e^{-[E_F - E_V(z)]/k_B T} \right) dz \tag{3.29}$$

where t is the thickness of the sample ($t = 200\,\mu$m for our test sample). We can then use this carrier density to compare the model to transport data. We first concentrate on the Hall coefficient ($R_H = 1/ne$) because it does not require any further parameters to be included; however, if we assume that mobility is constant, the resistivity follows the same trend. This is not a good assumption, as mobility is often temperature dependent, but the same feature around 10 K is seen in data for both Hall coefficient and resistivity.

Fig. 3.5 shows a plot of calculated Hall coefficient as a function of temperature for various values of E_{pin}. As in the band structure result of Fig. 3.4, we observe a crossover around

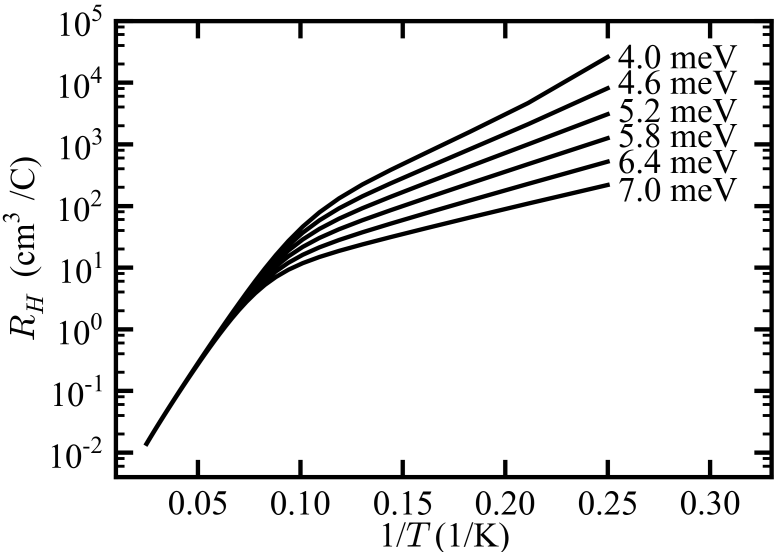

Figure 3.5: Calculated Hall coefficient as a function of temperature for different values of E_{pin}.

10 K. At temperatures above this crossover, where the bulk transport is dominated by bulk effects, all values of E_{pin} yield the same curve. This is expected because in this region, the accumulation length is always much less than the sample size, regardless of E_{pin}. Below the crossover, however, there is some variation. In this region, the amount of bending influences the accumulation length, so the magnitude of the Hall coefficient changes with E_{pin}. As mentioned previously, in this region, the activation energy can also be determined by $E_a = E_{gap}/2 - E_{pin}$.

The calculated Hall coefficient for $E_{pin} = 5.5$ meV is plotted along a collection of data in Fig. 3.6. The data agrees very well above about 10-15 K, and this agreement suggests that the bulk carrier density in SmB_6 is fairly consistent across samples. Below about 10-15 K, the data exhibits a variation of about an order of magnitude. We do not suggest a mechanism for this variation, but we do note that in this temperature range, our model suggests that the bulk conduction is dominated by the surface. Around 10-15 K, a feature is observed by all researchers, and this corresponds to the crossover discussed previously, between bulk conduction dominated by bulk effects above the crossover and bulk conduction dominated by surface effects below the crossover.

The calculated Hall coefficient from our model also demonstrates a crossover at about

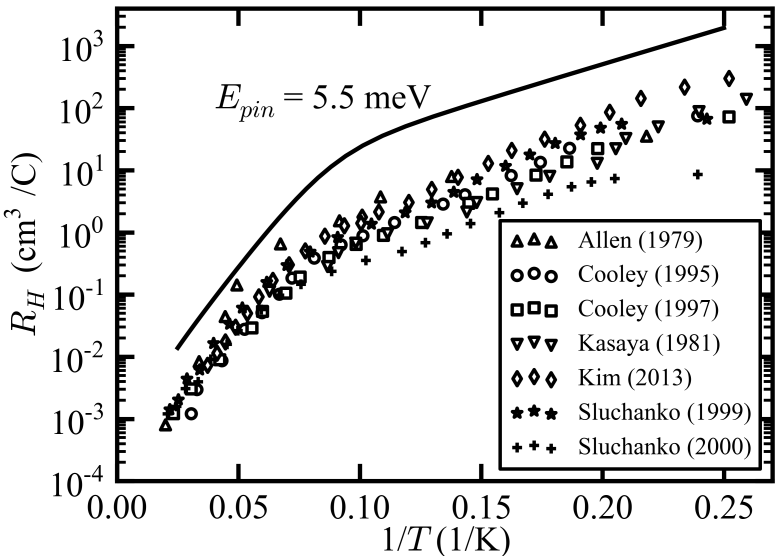

Figure 3.6: Comparison of one value of E_{pin} to a collection of Hall data. [9, 10, 161, 162, 16, 152, 115]

10-15 K and correctly describes the shape of the data, although the magnitude of our result does not agree with the data. This disagreement was expected based on the simplifications made to the dispersion. Previously, we estimated that these simplifications yielded errors of not more than a few meV in the dispersion, but this becomes very important for the Hall coefficient calculation. We can estimate the size of the expected discrepancy in the calculated Hall coefficient by using a Boltzmann factor, e^{Γ/k_BT}, where Γ is the approximate width of the features that were neglected. For Γ in the range of 1 to 3 meV in a temperature range of 10 to 20 K, the model is expected to be off at least by a factor of 2 and at most by a factor of 32. Our result was consistently a factor of about 5-6 greater than the data, and this is within the expected range of the discrepancy. Based on this estimate, agreement would likely be improved by including more features of the dispersion and DOS. However, this type of refinement would require many more parameters to be introduced.

3.5.2 Thermopower

We also compare the model to thermopower data, because like the Hall coefficient, it does not require any further parameters. In the relaxation time approximation, thermopower for

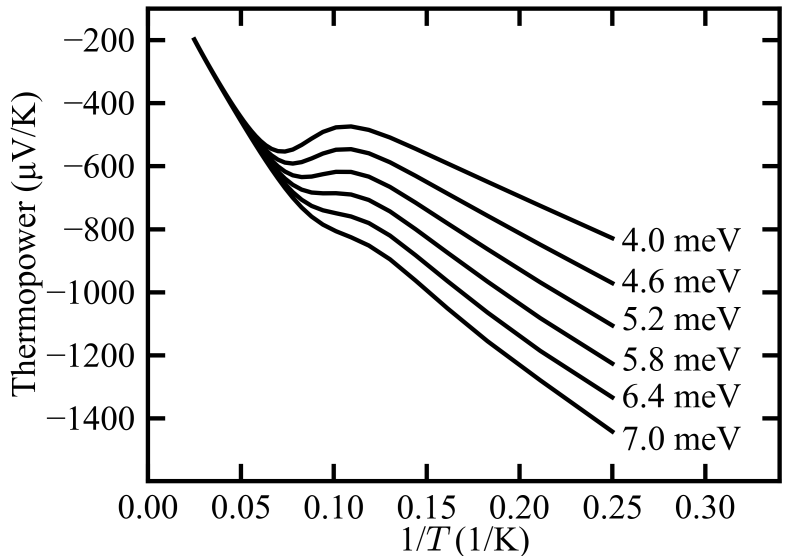

Figure 3.7: Thermopower versus temperature for various values of E_{pin}. A feature can be seen around 10 K, as in the Hall plot.

electrons in a semiconductor is given by [160]

$$S_C = -\frac{k_B}{e}\left[\left(\alpha + \frac{5}{2}\right) - \frac{E_C - E_F}{k_B T}\right] \tag{3.30}$$

where the subscript denotes the conduction band, and α is a constant between 0 and 2 that describes how energy is related to scattering time ($\tau \propto E^{\alpha}$). A similar expression can be obtained for holes in the valence band; it is important to note that the sign is positive for holes in a standard semiconductor. For a material containing both electrons and holes, these can be combined according to

$$S_{tot} = \frac{S_C \sigma_C + S_V \sigma_V}{\sigma_C + \sigma_V}. \tag{3.31}$$

In the limit of an intrinsic semiconductor, where $n = p$, the intrinsic carrier density in Eq. 3.11 and the usual conductivity in Eq. 3.23 can be used to simplify this. Assuming a quadratic dispersion for both the valence and conduction bands, we obtain

$$S = \frac{k_B}{e}\left[\frac{b-1}{b+1}\,\frac{E_{gap}}{2k_B T} + \frac{3}{4}\,\ln\frac{m_n}{m_p}\right] \tag{3.32}$$

where $b = \mu_n/\mu_p$, and the subscripts refer to electrons (n) and holes (p). [160, 152]

Again, the picture is slightly different in SmB_6. The factor of 1/2 must be accounted for once again, but based on the form of Eq. 3.31, it is clear that this factor cancels out for thermopower. Also, the curvature of the valence band means that the holes contribute with the same sign as the electrons. Using the conductivity derived in Eq. 3.27 and the analogous result for the valence band in Eq. 3.31, we can find the total thermopower in the model. Defining $\epsilon_c(z) = E_C(z) - E_F$ and $\epsilon_v(z) = E_F - E_V(z)$, we obtain

$$S(z) = -\frac{k_B}{e}\frac{1}{k_B T}\frac{\epsilon_c(z)e^{-\epsilon_c(z)/k_B T} + \epsilon_v(z)e^{-\epsilon_v(z)/k_B T}}{e^{-\epsilon_c(z)/k_B T} + e^{-\epsilon_v(z)/k_B T}} \tag{3.33}$$

where z again refers to the location in the bulk in the model. To get the total thermopower, we must integrate this expression, but since thermopower is dependent on conductivity and conductivity is dependent on z, it must be integrated using a form similar to that of Eq. 3.31. Thus, the effective thermopower across the bulk is

$$S_{eff} = \frac{\int_{-t/2}^{t/2} S(z)\sigma(z)dz}{\int_{-t/2}^{t/2} \sigma(z)dz} \tag{3.34}$$

where t is the thickness of the sample (here $t = 200\,\mu$m) and $\sigma(z) = n(z)e\mu$, where $n(z)$ is given by the integrand of Eq. 3.29.

S_{eff} was calculated as a function of temperature for various values of the pinning, shown in Fig. 3.7. Again, a feature around about 10 K is evident, although it is broader than the feature seen for the Hall effect. The bulk behavior in Fig. 3.7 is the same for all values of E_{pin}, but the surface behavior and prominence of the feature varies.

Fig. 3.8 shows a collection of thermopower data with a fit from the model. The data are consistent at high temperatures, and in this regime, there is also excellent agreement between the data and the model. As with the Hall coefficient, this agreement is expected as bulk effects dominate in this regime. At low temperatures, the data are more diverse. We note that the crossover does not occur at the same temperature in each data set shown, but we do not propose a mechanism for this. One possibility is that the transport geometries or dimensions (specifically thickness) of the three samples were different, leading to different effects of band bending in each sample. In the bulk-dominated regime, there is good agreement between

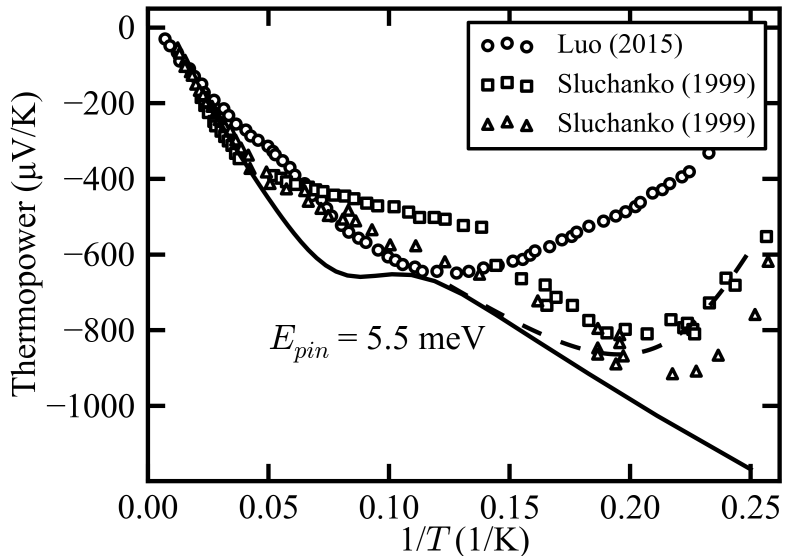

Figure 3.8: Comparison of calculation for one value of E_{pin} (solid line) to a collection of thermopower data. [131, 152] The effects of the TI surface state crossover are also shown (dashed line).

the data and the model. Below 4 K, a deviation between the model and the data can be observed. We attribute this deviation to the manifestation of the conductive surface state near 4 K, which can be added to the calculation.

To estimate the contribution of the surface state, we will again use Eq. 3.31,

$$S_{tot} = \frac{S_b \sigma_b t + S_s \sigma_s}{\sigma_b t + \sigma_s}, \tag{3.35}$$

where the subscripts b and s refer to bulk and surface contributions, respectively, and the thickness t is included so that the units match. From the theoretical treatment of TI surface states, [163] we expect that their contribution is much smaller than the bulk contribution. Therefore, only the first term will have a significant contribution to the thermopower. Near the bulk-to-surface transport crossover of $T_c = 4$ K, we also expect that the bulk and surface will contribute similarly to transport, i.e. $\sigma_b t \approx \sigma_s$. Each of these can be approximated using the form $\sigma_0 e^{E_a/k_B T}$, where E_a is the activation energy (the energy relevant to transport). For σ_s we use $T_c = 4$ K in this expression, and for $\sigma_b t$ we allow T to vary. We also assume that near T_c, σ_0 is about the same for both surface and bulk contributions. Then the thermopower

near 4 K, with $E_a = 3.47$ meV, [15] is approximately

$$S_{tot} \approx \frac{e^{E_a/k_BT}}{e^{E_a/k_BT} + e^{E_a/k_BT_c}} S_b. \tag{3.36}$$

This expression is shown in Fig. 3.8 with a dashed line, and the result provides a better estimate of the data near 4 K than the fit from the calculation.

Our model, with the addition of the estimation of surface effects, captures the low-temperature features of the thermopower well. We note that there is not much thermopower data available in the literature, which makes it difficult to understand trends in the data as done for the Hall coefficient. Our model agrees quite well with the data from Sluchanko *et al.* [152], but not as well with the other data. Again, a discrepancy between the data and the model is present, and again we attribute this to neglecting the small features of the dispersion. Improved agreement could likely be attained by adding more details of the dispersion to the model.

3.6 Conclusion

We have presented a model to understand the difference between the spectroscopy and transport gaps in SmB_6 without relying on in-gap bulk states. Transport measures an activation energy of 3-4 meV, expected to correspond to a total gap size of 6-8 meV, while spectroscopic methods measure a gap of 16-20 meV. This discrepancy between the two results has often been explained by introducing a localized bulk state in the gap, perhaps due to impurities, although other explanations such as the presence of an indirect gap have also been used. The effective mass approximation has been used to understand such an in-gap impurity state, because this method has been successful at describing impurity states in many gapped materials. However, we showed that the effective mass approximation fails when it is applied to SmB_6, suggesting that the in-gap impurity state picture is not justified.

Instead, we suggested a new way of understanding the SmB_6 gap using self-consistent band-bending calculations. We simplified the well-known dispersion and corresponding density of states to capture the main characteristics of SmB_6 and modeled SmB_6 as an intrinsic

semiconductor. We considered the possibility of band bending, which is expected to arise from the presence of excess surface charges. A self-consistent solution for the potential was found by numerically solving Poisson's equation with this charge density across the bulk of a test sample, with the boundary conditions simulating the strength of the bending effects at the surface and enforcing symmetry across the bulk.

The self-consistent solution was found for temperatures from 4-40 K, and from this result the band structure was calculated. In addition, the band structure result was connected to measurable transport parameters using semiclassical transport theory modified for SmB_6. Specifically, we concentrated on Hall coefficient, resistivity, and thermopower, as these do not require the addition of adjustable parameters to our model. The results of these calculations demonstrated a crossover to bulk transport dominated by bulk effects (in analogy with a standard gapped material) at high temperatures, to bulk transport dominated by surface effects at low temperature. The calculated crossover temperature was 10-15 K, which accounts for a feature that has been observed in transport data near this temperature. The transport parameters were compared to data, and although there was qualitative agreement between the data and the calculated curves, their magnitudes did not agree. We attributed the disagreement to neglecting some of the small features of the actual dispersion in the model, and found that a few meV of error in the dispersion could explain the disagreement.

We also related the feature seen in transport data to the accumulation length for a semiconductor. At high temperatures, the accumulation length was much smaller than the sample size, and at low temperatures, the accumulation length was much larger than the sample size. We estimated that the crossover would occur when bulk effects in terms of sample thickness and intrinsic carrier density become comparable to surface effects in terms of accumulation length and surface charges. Because of this relationship between accumulation length and sample size, our model suggests that the crossover would occur at different temperatures for different sample thicknesses.

The divergence of the accumulation length in SmB_6 at low temperatures suggests that the gap is clean, similar to the gap in a superconductor. This, combined with the success of our model at describing a variety of data without introducing bulk states in the gap, agrees well with the observation that there is no residual bulk conduction in SmB_6 below the

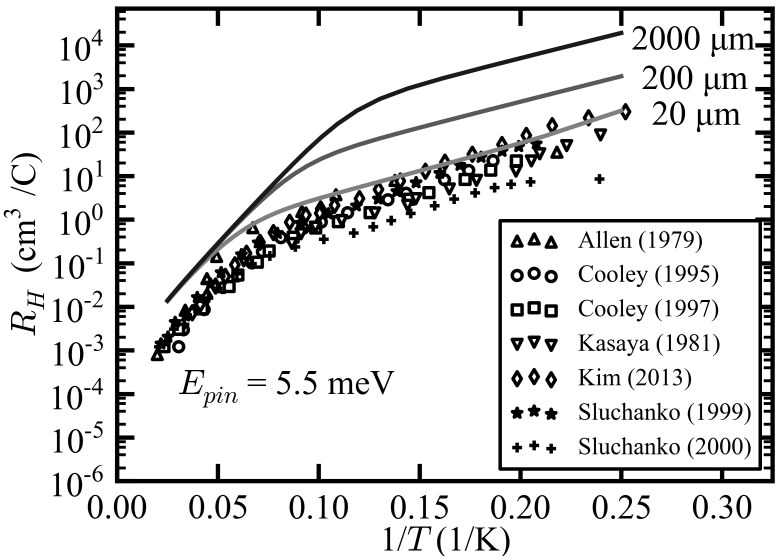

Figure 3.9: Predicted thickness dependence of crossover for $E_{pin} = 5.5$ meV.

TI crossover temperature of about 4 K. Together, these observations imply that SmB_6 is a true TI; it does not exhibit bulk conduction below the TI crossover temperature as all other known TIs do. This would be exciting for research in technological applications that require a clean gap and no bulk conduction. We also predict that our model could be extended to other materials that have a dispersion similar to that of SmB_6, including alloys of SmB_6.

3.6.1 Experimental verification

There are a few straightforward ways to test our model. Based on the results for accumulation length compared to sample size, the simplest method would be to determine the location of the 10-15 K feature for samples of different thicknesses. For a thin sample, the crossover temperature would be higher than the 10-15 K temperature calculated in our simulation, and for a thicker sample, the crossover temperature would be lower than 10-15 K. This dependence on thickness is shown in Fig. 3.9 for samples from 20-2000 μm in thickness, and the change in the crossover temperature is large enough to be experimentally measurable. We initially performed transport measurements on two samples with thicknesses of 65 μm and 960 μm, shown in Fig. 3.10, but no difference in the location of the feature was observed. Instead, we noticed significant differences between the transport results of the two samples.

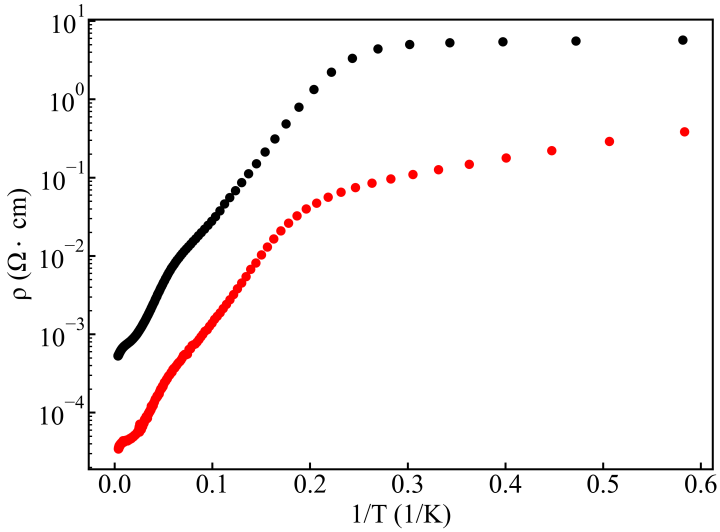

Figure 3.10: Resistivity measurements comparing a 65 μm thick sample and a 960 μm thick sample.

The thin sample was grown by the Al flux method, while the thick sample was grown by the floating zone method, prompting further studies of how growth technique affects the results. The results from these two measurements and continued investigations of the bulk Hall characteristics of SmB_6 will be discussed in Chapter 5.

In addition, we used the focused ion beam process described in Chapter 2 to prepare micro Hall bars of about 2 μm thickness out of the two samples initially used to test the thickness hypothesis. The only surviving micro Hall bar was from the flux-grown sample, and the transport results from this micro sample are shown in Fig. 3.11. No difference could be observed between the location of the 10-15 K feature in this sample compared to the original sample.

Another way to test the thickness dependence of the model is through ionic liquid gating. This technique uses a liquid composed of heavy ions in place of the traditional metallic gate and is ideal for samples with large surface area. In SmB_6, this technique is especially useful as it allows all surfaces to be gated simultaneously. As with traditional gating, ionic liquid gating can be used to change the carrier density of the surface conduction channel, which would change the location of the 10-15 K feature. Applying a positive voltage is expected to raise the crossover temperature while negative voltage is expected to lower the crossover

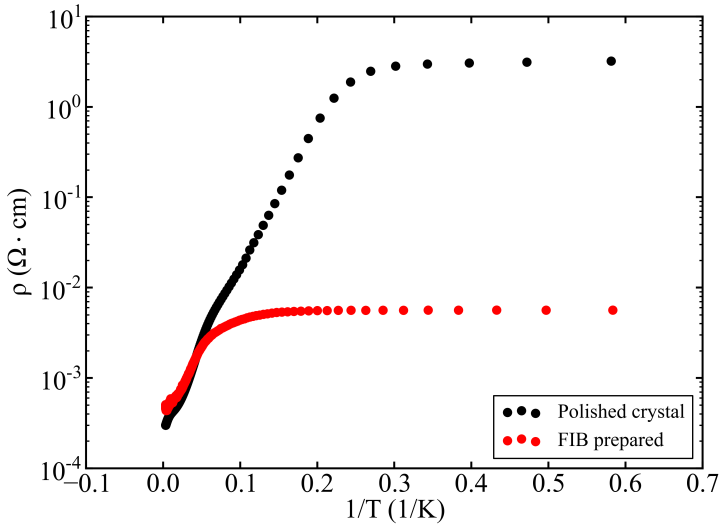

Figure 3.11: Resistance measurements comparing a 65 μm thick Hall bar (polished crystal, black) and a 2 μm thick Hall bar carved using a focused ion beam (FIB prepared, red).

temperature. We also performed ionic gating measurements on SmB_6 but again observed no difference in the location of the 10-15 K feature. Ionic liquid gating will be explored in further detail in Chapter 5 in the context of studying the SmB_6 surface.

3.6.2 Subsequent studies on the gap of SmB_6

After this work was published, another study of the possibility of hydrogenic impurities in SmB_6 was performed by B. Skinner. [105] In this study, the idea that the semiconductor effective mass approximation should not be used in SmB_6 is confirmed. One issue with using the semiconductor formulation is that SmB_6 does not have the same parabolic dispersion as semiconductors. In the new study, a re-derivation of the effective mass approximation for the "Mexican hat" dispersion of SmB_6 is presented. The calculation yields new equations for the effective Bohr radius and binding energy based on the Bohr radius in hydrogen and a momentum scale derived fromthe lattice parameter. Additionally, the Mott criterion, or the critical doping leading to an insulator-metal transition is found to be modified in SmB_6 compared to a semiconductor. As a result, SmB_6 could contain a much larger amount of impurities and still remain a bulk insulator than previously thought.

These new results suggest that SmB_6 likely hosts impurity states in the gap. In dc

transport, the in-gap impurity states are predicted to have an activated behavior with an activation energy much less than the activation energy related to the hybridization gap. We believe that this model captures the electronic structure of SmB_6 with much more detail and nuance than the band bending model presented in this chapter. In addition, the experimental tests of band bending failed to verify it. Thus, the band bending model should not be used to describe SmB_6; instead, the Skinner model provides a much more complete picture of the gap and the impurity states in SmB_6.

Chapter 4

Comparison of Aluminum Flux and Floating Zone Grown SmB_6 Using Hall Bar Geometry

4.1 Introduction

In the previous chapter, a simple method for experimentally testing the band bending model was introduced: measure the 10-15 K feature in Hall effect on samples of different thicknesses. One important consideration before undertaking such a measurement, however, is the method by which the sample was grown. As introduced in Chapter 2, SmB_6 samples are primarily grown by the aluminum flux or floating zone methods. Al flux grown samples often contain inclusions of aluminum, so these samples must be thinned before using them to ensure no aluminum remains. Thus, it can be difficult to compare transport as a function of thickness when using only Al flux grown samples. However, floating zone samples do not contain inclusions, and since they are cut from a large boule, they can be quite thick. In this way, data on thicker samples can be obtained.

As discussed in the previous chapter, a thinned Al flux grown sample and a thick floating zone sample were tested to try to verify the band bending model. The 10-15 K feature was not significantly different between the two samples, but other differences at both low and

high temperatures were observed. It is possible that the two specific samples chosen for this initial measurement were pathological, but after obtaining further transport data on samples grown by the two techniques, it seems that a difference really is present. This is surprising, as the growth method of the sample is not expected to affect transport results. In this chapter and the next, transport results on a number of Al flux and floating zone grown samples are presented. In this chapter, results on Hall bar geometry are discusssed, with a focus on the bulk channel that dominates conduction from about 5-400 K. Preliminary results presented in this chapter were published in the Journal of Superconductivity and Novel Magnetism, vol. 33, page 265 in 2019. [164]

Besides our initial transport measurements performed in relation to band bending, a clear variation in experimental reports can also be seen when comparing Al flux and floating zone grown samples. For example, ARPES reports that claim the existence of a topologically protected state [19, 20, 21] were performed primarily on Al flux grown samples, while the reports that claim a trivial conductive state [24] were performed on floating zone grown samples. Additionally, the dHvA results with signatures of a 2D Fermi surface [85, 86] were performed on Al flux grown samples, but the results with signatures of a 3D Fermi surface [26, 27] were performed on floating zone grown samples. In thermal transport, one study finds evidence for charge-neutral quasiparticles in floating zone samples [27] while another finds no evidence for them in flux grown samples. [88] A further study comparing flux and floating zone grown samples found differences in behavior between the two, but no evidence for charge-neutral quasiparticles in either type. [89] Overall, this suggests that sample growth method in SmB_6 can unexpectedly have an impact on the physical properties of the sample. However, it is unclear whether the origin of the discrepancies is extrinsic or intrinsic in SmB_6.

One possibility is that the amount of disorder differs between Al flux and floating zone grown samples, perhaps from effects arising during growth. Generally, the level of disorder can be probed in transport via the mobility, which requires measuring the resistance and Hall coefficient. However, the Hall coefficient is known to change sign around 65 K, from negative at lower temperatures to positive at higher temperatures. From ARPES results [22] the charge carrier in SmB_6 is known to be electrons, so the region where Hall coefficient is positive makes the mobility very difficult to calculate. The sign-change behavior has been

well-studied in heavy fermion systems and is associated with skew scattering, [165, 166, 167] an asymmetrical scattering of charge carriers due to strong correlations. It is enhanced in the presence of magnetic field, leading to the change of sign in the Hall coefficient. [9, 29, 123, 164] However, the general heavy fermion case is a bit different than what is seen in SmB_6. Based on the charge carrier type, the positive Hall coefficient due to skew scattering is seen from the transition temperature and below, while the negative Hall coefficient is seen above the transition temperature. The reasons for this, and the possibility of seeing a negative Hall coefficient in SmB_6 above room temperature, were not previously explored.

In this chapter, we measure resistance and Hall coefficient on both Al flux and floating zone grown samples to compare bulk characteristics between the two sample techniques, and to better understand the role of skew scattering in measurements of the Hall coefficient. We find that there is some sample-to-sample variation above about 40 K but that it cannot be clearly divided along the lines of sample growth technique; that is, both flux and floating zone samples demonstrate skew scattering and the sign change at roughly the same temperatures. In studying skew scattering, we extend our measurements to 400 K and find that a second sign change is present at about 310 K. We discuss a qualitative model of skew scattering to understand the two sign changes and how SmB_6 differs from other heavy fermion systems.

4.2 Results

We measured the resistance and Hall coefficient of four floating zone and four flux grown samples from 2-400 K using Hall bar geometry. Details of the sample origin and characteristics are shown in Table 4.1. The flux grown samples were thinned to ensure that no Al inclusions remain. All samples were prepared identically by polishing on the four sides making up the active region of the Hall bar with progressively smaller grit sizes down to 0.3 μm. The Hall bar geometry was defined by painting photoresist in the desired pattern and metallizing with Ti/Au. Contacts were made with silver paste and gold wire. Measurements were performed in a 14 T Dynacool Quantum Design Physical Property Measurement System (PPMS) with an SR830 lock-in amplifier.

The resistances are shown in Fig. 4.1. Resistance rather than resistivity is shown here as

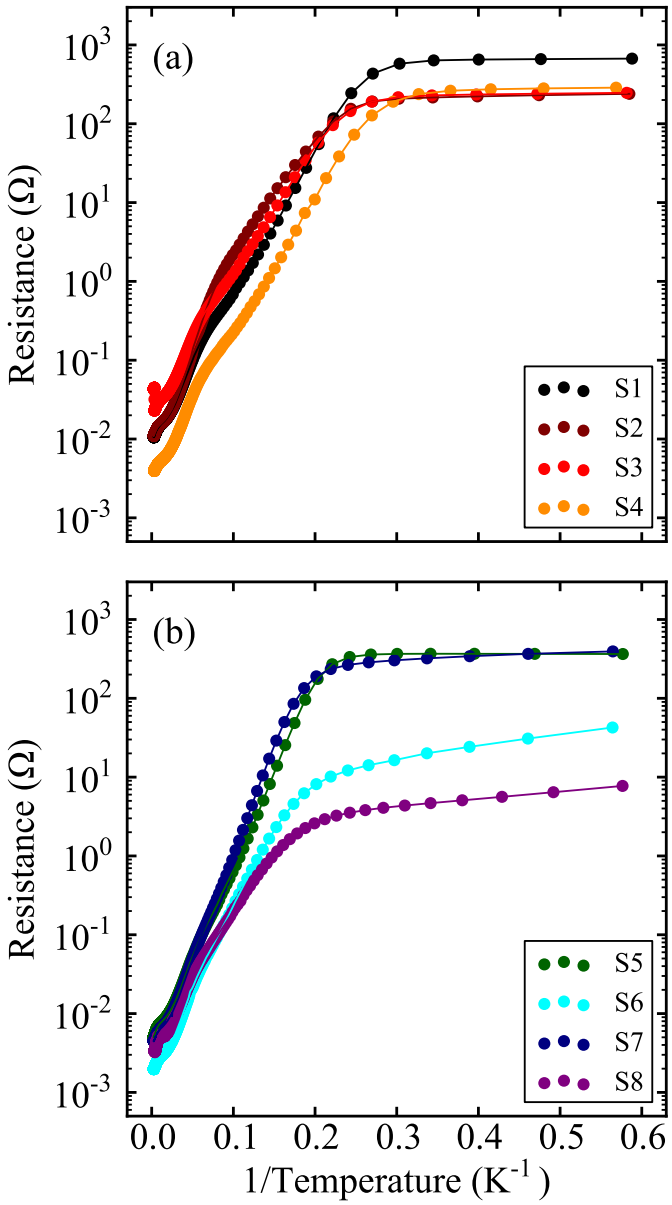

Figure 4.1: Resistance of (a) Al flux and (b) floating zone samples.

Sample	Technique	Source	Crystal plane	Details
S1	Flux	Irvine	(100)	Standard growth
S2	Flux	LANL	(100)	Standard growth
S3	Flux	GIST	(100)	Standard growth
S4	Flux	GIST	(100)	Standard growth
S5	FZ	Warwick	(111)	Standard growth [11]
S6	FZ	Warwick	(100)	Standard growth [11]
S7	FZ	JHU	(100)	Doubly-isotopic purification, Sm deficient
S8	FZ	JHU	(100)	Standard growth [107]

Table 4.1: Growth details of eight SmB_6 samples including growth technique, place of origin, and crystal plane. Abbreviations used: Floating zone (FZ), University of California Irvine (Irvine), Los Alamos National Laboratory (LANL), Gwangju Institute of Science and Technology (GIST), University of Warwick (Warwick), and Johns Hopkins University (JHU).

SmB_6 contains regions of two- and three-dimensional conduction. Thus, three-dimensional resistivity can be misleading at low temperatures. The resistances are within an order of magnitude of each other at high temperatures but show an almost three orders of magnitude range at low temperatures. In addition, the four samples with the highest resistances all show horizontal plateaus. The two samples with lowest resistance, S6, and S8, which are both floating zone grown, have finite slope below 5 K. This variation among the floating zone samples is in agreement with the literature. [113, 168, 107]

Hall coefficient data is shown in Fig. 4.2. The low-temperature behavior mirrors the resistance, in that S6 and S8 have a lower Hall coefficient and a non-horizontal plateau. The feature seen in all samples near 5 K is due to the crossover from bulk to surface conduction. At high temperatures, well above where surface effects are relevant, the Hall effect changes sign. In all samples, the sign change occurs near 65 K; above 65 K the Hall coefficient is positive but below 65 K the Hall coefficient is negative. These observations are in agreement with the literature. [9, 29] By measuring above room temperature (up to 400 K) we also observed a second sign change at about 305 K. Above 305 K, the Hall coefficient becomes negative again. All the samples showed this effect, although some samples had less clearly defined features. Two representative traces, from a flux grown sample (S3) and a floating zone grown sample (S8) are shown in the inset of Fig. 4.2. No difference in features was observed when comparing the flux grown and floating zone grown samples above 60 K.

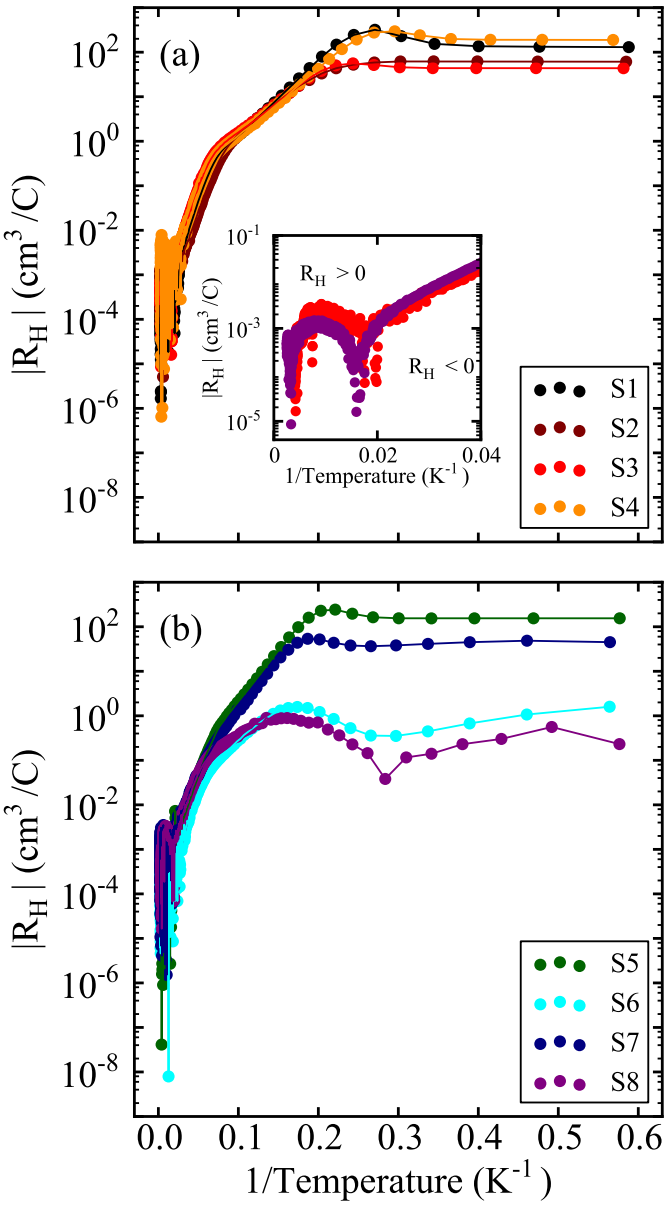

Figure 4.2: Hall coefficient of (a) Al flux grown and (b) floating zone grown samples. The inset shows a flux grown sample (red) and a floating zone sample (purple) overlaid at high temperatures.

4.3 Discussion

The dominant carrier in SmB_6 is known from the band curvature to be electrons, so the positive Hall coefficient from 65-305 K does not reflect the carrier type. This anomalous sign arises from skew scattering when f-d correlations are in strong resonance and is well-known in SmB_6. [166, 123] In general, skew scattering is common in heavy fermion systems where each site can be viewed as a resonant scattering center at high temperatures. [165] It occurs when the scattering from k to k' is asymmetric; this is enhanced under external magnetic field and is responsible for the anomalous sign in the Hall effect in SmB_6.

In SmB_6, the effect of skew scattering can be understood using the band structure of SmB_6 and the energy of the f and d electrons. In the band structure, shown in Fig. 4.3(a), the f level that participates in hybridization has a weak dispersion in k as well as some intrinsic broadening. [22] Since the actual contributions of these are difficult to separate experimentally due to thermal effects, we define the total f-level width to be ΔE_f. The d electrons in SmB_6 are the conduction electrons, so we expect that only the d electrons within k_BT of the Fermi energy participate in transport. Also, the Fermi energy in SmB_6 is resonant with the f bands, so when k_BT is comparable to the width of the f band, the f and d electrons are resonant with each other, resulting in strong skew scattering.

At high temperatures, the thermal energy of the d electrons is large ($k_BT \gg \Delta E_f$), meaning that not many d and f electrons are in resonance. This is indicated by the arrow for 400 K in Fig. 4.3(b). In this regime, the effect of skew scattering is small, so conventional scattering mechanisms should dominate. This agrees with the negative sign of the Hall coefficient observed in our data above about 305 K. As the temperature decreases, more d electrons become resonant with the f level ($k_BT \sim \Delta E_f$), and skew scattering becomes very strong. This is indicated by the arrow for 200 K in Fig. 4.3(b). In this regime, we observe the positive sign of the Hall coefficient because of the skew scattering effect. Further lowering the temperature leads to the opening of the Kondo gap. As the gap opens, the skew scattering effect is destroyed, because d and f electrons are hybridized and can no longer be in resonance, as shown in Fig. 4.3(c). In the data, we observe this as the correct, negative sign of the Hall coefficient, consistent with the band curvature, down to lowest temperatures.

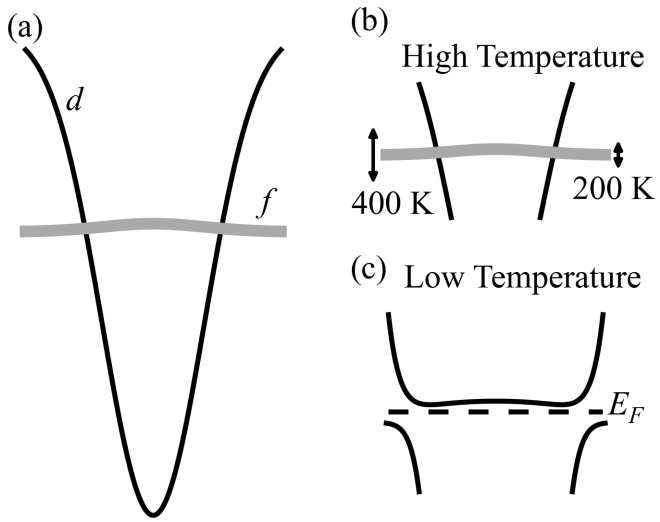

Figure 4.3: (a) Band diagram schematic of SmB_6 at room temperature. (b) Zoom of (a) with arrows indicating k_BT at 200 K and at 400 K. (c) Band diagram of SmB_6 at low temperatures were the gap is open. The three diagrams are not drawn to scale, and only the f band that participates in hybridization is shown.

More quantitatively, skew scattering in heavy fermion materials is related to the Hall coefficient, and that relationship depends on the temperature at which the skew scattering is strongest. In our data, this point occurs at about 100 K, although there is some sample-to-sample variation. Below about 100 K, the Hall coefficient is related to the magnetic susceptibility and the total resistivity: $R_H \propto \chi\rho^2$. [167] Above about 100 K, the relationship is modified to $R_H \propto \chi\rho$. [165] This skew scattering term can be added to the conventional terms. [165]

In our data, the sign change and skew scattering are not consistent across samples. Of the samples we measured, the two shown in the inset of Fig. 4.2 demonstrate the clearest sign changes. The differences between the high temperature effects in these samples suggests that the strength of skew scattering varies from sample to sample. One reason for this could be different levels of unintentional doping in each sample, leading to a greater contribution by impurity scattering that slightly masks skew scattering.

The sign of the Hall coefficient also affects transport analysis. In conventional materials, the carrier density and mobility can be extracted from the resistivity and Hall coefficient by

$n = 1/(eR_H)$ and $\mu = 1/(ne\rho)$, respectively. This method is still valid in SmB_6 below 50 K, where activated behavior is observed. However, in the presence of skew scattering at higher temperatures, the carrier density and mobility are inaccurate in both sign and magnitude. Using the standard analysis would suggest that the sign of the charge carriers changes with temperature, and it yields negative mobility, both of which are clearly incorrect.

To obtain a better picture of the true carrier density in SmB_6, we used ARPES data to estimate the high temperature carrier density. ARPES reports of the size of the d pockets in the bulk Brillouin zone allows us to calculate the maximum number of carriers allowed, 9 $\times$ 10^{21} cm^{-3}. [22, 145, 164] The carrier density extracted from transport would be expected to approach this maximum as temperature is increased. We then smoothly connected this to the carrier density extracted by standard methods below 50 K to obtain an estimate of the electron-like carrier density that might be measured if skew scattering were not present.

The estimated carrier density can then be used to calculate the mobility. The mobilities extracted by this method for the samples are shown in Fig. 4.4. A new feature appears in mobility when using this method: a minimum is present near 100 K, but the exact temperature at which the minimum occurs varies from sample to sample. Table 4.2 lists the mobility minima of the samples. For S1, S5, S7, and S8, the minimum is close to 100 K. S3 may have a minimum at a slightly higher temperature as this sample is much thinner than the others. On the other hand, S6 is much thicker than the others and showed different behavior from the other five samples at all temperatures. In S6, to investigate the possibility that there was an inclusion of another phase that affected the results, we polished the sample after measuring it using the same methods we use to remove Al inclusions in flux grown samples. We did not observe any inclusions in S6.

The mobility minimum indicates where scattering is strongest. Since skew scattering is the dominant scattering mechanism for SmB_6 at this temperature, the minimum indicates where skew scattering is strongest, and 100 K corresponds to the approximate temperature of the peak in the positive regime of the Hall coefficient (Fig. 4.2) as well as the temperature at which the hybridization gap begins to open as temperature decreases. [112, 22] As the temperature increases, conventional scattering mechanisms like impurity and phonon scattering become dominant.

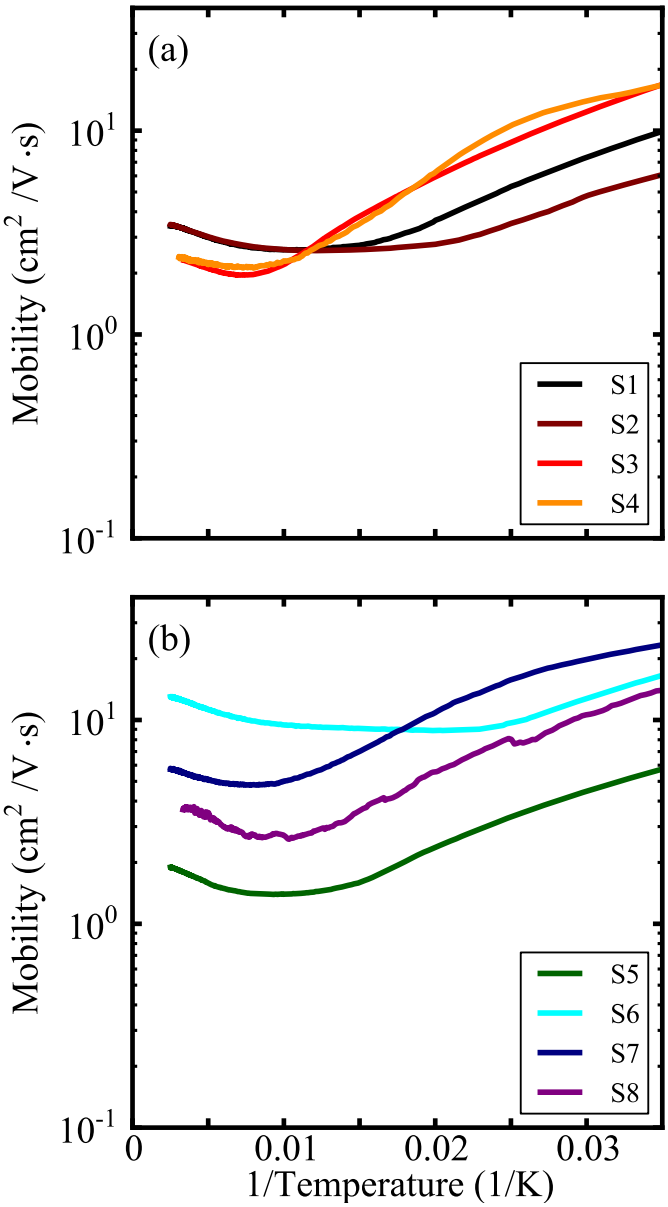

Figure 4.4: Mobilities of (a) flux and (b) floating zone samples calculated using an estimate of the Hall coefficient with the correct sign.

Sample	T_{min} (K)	μ_{min} (cm^2/V·s)	τ (fs)	ℓ (Å)
S1	97	2.6	1.3	7.8
S2	80	2.6	0.8	6.0
S3	142	2.0	0.98	6.0
S4	152	2.1	1.0	6.3
S5	107	1.4	0.68	4.2
S6	50	8.6	4.2	26
S7	107	4.8	2.3	14
S8	97	2.3	1.1	6.9

Table 4.2: Mobility minima of eight SmB_6 samples with the corresponding temperatures, scattering times, and mean free paths.

Table 4.2 also lists the scattering times and mean free paths for each of the samples at the mobility minimum. In calculating the scattering time ($\tau = \mu m^*/e$) and mean free path ($\ell = v_F\tau$), we used an effective mass of $0.86m_e$ and a Fermi velocity of 6.1×10^5 m/s, both obtained from ARPES data. [22] Our calculation of τ and ℓ are well within the metallic regime of SmB_6. At the minimum, all samples also satisfy $k_F\ell > 1$, confirming that hybridization begins near this point.

4.4 Conclusion

In this chapter, we presented transport measurements on both Al flux and floating zone grown SmB_6 from 2-400 K. Below 5 K, our resistivity results on Hall bar geometry show almost three orders of magnitude spread in their low-temperature saturation values, with flux samples showing some of the highest magnitudes and floating zone samples having more variation. A more detailed look at features below 5 K will be presented in the next chapter. Here, we concentrated on the bulk characteristics above 40 K, especially the well-known sign change feature in the Hall coefficient. The Hall coefficient is negative below 65 K, positive from 65 K to 310 K, and negative again above 310 K. Although the sign change at 65 K was reported in previous literature, we observed a second sign change at 305 K. The positive Hall coefficient is successfully described using skew scattering, an anomalous asymmetrical scattering mechanism found in heavy fermion systems. The presence of the sign change in transport is misleading, as both the magnitude and sign of the charge carriers extracted

for the bulk will be incorrect. Calculation of transport parameters was also revised to account for the effects of skew scattering by combining our transport data with results from ARPES. This yields a minimum in mobility near 100 K for most samples. This minimum indicates where scattering is the strongest and a combination of skew, impurity, and phonon scattering is present. The Hall sign change is observed in both flux grown and floating zone grown samples, demonstrating that the sample growth method alone does not affect this property of SmB_6. However, other factors, including purity of the starting materials and quality of the growth conditions in both growth methods, may have an effect on the strong correlations and lead to noise that "smears" the high-temperature features. Overall, this chapter strengthens the overall understanding of high-temperature bulk transport, which is necessary to gain a complete picture of SmB_6.

Chapter 5

Bulk Transport Paths Below 4 K Using Inverted Resistance

5.1 Introduction

In the previous chapter, bulk characteristics of SmB_6 were explored from 5-400 K using Hall bar geometry. Below about 5 K, the Hall bar measurements reveal that while flux-grown samples have fairly consistent resistance plateaus, floating zone samples show more variation. However, in this temperature range, surface and bulk conduction coexist (with surface conduction dominating), so traditional four-point geometry like Hall or van der Pauw can no longer provide information about whether the features we observed arise from the surface or the bulk. Instead, we employ the inverted resistance method introduced in Chapter 2 to investigate bulk properties of SmB_6 below 5 K.

In this chapter, inverted resistance measurements on a Corbino disk geometry are presented. This work is currently under review at Physical Review Materials. Previous data for Al flux grown samples are included, and new data on floating zone samples are shown to compare results on samples grown by different techniques. The pure Al flux grown sample showed insulating behavior down to 2 K, [110] while Al flux grown samples grown intentionally with off-stoichiometry show a small amount of residual bulk conduction below. On the other hand, the floating zone samples all demonstrate bulk conduction at lowest tem-

peratures, but with significant sample-to-sample variation. The possible origins of this new bulk channel are also discussed in the context of recent impurity models as well as one-dimensional defects, or dislocations. To expand experimental understanding of the role of disorder, we also perform chemical etching to verify the presence of dislocations in both Al flux and floating zone grown samples. The wide variation in the low-temperature results depending on the sample used suggests that discrepancies in experimental reports on SmB_6 may have an extrinsic rather than an intrinsic origin.

5.2 Summary of previous inverted resistance results

The previous results for inverted resistance on flux grown SmB_6 were published in Proceedings of the National Academy of Sciences, vol. 116, no. 26, p. 12638 in 2019. First, the inverted resistance method introduced in Chapter 2 will be reviewed. This method constrains the current to a closed loop, and voltage is measured outside of the loop. For materials with both surface and bulk conduction, the surface conduction is contained within the loop, so any signal measured outside of the loop must come from the bulk. [126] A Corbino disk geometry is optimal for performing inverted resistance measurements, and a schematic of the geometry used was previously shown in Fig. 2.2.

Inverted resistance measurements yield two curves, one from the standard measurement (Fig. 2.2(b)), and one from the inverted measurement (Fig. 2.2(c)). As introduced in Chapter 2, the standard resistance curve is proportional to the resistivity of the dominant conduction channel. In SmB_6, this means that the standard curve is proportional to bulk resistivity (ρ_b) above about 5 K but proportional to surface resistivity (ρ_s) below this temperature. The inverted curve is also proportional to the bulk resistivity above about 5 K, or where bulk conduction is dominant. On the other hand, the inverted curve depends on both the surface and bulk resistivities as $R_{\mathrm{Inv}} \propto \rho_s^2/\rho_b$. An example of standard and inverted resistance curves is shown in Fig. 5.1.

To calculate the bulk resistivity over the whole temperature range, $1/R_{\mathrm{Inv}}$ is calculated so that the result is proportional to the bulk resistivity. Flipping the curve in this way extends the activated bulk behavior seen in the standard curve above 5 K to temperatures

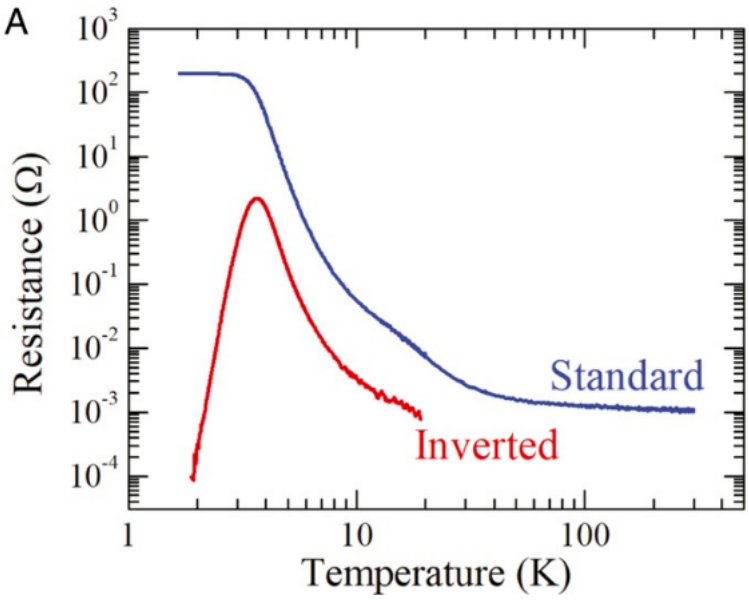

Figure 5.1: Example of standard and inverted curve of a stoichiometric Al flux grown sample.

below 5 K. The standard curve and the flipped inverted curve often do not match exactly however, and this is likely due to misalignment of the two Corbino disks or imperfections in the surface preparation (polishing) on the two faces that have Corbino disks.

This inverted method was used to measure bulk resistivity of four Al flux grown SmB_6 samples from 2-300 K. [110] Of the four samples presented, S1 was grown stoichiometrically, with a 1:6 Sm:B ratio. S2, S3, and S4 were grown with off-stoichiometry, which allowed the introduction of Sm vacancies; the actual concentration of vacancies is difficult to measure by x-ray diffraction and likely does not match the growth ratio. The growth ratios were 0.9:6 Sm:B for S2 (10% Sm deficiency), 0.75:6 Sm:B for S3 (25% Sm deficiency), and 0.6:6 Sm:B for S4 (40% Sm deficiency). All four samples were prepared identically by polishing with grit sizes down to 0.3 μm. The Corbino disks were defined using photolithography and metallized by e-beam evaporation of Ti/Au. Electrical connection was done using gold wires attached using either silver paste or wire bonding.

Results from these four samples are shown in Fig. 5.2. S1 (black) shows insulating behavior down to 2 K with a resistance rise of about 10 orders of magnitude. The three samples grown with off-stoichiometry, however, show a saturation of resistance below 2.5 K. Thus, they contain a small bulk conduction channel that is usually buried beneath the

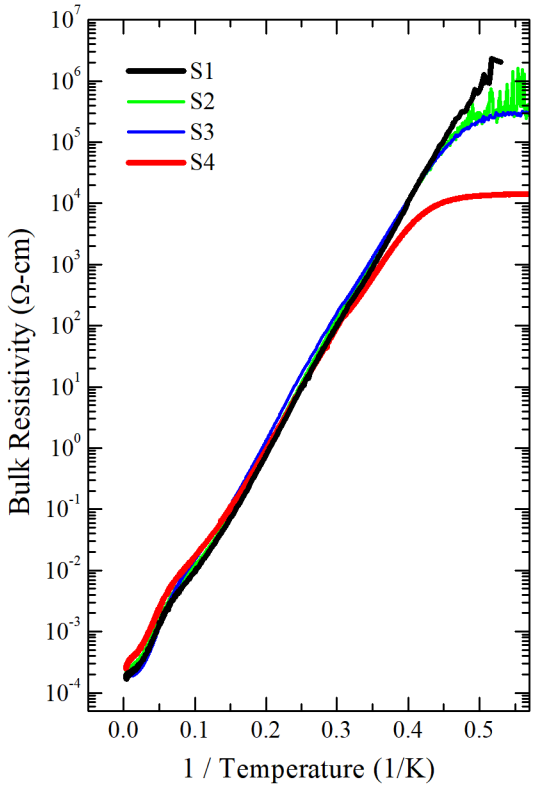

Figure 5.2: Inverted resistance measurement of four Al flux grown SmB_6 samples.

dominant surface conduction.

The resistivity values of this newly discovered bulk channel at low temperatures are extremely high. In fact, such resistivity saturation after a high magnitude increase is only seen in ultra clean semiconductors. [169, 170] This would correspond to a tiny conduction channel; nevertheless, understanding the origin of this low-temperature bulk conduction is important for understanding the unique role of disorder in SmB_6. Since S2, S3, and S4 all contain Sm vacancies, one possibility is that this third channel could arise from impurity conduction. However, the role of vacancies is under debate within the SmB_6 community. Instead, another possibile source of the third bulk channel could be conduction through one-dimensional defects, or dislocations, that are topologically protected. [110]

Dislocations have been studied extensively in semiconductor thin films such as GaN, where they are a significant source of scattering in electronic devices and provide recombination sites in optoelectronic devices. [137] In thin films, dislocations form during growth, especially at the interface between a substrate and a film with different lattice constants.

This lattice mismatch between the two materials strains the layer, leading to the formation of dislocations. [138] The density of dislocations present in the film is related to the difference in lattice constants between the substrate and the film, with lower dislocation density corresponding to more closely matched lattice constants. Dislocations are also present in crystals. They can form from internal stresses in the growth, especially stresses due to thermal fluctuations, local impurities in the growth, or even vibrations in the environment. [138] Impurities in the growth can provide nucleation sites where dislocations start to form, and high temperatures used in the growth can compound the effect of internal stresses as well. [139] Additionally, dislocations can extend from a seed crystal containing dislocations to new growth based on that seed. [139] However, not much is known about dislocations in topological materials. Previously, dislocations in Bi-based topological thin films have been shown to create unwanted bulk current paths. [171, 172] Dislocations in SmB_6 would be especially interesting to study in light of the previous report of a truly insulating bulk in the dc limit.

The level of disorder can generally be measured in transport via the mobility. At low temperatures, measurements of mobility in SmB_6 are not straightforward. Experimental reports - ARPES, dHvA oscillations, and transport - disagree on the order of magnitude of the mobility, which ranges from about 10 $cm^2/V{\cdot}s$ in transport [131] to about 1000 $cm^2/V{\cdot}s$ in quantum oscillations; [85] surface preparation can even affect the extracted mobility. [173] A recent study also shows that the two proposed topological surface channels would have very different mobilities, [173] and accounting for a disorder-based channel could be an additional challenge.

Data presented in the previous chapter as well as detailed literature results have also shown that the resistivity saturation in standard measurements at low temperature is non-universal. [107] Al flux grown samples generally yield resistivity with temperature-independent plateaus. [10, 152, 131] Floating zone samples are generally less consistent and can behave similarly to flux-grown samples, show temperature-dependent behavior, or even a step-like behavior. [174, 175, 107] An open question is whether these differences in behavior are due to different surface characteristics or bulk characteristics. If the differences are due to surface characteristics, the low-temperature bulk behavior should be similar between both types of

Sample	Growth details	Starting powder origin
Warwick 1	Standard growth [11]	Alfa Aesar
Warwick 2	Standard growth [11]	American Elements
JHU 1	Standard growth [107]	Testbourne Ltd.
JHU 2	Doubly-isotope enriched, Sm deficient	Alfa Aesar

Table 5.1: Details of the four floating zone samples measured. Sample names indicate growths by collaborators at University of Warwick (Warwick) and Johns Hopkins University (JHU).

samples. But, if bulk characteristics differ at low temperatures, this would be reflected in inverted resistance measurements.

5.3 Results on floating zone samples

Four floating zone samples were prepared for the inverted resistance measurement. Details of the samples' origins and growth methods can be found in Table 5.1. All samples were polished with grits down to 0.3 μm. The Corbino disks were patterned by photolithography. Ti/Au was deposited on the samples using e-beam evaporation and later a lift-off process with acetone was used to define the pattern and electrodes. We used gold wires to make electrical connection from the electronics to the sample, and attached them using either silver paste or wire bonding.

Fig. 5.3 shows the resistance vs. temperature of all four samples. The blue curves are the standard resistance measurements and the red curves are the inverted resistance measurements. In the standard measurements (blue curves), all four samples show a change in slope around 4 K that would conventionally be regarded as a surface plateau. Fig. 5.3 (a) and (d) show little to no temperature dependence in the standard measurement below about 4 K, especially compared to Fig. 5.3 (b) and (c). Using the inverted curves (red), we can determine whether these "plateaus" arise from surface or bulk conduction channels. We see dramatic differences in the inverted resistance results for each sample. Fig. 5.3 (a) shows a resistance that drops and saturates, similar to the non-stoichiometric flux growths observed previously. [110] The inverted resistance measurement shown in Fig. 5.3 (d) has a feature similar to Fig. 5.3 (a) but also a moderate drop at lower temperatures. In Fig. 5.3 (b) and

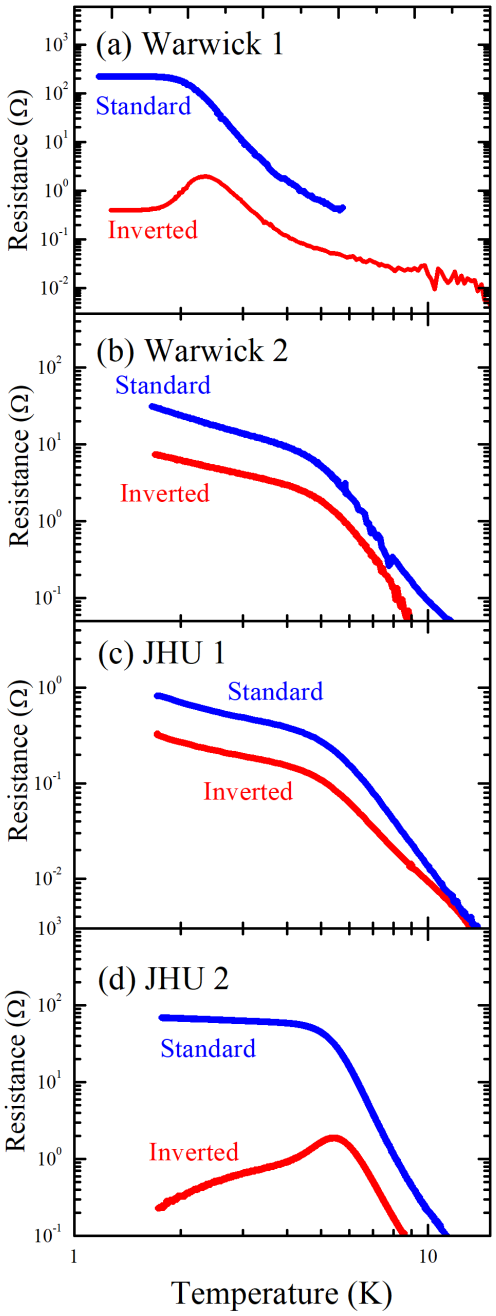

Figure 5.3: Inverted resistance measurement of four floating zone grown SmB_6 samples.

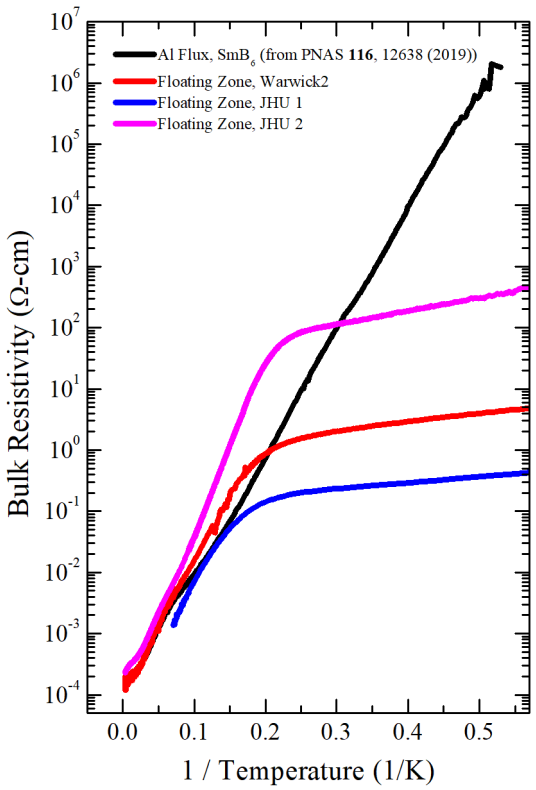

Figure 5.4: Bulk resistivity conversion from Fig. 5.3 measurements.

(c), we see a temperature dependence that is close to parallel to the standard measurement.

We convert the measured resistances to bulk resistivity in Fig. 5.4, except for the sample Warwick 1 (Fig. 5.3(a)) which was complicated to convert due to the Corbino disks being placed on different crystal planes. We compare the results from this study to the previously reported result on a stoichiometric flux-grown sample (black trace). [110] We find that the remaining three floating zone grown samples have a significant slope change in bulk resistivity which indicates that the intrinsic exponential temperature dependence in bulk resistivity is interrupted. That is, another bulk conduction mechanism is present in these samples in addition to the standard mechanism responsible for activated behavior.

5.4 Discussion

Figs. 5.3 and 5.4 show that the four floating zone samples presented here have non-negligible bulk conduction, but the characteristics of the bulk conduction differ by sample. In Fig. 5.3 (b)

and (c) the standard and inverted resistance curves are parallel to one another, demonstrating that these samples are bulk conductors and can be described by Eq. 2.16. In terms of transport, this means that either the surface conduction is nonexistent or that the bulk conduction channel dominates.

Many researchers have proposed impurities as a possible origin for residual bulk conduction in SmB_6. Most point defects come from the starting material, as rare earth elements are notoriously difficult to purify. In our samples, the starting materials were sourced from different companies, so the purity of the Sm used in the growth may differ among samples. One way to reduce rare earth impurities is via isotopic purification to Sm-154, as was done for our sample JHU 2. The only remaining rare-earth impurity is Gd-154, which is magnetic. [102] Gd impurities have been studied previously, beginning with the observation that the substitution of even 1% Gd could dramatically change the electrical properties of SmB_6. [176] Later, a Gd doped sample was used to test the TI hypothesis by searching for time reversal symmetry breaking below 4 K. [17] Gd impurities have also been shown to increase the residual heat capacity at low temperatures [102] and have been suggested as an avenue for screening of the Kondo effect at low temperatures. [120] Debate is ongoing about the role of Gd impurities; recent reports have suggested that it is not responsible for bulk dHvA oscillations. [91] However, the local environment of Gd impurities is metallic even at very low concentrations, and at higher concentrations this could lead to percolation through the sample in transport measurements. [121]

Results from the isotopically purified sample shown in Fig. 5.3 (d) have different features in the inverted resistance curve compared to the non-purified samples (Figs. 5.3 (b) and (c)). Since the standard and inverted curves are not parallel, this sample does not have dominant bulk conduction, but it may have parallel surface and bulk channels. Since the sample is isotopically pure, the bulk channel could come from the remaining Gd impurities, Sm vacancies introduced during growth, or both.

A general model of impurities used in semiconductors and other materials is the effective mass approximation, where the impurity is treated hydrogenically, with an effective Bohr radius and binding energy. [148] As discussed in Chapter 3, the conditions for standard hydrogenic impurites are not satisfied in SmB_6 when the model for semiconductors is used.

[145] However, the model introduced by B. Skinner in Ref. [105] demonstrated that the effective mass approximation can be modified for SmB_6. In the Skinner model, the quadratic potential used in the original treatment of the effective mass approximation [148] is swapped for the "Mexical hat" dispersion seen in SmB_6. New conditions for the effective radius and binding energy of the impurity state are determined. The total dc conductivity in the presence of these new impurity states is also derived and found to be a combination of the standard activated behavior with activation energy E_1 and an activated hopping term with activation energy E_3, [105]

$$\sigma(T) = \sigma_1 \exp\left(\frac{E_1}{k_B T}\right) + \sigma_3 \exp\left(\frac{E_3}{k_B T}\right). \tag{5.1}$$

This type of impurity band could be present in all samples and could describe both magnetic and nonmagnetic point impurities, including Sm vacancies. Since the addition of Sm vacancies to flux grown samples has been shown to induce bulk conductivity, [110] some portion of the residual bulk conductivity seen in this work in floating zone samples could also be due to Sm vacancies as described above. However, the magnitude of the bulk conduction seen in the inverted measurements is much greater in all the floating zone samples, including the isotopically purified sample, so it is unlikely that vacancies or impurities alone could be the origin. The possibility of hopping conduction and even insulator-to-metal transition by heavily doped foreign magnetic impurities will be discussed elsewhere in our future work.

Another possibility for the source of the residual bulk conduction is one-dimensional defects, or dislocations. As discussed earlier, a mismatch in lattice constant between a substrate and a semiconductor thin film can lead to the formation of dislocations which terminate on the surface of the film. [138] The density of dislocations in a film can be estimated by the change in lattice parameter, $n_{\text{dis}} = |1/a_1^2 - 1/a_2^2|$, where a_1 and a_2 are the lattice parameters on the two surfaces of the film.

In SmB_6, one study reports a change in lattice constant over the length of a floating zone sample. [107] Unlike the case of thin films, to the best of our knowledge there is no literature describing how to estimate dislocation density in bulk crystals where there is a variation in lattice constant. Here, we introduce a new method to understand the formation

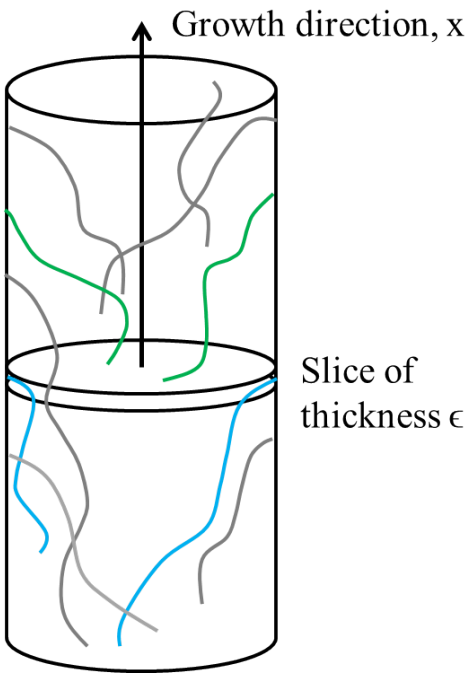

Figure 5.5: Sketch of dislocations in a floating zone boule. Some dislocations (green) initiate within a slice of thickness ϵ, and others (blue) terminate within that slice. The remaining dislocations (gray) form and terminate elsewhere in the sample.

of dislocations in bulk materials. Later, we use our model to estimate the dislocation density in SmB_6 samples. We consider a floating zone sample as its size allows for more variation of lattice parameter in the crystal compared to a flux grown sample, but dislocations are still expected to be present in flux grown crystals.

Generally, dislocations that form in films terminate on the surface of the film. In thin films, the dislocations form in the growth direction and terminate on the top surface of the film. In crystals, however, dislocations do not have to form and terminate only along the direction of growth; dislocations could also terminate on the side surfaces of the crystal, as shown in Fig. 5.5. Thus, the dislocation density in crystals is expected to depend both on the change in lattice constant in the direction of growth and on the size (radius) of the crystal.

To estimate the dislocation density, we model the floating zone rod as forming from a series of thin slices of thickness ϵ as the molten zone passes through the furnace. In analogy with the equation above for semiconductor thin films, the total number of dislocations that

nucleate within the slice is

$$\left| \frac{1}{(a(x))^2} - \frac{1}{(a(x+\epsilon))^2} \right| (\pi r^2) \tag{5.2}$$

where $a(x)$ is the lattice parameter at a location x along the growth direction and r is the radius of the crystal. A sketch of these is shown in green in Fig. 5.5. All the dislocations that form in this slice must terminate somewhere on the surface of the sample, whether on the sides or the ends. To account for the dislocation terminating on the sides, we introduce an angle θ_{d} which the dislocation makes with respect to the growth direction. Then, the number of dislocations that terminate within a slice (shown in blue in Fig. 5.5) is related to the surface area of the slice, the dislocation density (n_{dis}), and θ_{d} by

$$(2\pi r\epsilon) n_{\mathrm{dis}} \cos\theta_{\mathrm{d}}. \tag{5.3}$$

Here, $\cos\theta_{\mathrm{d}} = 1$ would correspond to all dislocations oriented along the growth direction. We expect $cos\theta_{\mathrm{d}} < 1$ in an actual sample, since dislocations are expected to terminate randomly on the surface but form with the growth of the rod. Since all the dislocations that formed must terminate, Eqs. 5.2 and 5.3 are equal. Expanding Eq. 5.2 as a Taylor series, we calculate that the estimated dislocation density is

$$n_{\mathrm{dis}} = \frac{r}{\cos\theta_{\mathrm{d}}} \frac{|\nabla a(x)|}{(a(x))^3} \tag{5.4}$$

for the dislocation density.

We can estimate the dislocation density in the sample with reported change of lattice constant from Ref. [107]. The lattice parameter in that sample was $a_1 = 4.134309$ Å on one end of the crystal and $a_2 = 4.133343$ Å on the other end, 8 cm away. The radius of the crystal was 3 mm. Using these values with Eq. 5.4, we estimate that the dislocation density in this floating zone sample is $\sim 10^{10}$ cm^{-2}.

Dislocations are commonly imaged by preparing samples as for transmission electron microscopy (TEM). However, the estimated density of dislocations we calculated is too small to use this method. Instead, we used chemical etching to reveal points where dislocations terminate on the surface. During etching, material is removed from the area near a crystal

defect at a different rate than from the lattice. The etching method allows defects, including dislocations, to be imaged optically. [137] The "etch pit" that forms also mirrors the crystal structure of the sample; for SmB_6 we expect to see square etch pits aligned with the crystal direction. With longer etching time, the size of the etch pits increases and more etch pits start to form, so that the etch pit density observed provides a lower bound on the actual dislocation density.

We used equal parts nitric and sulfuric acid diluted to 10% to etch flux grown and floating zone SmB_6 crystals. After etching, we observed etch pits using a scanning electron microscope in both types of samples. Examples of etch pits are shown in Fig. 5.6. The floating zone sample shown was etched for 340 seconds and had an etch pit density of 10^5 cm^{-2}. The flux grown sample shown was etched for 600 seconds and had an etch pit density of 2×10^3 cm^{-2}. Even though the flux grown sample was etched longer than the floating zone sample, it has a lower density of etch pits observed, suggesting that the floating zone sample hosts more dislocations than the flux grown sample. In both samples, the locations of the etch pits is nonuniform, which suggests that local inhomogeneities in temperature or stoichiometry, for example, during sample growth are important to the formation of dislocations. In both cases, the observed densities are much lower than the calculated estimate of 10^{10} cm^{-2}, but since we imaged immediately after identifying that etch pits were present, our values are lower bounds on the number of dislocations actually present in the samples. Since there is significant sample-to-sample variation in floating zone samples, it is also possible that our floating zone sample had fewer dislocations than the one in Ref. [107].

In addition to impurity hopping and dislocations, we briefly consider other theories proposed to explain some of the novel results of SmB_6. First, the proposal that SmB_6 is a nodal semimetal [100, 101] is inconsistent with the low-temperature bulk conduction that we observe, and it does not explain the difference between flux and floating zone grown samples. Our inverted resistance curves show two regions of activated behavior (above and below about 4 K) rather than activated behavior above 4 K and linear-in-T behavior below 4 K. Next, in heat transport, excess thermal conduction at low temperature was not found in flux-grown samples, and reports have disagreed about whether thermal conduction is present universally in floating zone samples. [27, 88, 89]. Theories attempting to reconcile

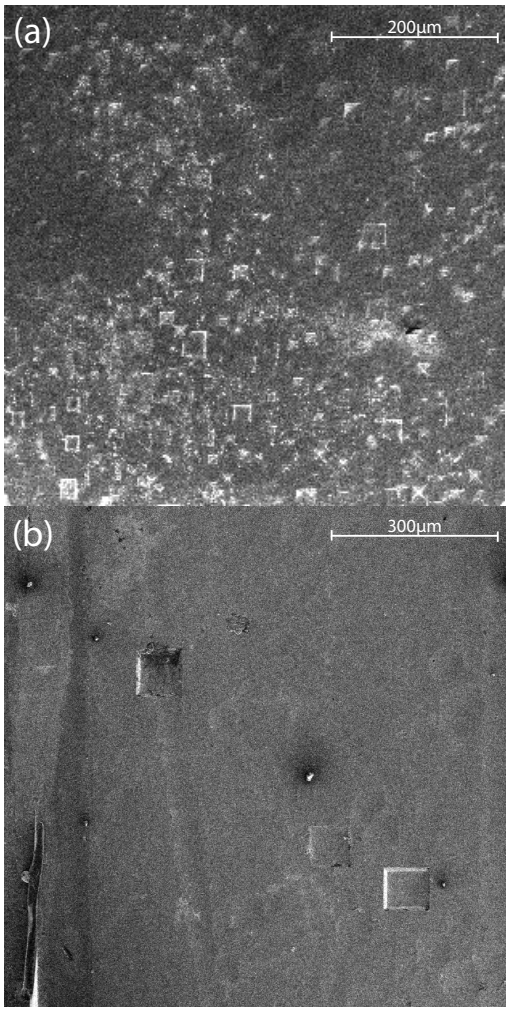

Figure 5.6: Examples of etch pits on the (001) surfaces of (a) a floating zone sample etched for 340 seconds and (b) a flux-grown sample etched for 600 seconds.

these conflicting results have focused on the possibility that the floating zone samples contain charge-neutral excitations and primarily explored their relevance to dHvA oscillations rather than transport. Our data do not provide evidence for charge-neutral excitations, but the low-temperature bulk channel we observe could conduct heat and contribute to dHvA. Even in samples with very few rare earth impurities, [91] dislocations could still contribute to these effects. A better understanding of the role of dislocations, or more generally, the conduction channel we observe here, will be an intriguing area of further study.

5.5 Conclusion

In this chapter, we performed transport measurements on SmB_6 using the inverted resistance method. Standard four-point and Hall bar geometry resistance results show nonuniversal temperature dependence below about 4 K, but the origin of this behavior is difficult to pinpoint as both bulk and surface channels are present. The inverted resistance method we used allowed us to characterize the bulk behavior at temperatures at which surface conduction dominates. We found that the four floating zone samples show bulk conduction with characteristics differing by sample. On the other hand, a stoichiometric flux-grown sample has a truly insulating bulk, and the introduction of Sm vacancies in flux grown samples was found to induce bulk conduction. In general, the bulk conduction channel seems to be significantly larger in floating zone samples compared to flux grown samples, even those grown with off-stoichiometry.

We discussed various possibilities for the origin of the new conducting channel observed here, as well as the differences between the floating zone results presented here and the flux-grown samples presented in the previous work. [110] We especially considered impurities, which could be magnetic, like Gd, or non-magnetic, including defects like Sm vacancies. Our experimental results are consistent with the Skinner model [105] for impurity hopping conduction at low temperatures with an activated transport behavior. In addition, we considered one-dimensional defects, or dislocations, extending throughout the sample. We observed a small dislocation density in both flux and floating zone samples via chemical etching, with a larger dislocation density observed in floating zone samples compared to flux grown samples.

While this is consistent with the relative amounts of bulk conduction observed in samples grown by each technique, further work to explore the characteristics of the dislocations is needed to verify that they contribute to bulk conduction with a magnitude agreeing with our inverted resistance data. Future work could include characterizing the mobility of the channel or thermal studies of the role of dislocations in SmB_6.

Chapter 6

Exploring Surface Physics Using Hall Bar Geometry and Ionic Liquid Gating

6.1 Introduction

The previous chapters have focused on bulk behavior of SmB_6, including at temperatures where surface conduction dominates. However, characterizing the conductive, and possibly topological, surface has been a major focus of research into SmB_6 in the last few years. As introduced in Chapter 1, the surface conduction in SmB_6 has contributions from a pocket near the Γ point and from two identical pockets at the X points in the (001) Brillouin zone. Experimental efforts to pinpoint the properties, especially carrier density and mobility, of these pockets have been numerous, although results obtained using different experimental methods disagree significantly. The X pocket has a larger carrier density than the Γ pocket, making study of the Γ pocket an additional challenge. Recent work by Eo, et al. [173] used a Corbino disk to study conduction on a single crystal surface of SmB_6, resulting in estimates for the parameter space of the carrier density and mobility of the two pockets on the (001) surface. Additionally, this work initially suggested that Corbino disk geometry is optimal for studying surface physics, whereas Hall bar geometry is best suited for bulk studies.

In this chapter, the work of Eo, et al. [173] is extended using Hall bar geometry. First, subsurface cracks, which can be reduced by polishing but never completely eliminated, are included in the analysis of surface conductivity. For a Hall bar geometry, where both ρ_{xx} and ρ_{xy} are measured, we show that conductivity through cracks can effectively be eliminated, making Hall bar geometry much more powerful than previously thought for studying the surface. Our analysis of the Hall bar yields a Hall conductivity that is proportional to the square of the mobility, so in materials with multiple conduction channels, the higher mobility channel dominates. In SmB_6, the higher mobility channel is the Γ pocket, which is difficult to access using other experimental methods due to its small carrier density.

Yet more information can be obtained from the surface channels by gating the surface. In SmB_6, since all the surface are conductive, a traditional metallic gate is impractical. Instead, an ionic liquid is used to apply voltage to a sample, in a method known as ionic liquid gating. When voltage is applied to the ionic liquid and thus to the sample, the surface charge (or carrier density) can be tuned within a narrow range. When used in conjunction with Hall bar geometry, ionic liquid gating allows the carrier density of the Γ pocket to be tuned. In this chapter, we also present ionic liquid gating results on an SmB_6 Hall bar, and use the results to further constrain the parameter space on the (001) surface from Ref. [173]. Before measuring SmB_6, we also performed a "control" measurement of ionic liquid gating on N-polar GaN, which has a high carrier density and a two-dimensional electron gas (2DEG) close to the surface, making it simple to tune using gating.

Finally, ionic liquid gating was noted in Chapter 3 as one method of testing whether the band bending model is accurate. If band bending is correct, a change in surface charge would shift the location of the 10-15 K feature. The results presented in this chapter show that the 10-15 K feature does not change with gating.

6.2 Surface characteristics of SmB_6

Topological Kondo insulator theory predicts that three surface Fermi pockets exist, each surrounding a high symmetry point in the Brillouin zone. [70] In particular, on the (001) crystal surface, theory predicts that one of the Fermi pockets should be centered at the Γ-

point (also called the Γ pocket), and the other two should be centered at the X point (called 2X pockets in the remainder of the chapter). A straightforward way of identifying that the predicted pockets are present is via Shubnikov-de Haas (SdH) oscillations, but in SmB_6 these have not been observed up to 80 T. Instead, following Ref. [173], a possible parameter space for the carrier density and mobility of these pockets will be constructed using a combination of theoretical arguments and experimental data. The constructed parameter space is shown in Fig. 6.1.

First, there are fundamental limits in two-dimensional transport that constrain the parameter space. One constraint is the k_F limit, or that the size of the Fermi pockets cannot be larger than the surface Brillouin zone of the material. In SmB_6, the total area of the surface Brillouin zone corresponds to a carrier density of 1.17 $\times 10^{15}$ cm^{-2}, so this places an upper limit on the carrier density. In Fig. 6.1, this constraint is indicated in the darkly shaded area on the right of the plot. Additionally, the Ioffe-Regel criterion indicates that the system would undergo a metal-to-insulator transition when the surface resistance becomes larger than the quantum of resistance, h/e^2. Thus, this region, indicated in the darkly shaded triangle in the lower left of Fig. 6.1 is also excluded from the parameter space. A final, although less strict, constraint is that SdH oscillations have not been observed up to 80 T. The magnetic field strength at which SdH oscillations appear is inversely proportional to mobility, so the surface mobility would be constrained to be smaller when the onset of SdH oscillations is at higher fields. This is shown as a gradient in the upper left-hand corner of Fig. 6.1.

To further constrain the parameter space, experimental results are used. When compared with the parameter space, transport using Hall bar geometry usually yields carrier densities in the 10^{15} cm^{-2} or higher range, making them violate the k_F limit. One possible reason for this is that current can flow on all the surfaces, so a single (001) surface is not isolated. Instead, Corbino geometry can be used to isolate a single surface. Additionally, the carrier density and mobility extracted from a Corbino measurement is usually within the theoretically allowed region of the parameter space. The carrier density and mobility extracted from a Corbino disk prepared on a mirror-polished SmB_6 surface is shown as a triangular point in Fig. 6.1. The result places an upper bound on the conductivity, indicated

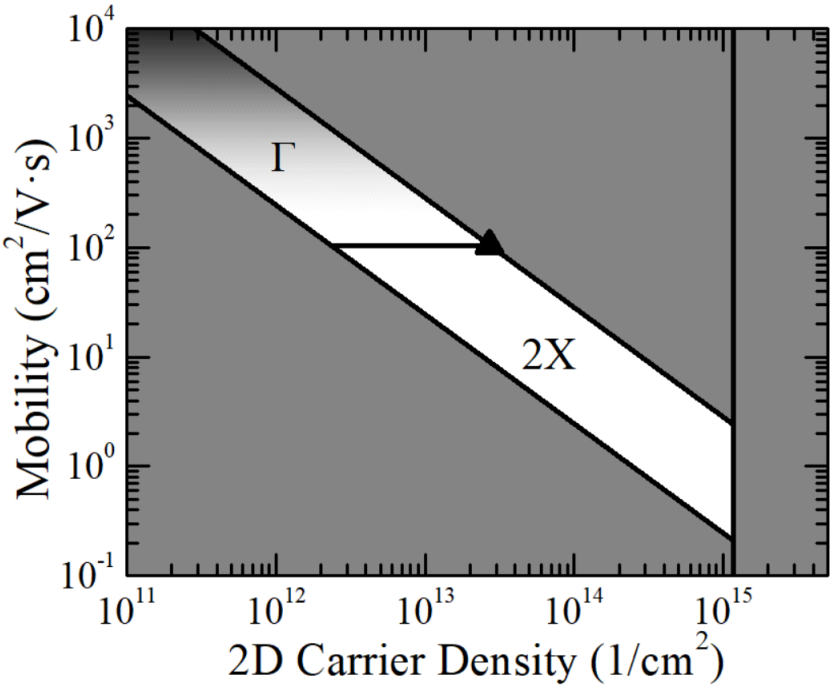

Figure 6.1: Parameter space of SmB_6 on the (001) surface.

by the diagonal line intersecting the triangular point in the figure. Additionally, the Γ and 2X pockets contribute similarly to the conductivity, meaning that one should have a larger carrier density and smaller mobility, and the other should have a smaller carrier density and a larger mobility. This is indicated in Fig. 6.1 by breaking up the remaining white space (the allowed parameter space) into sub-spaces for the Γ and 2X pockets. By comparing with ARPES data, the best estimates for the Γ pocket were $n = 8 \times 10^{12}$ cm^{-2} and $\mu = 170$ cm^2/V·s, and the best estimates for the 2X pocket were $n = 2 \times 10^{14}$ cm^{-2} and $\mu = 10$ cm^2/V·s.

This parameter space does provide reasonable ranges for the carrier density and mobility of the two pockets on the SmB_6 surface, but is it possible to further constrain the parameters? One remaining problem is the role of subsurface cracks. Although the Corbino measurement used to construct the parameter space was polished with grit sizes down to 0.3 μm, subsurface cracks or defects, like voids, could still be present in the sample. These cracks would create another surface on which current could flow, and their geometry is impossible to account for in the analysis. Instead, without knowing the actual conductivity in subsurface cracks

in a given sample, this parameter could be eliminated from the analysis by performing two complementary measurements. In the following section, we show that Hall bar geometry can do just this; it allows conductivity through subsurface cracks to be eliminated by considering both the resistance and the Hall coefficient.

6.3 Accounting for cracks in transport analysis

Normally, Hall bar results are used to calculate the carrier density and mobility. To review from Chapter 2, in a standard analysis including a magnetic field in the z-direction, these are extracted from the x-y conductivity matrix,

$$\sigma = \begin{pmatrix} ne\mu & ne\mu^2 B \\ ne\mu^2 B & ne\mu \end{pmatrix} \tag{6.1}$$

where n is the carrier density, μ is the mobility, e is the electric charge, and B is the magnetic field. The longitudinal and transverse resistance are

$$\begin{aligned} R_{xx} &= \frac{1}{ne\mu} \\ R_{xy} &= \frac{B}{ne}. \end{aligned} \tag{6.2}$$

Then, carrier density can be found from R_{xy} and mobility from n and R_{xx}. Carrying out this process for our data yielded surface carrier densities of order 10^{15} cm^{-2} or higher, which is a usual order of magnitude for Hall bar carrier densities. Proper surface preparation (polishing) can reduce the carrier density, but the values are still higher than is observed in any other experimental method. However, the size of the surface Brillouin zone (k_F limit) in SmB_6 restricts the maximum carrier density to 1.17×10^{15} cm^{-2}. Previous results on a Corbino disk also suggest that the surface carrer density is closer to 2.7×10^{13} cm^{-2}. [173]

One way to improve agreement and ensure that the carrier density extracted from a Hall bar is physical is to include conduction through subsurface cracks. To do this, we add a term for the conductivity through the cracks, σ_{cr}, to the conductivity matrix. This term should only be added to the diagonal elements, as the subsurface cracks are oriented randomly

and thus are unlikely to contribute to the Hall conductivity. The new conductivity matrix becomes

$$\begin{pmatrix} ne\mu + \sigma_{\mathrm{cr}} & ne\mu^2 B \\ ne\mu^2 B & ne\mu + \sigma_{\mathrm{cr}} \end{pmatrix}. \tag{6.3}$$

The new results for the longitudinal and transverse resistance are

$$\begin{aligned} R_{xx} &= \frac{1}{ne\mu}\left(\frac{1}{1+\sigma_{\mathrm{cr}}/(ne\mu)}\right) \\ R_{xy} &= \frac{B}{ne}\left(\frac{1}{1+\sigma_{\mathrm{cr}}/(ne\mu)}\right)^2. \end{aligned} \tag{6.4}$$

These new expressions are both modified from Eq. 6.2 by the same factor containing the conductivity of the cracks, although this factor is squared in R_{xy}. By dividing the two equations, we can obtain a crack-independent quantity,

$$\frac{R_{xy}}{R_{xx}^2} = ne\mu^2 B. \tag{6.5}$$

This is also equal to the off-diagonal term in the conductivity matrix, or σ_{xy}. Thus, in a system with multiple channels, the term on the right hand side of Eq. 6.5 would simply be summed over all the channels. The new equation allows a relationship between the carrier density and mobility to be extracted from data, but the exact values of both cannot be determined explicitly just from the measurement. The expression in Eq. 6.5 is general and could be applied to any surface conductor measured by Hall bar geometry, but it is especially useful in materials where subsurface cracks are present.

To proceed, we consider the specific case of the Γ and 2X pockets in SmB_6. A Hall bar measurement would yield the relation in Eq. 6.5, modified for two channels:

$$\sigma_{xy} = n_\Gamma e\mu_\Gamma^2 B + n_{2X} e\mu_{2X}^2 B. \tag{6.6}$$

From Ref. [173], the Γ pocket has an estimated carrier density of 8×10^{12} cm^{-2} and mobility of 170 cm^2/V·s, while the 2X pockets have an estimated carrier density of 2×10^{14} cm^{-2} and mobility of 10 cm^2/V·s. This means that the Γ pocket, which has the higher mobility

of the two surface pockets, dominates the Hall conductivity in SmB_6. In contrast, surface conductivity measured by a Corbino disk contains equal contributions from both pockets, and still may depend on an unknown amount of conduction through subsurface cracks:

$$\sigma_{xx} = n_\Gamma e\mu_\Gamma + n_\Gamma e\mu_\Gamma + \sigma_{cr}. \tag{6.7}$$

This suggests that although the Corbino disk is the best transport method for isolating a single surface, it lacks the ability to independently characterize the Γ and 2X pockets of SmB_6 (or more generally, characterize individual channels in a two-dimensional conductor). Other methods like ARPES or quantum oscillations can more readily probe the X pocket, as it has a higher carrier density than the Γ pocket. In contrast to these, in the new method presented here in Eq. 6.6, the dependence on the square of the mobility means that the higher mobility channel dominates. Effectively, this means that the Γ pocket can be probed using this method of analysis with simple Hall bar geometry.

In the following sections, these methods are used to analyize Hall bar results on SmB_6. To extend these measuremens, ionic liquid gating is also used to try to change the surface characteristics. Before discussing the ionic gating results, the method will be introduced in the next section.

6.4 Introduction to ionic liquid gating

6.4.1 Properties of the ionic liquid

Ionic liquids are often employed in research involving electric double layer (EDL) devices for energy storage applications. [177, 178] They are generally formed between two large organic molecules with a weak ionic binding. [177]. Upon application of a voltage to the ionic liquid, the ions separate; if positive voltage is applied on an electrode, a layer of negative charges builds up around the electrode, and a layer of positive charges builds up far from the electrode. [179] This effectively applies a positive voltage to the sample in a similar way to a traditional metallic gate.

In the present experiments, the ionic liquid N,N-diethyl-N-methyl-N-(2-methoxyethyl)

ammonium bis(trifluoromethylsulphonyl)imide (DEME TFSI) was used. This liquid has a high ionic conductivity, [179] so it can serve as an efficient medium for applying voltage to the sample. In addition, it leaks charge very little as the temperature is reduced, so the voltage applied to the sample is stable over a large temperature range. [180] However, DEME-TFSI has a glassy transition at 182 K, [179, 178] so the applied voltage must be changed at higher temperatures. The breakdown voltage of DEME-TFSI is also rather large (2-3 V) compared to other ionic liquids, [178] but it is unclear whether damage to the liquid is permanent if too large of a voltage is applied. DEME-TFSI may also have a finite response time, likely due to the size of the molecules hindering movement when voltage is applied.

Ionic liquids are ideal for gating experiments in materials with a large active region. When metallic gates are used on a large active region, often they can have leakage issues that impede experimentation. In SmB_6, all the surfaces are conductive, so the ideal way to gate would be to gate all the surfaces at once. Since SmB_6 is generally a macroscopic crystal, this would not be feasible with a metallic gate. Using an ionic liquid instead allows voltage to be applied to all surfaces of the sample.

6.4.2 Control measurement in N-polar GaN

Since SmB_6 is a challenging material to understand, ionic gating measurements were initially performed on N-polar GaN high-electron mobility transistors (HEMTs). This work on GaN was published in Applied Physics Letters, vol. 114, p. 162102 in 2019, [181] but only the aspects relevant to ionic liquid gating on SmB_6 are presented here. GaN HEMTs have many high-power and high-frequency applications due to their large band gap of 3.4 eV and high electron mobility in the 2DEG. [182, 183, 184, 185] They can have Ga polarity or N polarity; most GaN studies for past applications have focused on Ga-polar devices, but N-polar devices now seem to have many advantages. In N-polar HEMTs, the two-dimensional electron gas (2DEG) forms on top of the barrier (the larger bandgap material) whereas in Ga-polar HEMTs the 2DEG is positioned below the barrier. This allows for better confinement of the 2DEG in N-polar devices compared to Ga polar, as well as better control of the device via gating. [186] One reason that Ga-polar devices were previously favored was that N-polar devices are harder to grow epitaxially in comparison. [187] Thus, there are very few transport

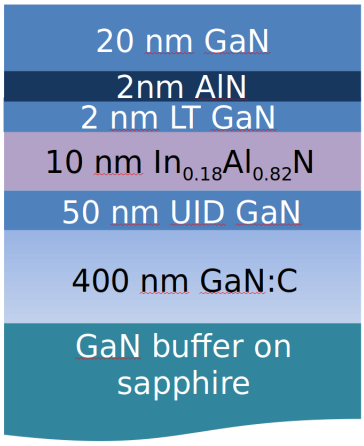

Figure 6.2: Epistructure of the GaN HEMT studied in this work. The sample was grown on a miscut semi-insulating GaN-on-sapphire template using plasma-assisted molecular beam epitaxy.

studies on N-polar GaN.

In the published work, [181] temperature-dependent Shubnikov-de Haas and Hall measurements are reported and the carrier density and mobility are presented. The presence of persistent photoconductivity (PPC), or an increase in carrier density after illumination, was also tested. It was not observed in the N-polar samples, in contrast to past work on Ga-polar samples. [188, 189, 190, 191] Since PPC has been utilized to change charge density in the channel in electron transport [192, 193], we further investigated the charge density using ionic liquid gating.

The heterostructure of the GaN sample used in the ionic gating measurements is shown in Fig. 6.2. The transport geometry was lithographically defined van der Pauw geometry with Ohmic contacts. Magnetotransport measurements were carried out using a low-frequency ac technique in a Quantum Design 14 T Physical Property Measurement System. Since DEME-TFSI may be reactive with water vapor, it was applied to the sample immediately before loading into the cryostat, to prevent possible reaction with air. To prevent breakdown, gate voltages from -1 V to $+2$ V in steps of 0.5 V were tested. An adjacent Au pad was used as a gate electrode. Each voltage was applied at 250 K, above the glassy transition temperature. The sample was subsequently cooled to 1.7 K, where the longitudinal resistance was measured in one van der Pauw configuration. The system was then warmed back to 250 K before applying the next gate voltage.

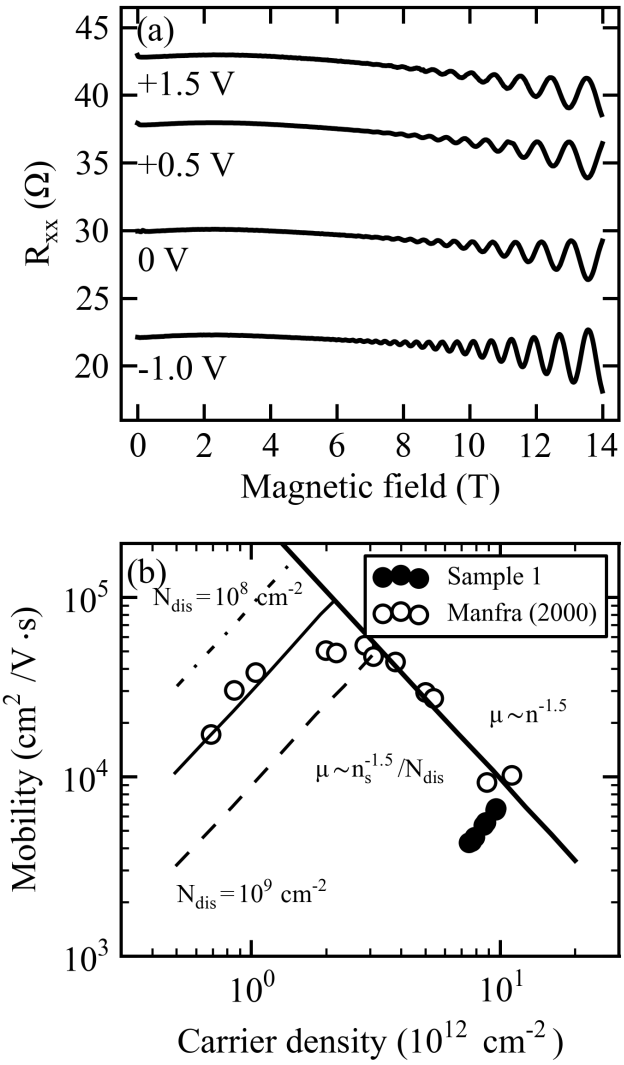

Figure 6.3: (a) Resistance of N-polar GaN sample at selected voltages applied to the ionic liquid. (b) Carrier density vs mobility extracted from resistance and Hall resistance (filled circles) shown with data and fits from Manfra, et al. [194] (unfilled circles and lines).

Figure 6.3(a) shows traces for selected gate voltages. Changing the gate voltage on the liquid affects both the magnitude of the measured resistance and the period of the oscillations. The carrier density was extracted for each gate voltage and showed a change from 7.5×10^{12} cm^{-2} at -1 V to 9.6×10^{12} cm^{-2} at $+2$ V, but no second sublevel (which would correspond to a second oscillation frequency) was observed during this measurement. Mobility was also extracted and showed a corresponding change, as shown in Fig. 6.3(b). In Ref. [181], this figure was used to understand the differences in scattering mechanism between our N-polar device (filled circles) and a previous result for traditional metallic gating on a Ga-polar device with a similar defect density (unfilled circles, from Manfra, et al. [194]). For the purposes of ionic gating, the experiment on GaN indicated that ionic liquid gating is a powerful tool for changing the carrier density and mobility of a material. By comparing with a traditionally gated result, we find that ionic gating does not allow for as wide of a range in carrier density or mobility to be probed, but its effects are qualitatively similar.

6.5 Ionic liquid gating on SmB_6

We then performed a similar measurement on an SmB_6 sample. In this sample, we measured the resistance and Hall effect at low temperatures at a variety of gate voltages using Hall bar geometry. We used sample S1 from the previous chapter; this sample was flux grown, so it was thinned to ensure that no Al inclusions remained. It was also polished on the four sides making up the active region of the Hall bar with progressively smaller grit sizes down to 0.3 μm. The Hall bar geometry was defined by e-beam lithograhy followed by metallizing with Ti/Au. Contacts were initially made using silver paste, but these were not strong enough to withstand the glassy transition of the ionic liquid. Instead, contacts were made using indium and gold wire. To allow all surfaces of the sample to be gated, the sample was suspended in a small Si boat. An adjacent indium contact was used as a gate electrode. Measurements were performed in a 14 T Dynacool Quantum Design Physical Property Measurement System (PPMS) with an SR830 lock-in amplifier.

As with the GaN experiment, DEME-TFSI was used, and it was applied immediately before loading the sample into the cryostat to prevent possible reaction with air. Gate

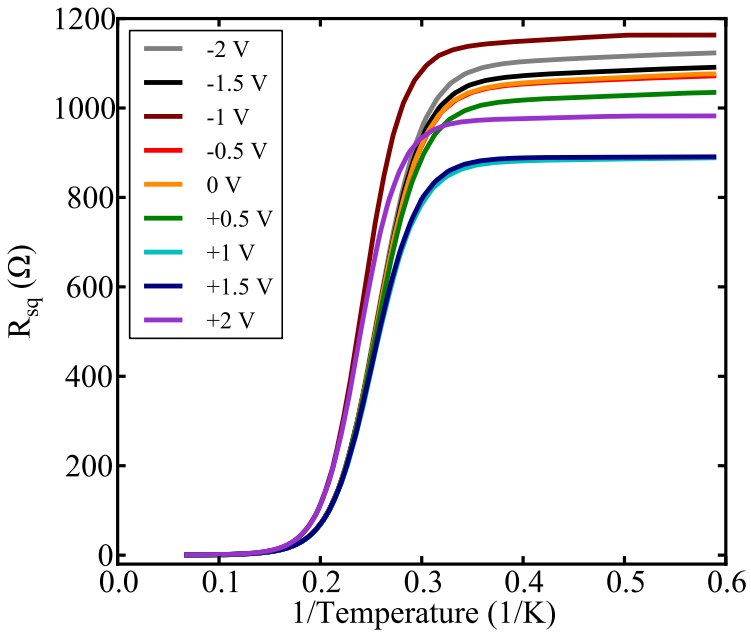

Figure 6.4: Surface resistance of SmB_6 from 1.7-20 K at gate voltages between -2 V and $+2$ V.

voltages from -2 V to $+2$ V were tested, and each gate voltage was applied at 300 K. Keeping the reported finite response time of the liquid in mind, we found that the applied voltages were most accurate when the liquid was allowed to rest at the newly applied gate voltage at 300 K before cooling down; we used a resting time of 30 minutes. Additionally, the voltages were applied in order of their magnitudes, i.e. $+0.5$ V, then $+1$ V, then $+1.5$ V, etc. which seemed to enhance the accuracy of each trace. The liquid rested at 0 V overnight between applying the positive and negative voltages. Each voltage was also applied at zero magnetic field; for Hall effect measurements the field was applied below the glassy transition temperature to avoid any magnetic effects on the ions in the liquid.

The resistance of the sample from 1.7 K to 20 K at all the gate voltages tested is shown in Fig. 6.4. Instead of presenting the as-measured resistance R, we present the surface resistance as R_{sq}. This method is chosen as ionic gating is expected to change the surface properties below 4 K. The results show a change of about 200 Ω over all the gate voltages measured, meaning that gating does change the surface characteristics of SmB_6. However, the magnitudes of the plateaus do not follow a consistent relationship with the gate voltages.

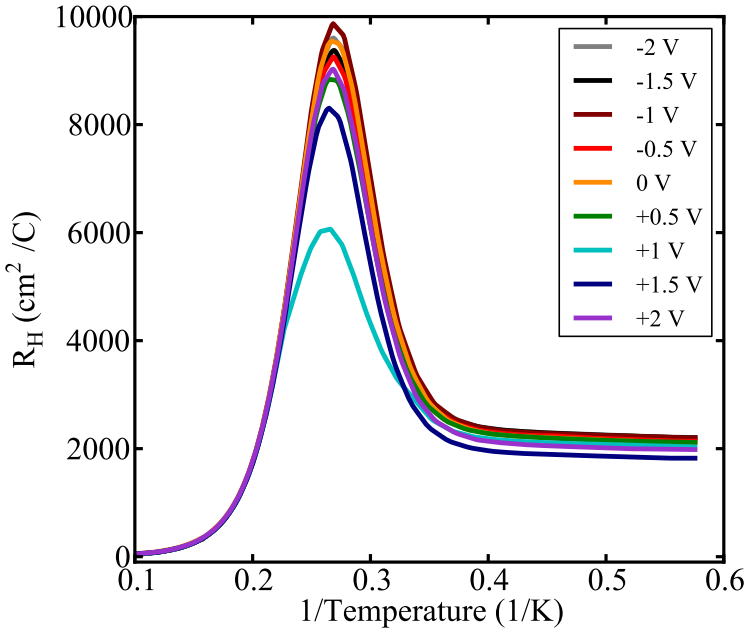

Figure 6.5: Surface Hall coefficient of SmB_6 from 1.7-20 K at gate voltages between -2 V and $+2$ V.

The lack of a consistent relationship between gate voltage and plateau magnitude was observed in all ionic gating trials we performed on this sample, but the data set presented here most clearly demonstrates the effects of gating on the surface. It is also unclear why some of the traces have a temperature-independent plateau while the others have some temperature dependence below 4 K.

The Hall coefficient from 1.7 K to 20 K at all the gate voltages tested is shown in Fig. 6.5. Again, the data are presented as the two-dimensional Hall effect to highlight the changes in the surface properties. The results show a change of about 2000 $cm^2/V{\cdot}s$ at the lowest temperature over all the gate voltages measured. Again, the magnitudes do not follow a consistent relationship with the gate voltages, but the ordering of the traces for negative voltages is consistent with what was seen in resistance. In addition, since the original purpose of this study was to test the 10-15 K feature, we found that ionic gating had no effect on the feature in the Hall coefficient, contrary to what would be expected from the band bending model.

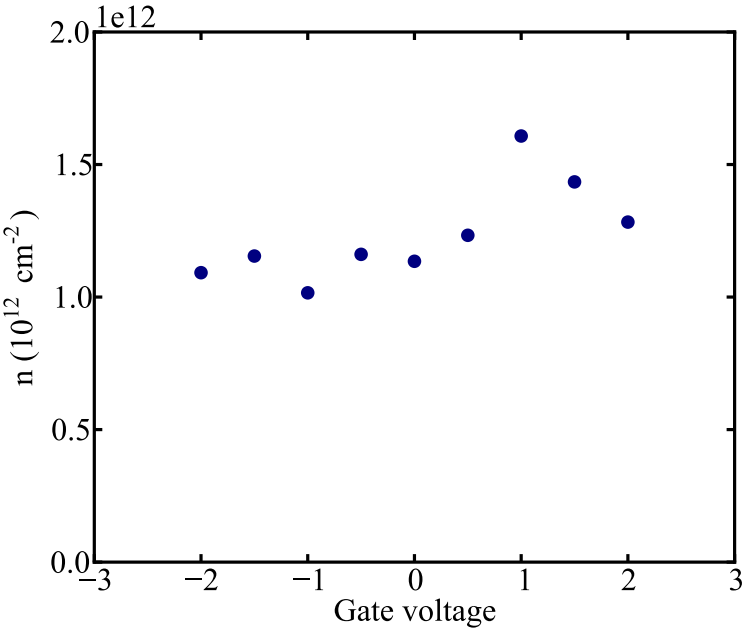

Figure 6.6: Estimated carrier density using Eq. 6.6.

6.6 Discussion

Using the analysis method for Hall bar geometry introduced above, we can estimate the carrier density and mobility in SmB_6. First, we consider the ionic gating results to determine whether the carrier density was affected. Using the estimated mobility values obtained from the previous Corbino disk results, the carrier density is estimated at all gate voltages from the measurement. A plot of carrier density versus gate voltage for the data in Figs. 6.4 and 6.5 is shown in Fig. 6.6. This analysis method shows a small change in carrier density from about 1.5×10^{12} cm^{-2} to about 1.7×10^{12} cm^{-2}. The change in carrier density is small and does not show a clear trend like what was seen in GaN, but this is expected as the SmB_6 surface is more complex than a semiconductor 2DEG.

Next, to improve the overall estimates of the carrier density and mobility on the surface, mobility is left as a parameter, and the quantity $n\mu^2$ from Eq. 6.5 is computed for the range of voltages measured in the ionic liquid. The $n\mu^2$ results from the highest voltage and the lowest voltage are added to the parameter space obtained earlier using the Corbino disk, shown as the two new parallel lines in Fig. 6.7. The overlap of the new constraint with the

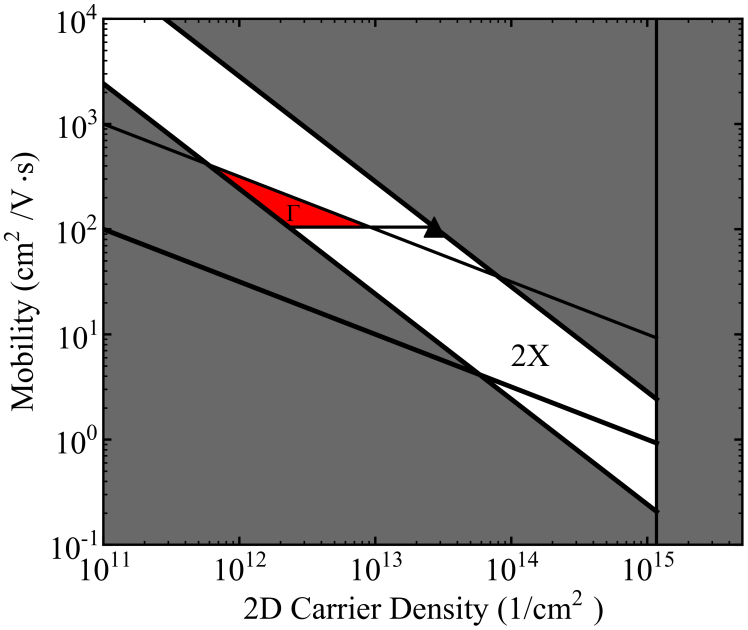

Figure 6.7: Parameter space of the Γ and 2X pockets estimated using both Corbino and Hall bar geometry. The triangle indicates the conductivity measured by a Corbino disk [110], and the red shaded area indicates the new estimate for the Γ pocket.

constraints from the Corbino disk create a new, smaller parameter space for carrier density and mobility for the Γ pocket, shown in red in Fig. 6.7. The estimated carrier density and mobility of the Γ pocket based on the new constraint are 2.5×10^{12} cm^{-2} and 150 cm^2/V·s, respectively. These values agree with the estimated carrier density and mobility from the Corbino disk and ARPES results.

The leading source of error remaining in the analyzed data is due to the contact geometry. Both the size and location of the contacts are very important. To partly address these, we used e-beam lithography to ensure that the Ti/Au contact pads were all the same size and were aligned perfectly with each other. However, wiring with indium adds some error to this as occasionally the indium contact exceeds the size of the contact pad. To reduce error in geometry, the size of the contacts should be reduced as much as possible while still preserving their alignment and uniformity with each other. We believe that reducing contact size would not only lead to more accurate transport parameters, it may also improve the clarity of results obtained in the ionic gating experiment.

6.7 Conclusion

In this chapter, properties of the surface in SmB_6 were investigated. Previous work to determine an allowed parameter space of carrier density and mobility on the (001) surface was reviewed. To extend this work, a new method of analyzing Hall bar geometry was introduced. This new method significantly improves the accuracy of carrier density and mobility extracted from Hall results, making them well within the parameter space. More importantly, the Hall conductivity in the new analysis is independent of any conduction through subsurface cracks, and it is proportional to the square of the mobility. Thus, Hall bar geometry can be used to study the high-mobility, low-carrier density Γ pocket in SmB_6. This is significant because the Γ pocket, with its lower carrier density, can be difficult to access using many experimental methods. In addition, Hall bar geometry was previously thought to be a poor way to study the SmB_6 surface; this work demonstrates that it can be used together with Corbino measurements to obtain a complementary picture of the surface. The improved Hall analysis also prevents significant overestimation of the surface carrier density.

To further study the SmB_6 surface, ionic liquid gating was performed. An initial measurement on N-polar GaN was included to demonstrate how ionic liquid gating would work in the case of a straightforward 2DEG. Then, resistance and Hall effect measurements as a function of temperature for different gate voltages from -2 V to $+2$ V were presented. By analyzing the ionic gating results using the crack-independent Hall conductivity, a new constraint was placed on the parameter space for the (001) surface, specifically narrowing down the allowed space of the Γ pocket. A major source of error remaining in these Hall bar measurements is due to the contact size and alignment, so by improving the geometry, a more precise parameter space could be developed.

Chapter 7

Conclusion and Outlook

7.1 Summary

Samarium hexaboride is a fascinating material with an extensive history. Its resistivity-temperature curve shows metallic behavior at room temperature, activated behavior from about 5-50 K, and a plateau in resistivty below 4 K. The activated behavior was explained when SmB_6 was identified as the first Kondo insulator, in which the f and d bands hybridize to open a small gap at the Fermi energy. Additionally, SmB_6 is a classic mixed valence compound, where an overall noninteger valence appears due to rapid fluctuation between two integer valence states. Most recently, the plateau in resistivity was predicted to arise from topology, and SmB_6 was predicted to be the first topological Kondo insulator. Significant experimental effort, including electrical and magnetotransport, angle-resolved photoemission spectroscopy, and quantum oscillations, as well as more exotic methods, has been dedicated to understanding the role that topology may play in SmB_6. However, little consensus has been reached, and more questions have been raised. In this dissertation, a few of these open questions were addressed, including a model of the hybridization gap in Chapter 3, high-temperature bulk behavior and the role of skew scattering in Chapter 4, a new bulk conduction channel below 4 K arising from impurities or dislocations in Chapter 5, and the surface carrier density and mobility using the Hall effect and ionic gating in Chapter 6. Also considered were the role of sample growth technique, the importance of surface preparation,

and improving the analysis of transport measurements.

In Chapter 3, Poisson's equation was solved self-consistently across the bulk of SmB_6 in the case of a bulk that behaves like an intrinsic semiconductor and a conductive surface that may or may not arise from topological effects. In an intrinsic semiconductor, the activation energy is expected to be half the total gap size, but experimental results on SmB_6 suggest that the total gap size is 20 meV while the activation energy is just 3 meV. By including the conductive surface, however, the valence and conduction bands bend significantly near the surfaces, which allows the total gap to remain the same but reduces the activation energy, as is seen in experiment. Semiclassical transport was used to connect the band structure to measurable parameters; specifically the Hall coefficient and the Seebeck effect. The results simulated a feature near 10-15 K which is observed in experimental reports of both parameters. Finally, ways of experimentally verifying the results were introduced: varying the thickness, which would change where band bending becomes important in the bulk, or varying the surface charge, which would change the strength of the bending effect near the surface. These were tested by performing Hall effect measurements on samples of various thicknesses, including a Hall bar of 2 μm thickness prepared by focused ion beam, but no difference was observed. Ionic liquid gating was used to change the surface charge, but again the predicted difference was not observed. Band bending is likely not the correct scenario for describing SmB_6; the model was simplified too much and improving the assumptions would yield better results. A later, related, study [105] reformulated the effective mass approximation for the correct dispersion in SmB_6 and instead found that in-gap impurity states are justified and described by a different effective radius, and this model is much more appropriate for understanding impurity states and the gap in SmB_6.

Chapter 4 focused on the Hall coefficient from 5-400 K, where standard bulk conduction dominates. A well-known feature in this temperature range is a sign change near 65 K in the Hall coefficient; below about 65 K the sign is negative, and above 65 K the sign is positive. By extending the measurements to 400 K, a second sign change was observed, and the Hall coefficient changes back to negative above about 305 K. Since electrons are the dominant charge carrier in SmB_6, the negative sign change is known to be the correct one, but the positive sign between 65 and 305 K is also well-known in heavy fermion systems to arise

from skew scattering due to the strong correlations. A qualitative model of skew scattering is presented in SmB_6 by considering the band structure and that only electrons near the Fermi energy participate in transport. This model can explain the two sign changes we observe: above 305 K, standard scattering from phonons or impurities dominates; when the Hall sign is positive, skew scattering dominates; and when the Kondo gap begins to open up, the sign is again negative, correctly reflecting the sign of the carriers. The effect of the positive sign on transport analysis is discussed, and a method for extracting the correct Hall mobility in the presence of an incorrect Hall sign is presented. This chapter also shows Hall bar transport data below 5 K, including the wide variation between samples, especially samples grown by different techniques.

A closer look at the low-temperature behavior was presented in Chapter 5. Here, inverted resistance measurements were used to study bulk behavior of SmB_6 at temperatures where surface conduction dominates. Prior results on Al flux grown samples were shown, and they were then compared with results on floating zone grown samples. The two types of samples behaved very differently below 5 K; pure Al flux samples showed activated behavior to the lowest temperature measured, but pure floating zone samples showed significant bulk conduction. This low-temperature bulk conduction is a previously unreported conduction channel, and it may partially explain why transport data varies so much, especially when comparing flux and floating zone samples. The low-temperature bulk channel is attributed to a combination of impurity scattering after the model by Skinner, et al. [105] as well as scattering through one-dimensional defects, or dislocations. Although dislocations are expected to be present, their presence is verified experimentally by chemical etching and imaging with a scanning electron microscope.

In Chapter 6, the focus was on transport on the conductive surface of SmB_6. First, previous work on creating a parameter space of carrier density and mobility from theory and Corbino measurements was summarized. The Corbino disk is generally considered a superior method for studying the surface of SmB_6 since the geometry constrains current to flow on a single surface. However, Hall bar geometry was shown to provide complementary information to the Corbino disk. Conduction through subsurface cracks pollutes measurements of the surface, and combining the resistance and Hall coefficient measurements available in Hall bar

geometry allows a crack-independent quantity to be determined. This quantity is dependent on the square of the mobility, so in a material like SmB_6 with two types of surface pockets, the higher mobility pocket dominates. In SmB_6, the high mobility pocket is the Γ pocket, which tends to be difficult to probe experimentally due to its low carrier density; the work in this chapter demonstrates that Hall bar geometry is in fact able to probe properties of this elusive pocket. Ionic liquid gating measurements are also presented to extend information about the Γ pocket. The crack-independent quantity is used to further constraints on the Corbino parameter space, further cornering the carrier density and mobility for the Γ pocket.

Overall, these studies reflect that Hall bar geometry is an extremely useful transport geometry in SmB_6. However, it often cannot be analyzed using the standard textbook equations to find the carrier density and mobility. At high temperatures, the effect of skew scattering was found to give the wrong sign of the carriers and a negative mobility by using the textbook analysis. This was improved by combining Hall bar data with ARPES. At low temperatures, Hall bar geometry was previously thought to be a poor way of studying the surface, but by analyzing it in a slightly different way, new information can be obtained.

Another important theme of this dissertation is that the bulk of SmB_6 is quite complex. Many of the modern studies have focused on understanding the surface, but a complete picture of the bulk is also necessary to gain a full understanding of the material as a whole. For example, skew scattering is extremely important at high temperatures, while material defects could dominate bulk conduction at low temperatures. It is likely that a full understanding of the bulk will be even more important to SmB_6 than determining properties (including topology) of the surface.

7.2 Future work

7.2.1 Ionic gating and contact geometry

The ionic gating measurements shown in Chapter 6 were performed multiple times on the same sample, and the results were not very consistent. While inconsistency is a more general problem in SmB_6, the ionic liquid gating measurement could be improved. First, although

some properties of the liquid DEME-TFSI are reported in literature, they are mainly geared toward capacitor applications rather than using the liquid as a gate. Systematic studies of the properties of the ionic liquid are currently underway in our group, and this should improve outcomes of ionic gating experiments on SmB_6.

In addition, contact geometry was recognized as a significant source of error. Although this would be relevant to any Hall bar measurement, ionic gating seems to be especially sensitive to geometry. To improve contact geometry, the size of the contacts should be reduced as much as possible, and the alignment of the contacts used to measure the Hall coefficient should be as precise as possible. This can be done using spot welding, in which a voltage is discharged over a wire to weld it directly to the sample. [195, 196] In contrast to Ti/Au contacts and silver paste, which have sizes of about 200 μm by 200 μm, spot welding would yield contacts that are just larger than the diameter of the wire used for the lead.

Since all the ionic gating results currently obtained were performed on the same sample, it would be useful to compare results on different samples. To extend the work presented in Chapter 5, where floating zone samples are found to host bulk conduction below 5 K, it would be especially interesting to perform ionic gating measurements on a floating zone sample to test whether the surface characteristics differ significantly from the flux grown sample from Chapter 6. This type of result would be of interest to the wider SmB_6 community, as there is ongoing debate about ARPES and dHvA results compared between flux and floating zone grown samples.

7.2.2 The role of impurities

Impurities, both magnetic and nonmagnetic, have been a recent subject of interest in the SmB_6 community. In light of the new bulk conduction channel below 5 K, a systematic study of impurities and their effect on low-temperature conduction is a clear future direction. Also, impurities have been used to explain everything from the resistance plateau [3] to the presence of dHvA oscillations. [27, 91, 102] Recent work has also suggested that impurities play a role in the topology of SmB_6 [104] and may have a significant affect on thermal transport at low temperatures. [197] Magnetic impurities are of particular interest as recent work has demonstrated that they can screen local moments, perhaps disrupting the Kondo effect and

leading to novel magnetic properties that have not yet been fully probed. [102]

Drawing from this, Ref. [197] demonstrates that magnetic impurities affect the thermal properties of SmB_6 at low temperatures. This work also suggests that purifying SmB_6 isotopically is a good way to reduce rare earth impurities in SmB_6. However, other work from Ref. [91] indicates that impurities are not a significant effect in their studies of thermal transport and dHvA oscillations. One way to resolve this could be by performing dHvA oscillation studies on isotopically purified SmB_6.

In addition to point impurities, dislocations and other material defects are another direction of future study. The work presented in Chapter 5 is the first exploration of dislocations in SmB_6, so there is significant opportunity for future work. Other material defects, like grain boundaries, polycrystals, and twin crystals, could play a role in some SmB_6 samples, and these would also be interesting to study systematically.

Besides expanding etching studies to better understand the variation of dislocation density between samples, it would be interesting to study the properties of an individual dislocation. To do this, the dislocation could be identified using etching and then cut out of the larger sample using the focused ion beam technique introduced in Chapter 2. Placing a Corbino disk on the dislocation would allow the transport characteristics of the dislocation to be studied. Alternatively, the focused ion beam could be used to cut out a dislocation-free region of the sample, and its properties could be compared to that of a sample that includes dislocations.

7.2.3 Other open questions

A few of the remaining open questions in SmB_6 were briefly discussed in the introduction, but many more remain. Electrical transport has been discussed at length in this dissertation, but magnetotransport and transport under pressure have not been investigated as deeply. One mystery in magnetotransport is why the magnetoresistance is negative at all temperatures measured. It would normally be expected to be positive for a metal (below 4 K in SmB_6), but this is not seen.

It would additionally be interesting to revisit pressure measurements in SmB_6. Pressure was previously studied to investigate whether SmB_6 is a Kondo insulator. [198, 10] Now that

more is known about SmB_6, the effects of pressure on the various conduction channels could be a new area of study. For example, the effect of pressure on the surface conductivity or on the surface carrier density and mobility would be an interesting topic of study. Alternatively, the effect of pressure on the low-temperature bulk conduction channel could be another area of study. Related to pressure, one study [199] was performed on SmB_6 under strain, and it would be interesting to test whether those results are reproducible.

Spectroscopic results also leave room for future work. For example, discussions of ARPES results seem to have stalled on the (001) surface, but STM and related methods are still being used. The role of surface polarity and reconstructions has been investigated in STM, and a recent quasiparticle interference study showed Dirac cones at the Γ and X points on the (001) surface. [79] However, the (111) crystal surface may be even more promising. This surface can be cleaved in situ, it is nonpolar so it does not form reconstructions, and one study has shown evidence for an odd number of Dirac cones and spin momentum locking. [78] Could the (111) surface, which has not been extensively studied, be the key to understanding surface conduction in SmB_6?

An obvious open question is to work towards resolving quantum oscillations, specifically finding the origin of the de Haas-van Alphen oscillations and why results seem to differ between Al flux and floating zone grown samples. One experimental possibility moving forward is to measure dHvA on an isotopically purified floating zone sample to test if it matches more closely with the flux sample results. More mysterious in quantum oscillations is why Shubnikov-de Haas oscillations have not yet been seen in SmB_6.

Results from transport, ARPES, and dHvA were the primary methods considered in this dissertation, but a huge amount of other work on SmB_6 exists. For example, ac transport results have been performed, [200, 201] and they do not agree with dc transport in the relevant limits. It is still unknown why this occurs. Additionally, Raman spectroscopy has been used to study phonon modes in SmB_6, [202, 203] but it is unclear how these fit in with other results. Inelastic neutron scattering has also been studied for some time, and one distinct signature is a 14 meV magnetic mode within the gap of SmB_6. [204] This mode seems to be well-understood in isolation, but it is still not clear if it should be related to in-gap impurity states or topological surface states. These are not the only methods used to

test SmB_6, however, and there is still room for significant and creative breakthroughs before a complete understanding of this material is reached.

Bibliography

[1] E. E. Vainshtein, S. M. Blokhin, and Yu. B. Paderno. X-ray spectral investigation of samarium hexaboride. *Soviet Physics - Solid State*, 6:2318, 1965.

[2] Yu. B. Paderno, V. I. Novikov, and E. S. Garf. Electrical properties of hexaborides of the alkaline- and rare-earth metals at low temperatures. *Poroshkovaya Metallurgiya*, 11(83):70–73, 1969.

[3] A. Menth, E. Buehler, and T. H. Geballe. Magnetic and semiconducting properties of SmB_6. *Physical Review Letters*, 22(7):295, 1969.

[4] J.-N. Chazalviel, M Campagna, G. K. Wertheim, and P. H. Schmidt. Study of valence mixing in SmB_6 by x-ray photoelectron spectroscopy. *Physical Review B*, 14(10):4586, 1976.

[5] R. L. Cohen, M. Eibschutz, and K. W. West. Electronic and magnetic structure of SmB_6. *Physical Review Letters*, 24(8):383, 1970.

[6] G. Aeppli and Z. Fisk. Kondo Insulators. *Comments Cond. Mat. Phys.*, 16(3):155–165, 1992.

[7] J. Kondo. Resistance minimum in dilute magnetic alloys. *Progress of Theoretical Physics*, 32:37, 1964.

[8] N. F. Mott. Rare earth compounds with mixed valencies. *Philosophical Magazine*, 30(2):403, 1974.

[9] J. W. Allen, B. Batlogg, and P. Wachter. Large low-temperature Hall effect and resistivity in mixed-valent SmB_6. *Physical Review B*, 20:4807, 1979.

[10] J. C. Cooley, M. C. Aronson, Z. Fisk, and P. C. Canfield. SmB_6: Kondo Insulator or Exotic Metal? *Physical Review Letters*, 74(9):1629, 1995.

[11] M. C. Hatnean, M. R. Lees, D. McK. Paul, and G. Balakrishnan. Large, high quality single-crystals of the new topological Kondo insulator, SmB_6. *Scientific Reports*, 3:307, 2013.

[12] M. Dzero, K. Sun, V. Galitski, and P. Coleman. Topological Kondo insulators. *Physical Review Letters*, 104:106408, 2010.

[13] T. Takimoto. SmB_6: A promising candidate for a topological insulator. *Journal of the Physical Society of Japan*, 80:123710, 2011.

[14] M. Dzero, K. Sun, P. Coleman, and V. Galitski. Theory of topological Kondo insulators. *Physical Review B*, 85:045130, 2012.

[15] S. Wolgast, Ç. Kurdak, K. Sun, J. W. Allen, D.-J. Kim, and Z. Fisk. Low-temperature surface conduction in the Kondo insulator SmB_6. *Physical Review B*, 88:180405(R), 2013.

[16] D. J. Kim, S. Thomas, T. Grant, J. Botimer, Z. Fisk, and J. Xia. Surface Hall effect and nonlocal transport in SmB_6: evidence for surface conduction. *Scientific Reports*, 3:3150, 2013.

[17] D. J. Kim, J. Xia, and Z. Fisk. Topological surface state in the Kondo insulator samarium hexaboride. *Scientific Reports*, 13:466, 2014.

[18] P. Syers, D. Kim, M. S. Fuhrer, and J. Paglione. Tuning bulk and surface conduction in the proposed topological Kondo insulator SmB_6. *Physical Review Letters*, 114:096601, 2015.

[19] M. Neupane, N. Alidoust, S.-Y. Xu, T. Kondo, Y. Ishida, D. J. Kim, Chang Liu, I. Belopolski, Y. J. Jo, T.-R. Chang, H.-T. Jeng, T. Durakiewicz, L. Balicas, H. Lin, A. Bansil, S. Shin, Z. Fisk, and M. Z. Hasan. Surface electronic structure of the

topological Kondo insulator candidate correlated electron system SmB_6. *Nature Communications*, 4:2991, 2013.

[20] J. Jiang, S. Li, T. Zhang, Z. Sun, F. Chen, Z. R. Ye, M. Xu, Q. Q. Ge, S. Y. Tan, X. H. Niu, M. Xia, B. P. Xie, Y. F. Li, X. H. Chen, H. H. Wen, and D. L. Feng. Observation of possible topological in-gap surface states in the Kondo insulator SmB_6 by photoemission. *Nature Communications*, 4:3010, 2013.

[21] N. Xu, P. K. Biswas, J. H. Dil, R. S. Dhaka, G. Landolt, S. Muff, C. E. Matt, X. Shi, N. C. Plumb, M. Radovic, E. Pomjakushina, K. Conder, A. Amato, S. V. Borisenko, R. Yu, H. M. Weng, Z. Fang, X. Dai, J. Mesot, H. Ding, and M. Shi. Direct observation of the spin texture in SmB_6 as evidence of the topological Kondo insulator. *Nature Communications*, 5:4566, 2014.

[22] J. D. Denlinger, J. W. Allen, J.-S. Kang, K. Sun, J.-W. Kim, J. H. Shim, B. I. Min, Dae-Jeong Kim, and Z. Fisk. Temperature dependence of linked gap and surface state evolution in the mixed valent topological insulator SmB_6, 2014. arXiv:1312.6637 [cond-mat.str-el].

[23] E. Frantzeskakis, N. de Jong, B. Zwartsenberg, Y. K. Huang, Y. Pan, X. Zhang, J. X. Zhang, F. X. Zhang, L. H. Bao, O. Tegus, A. Varykhalov, A. de Visser, and M. S. Golden. Kondo hybridization and the origin of metallic states at the (001) surface of SmB_6. *Physical Review X*, 3:041024, 2013.

[24] P. Hlawenka, K. Siemensmeyer, E. Weschke, A. Varykhalov, J. Sánchez-Barriga, N. Y. Shitsevalova, A. V. Dukhnenko, V. B. Filipov, S. Gabáni, K. Flachbart, O. Rader, and E. D. L. Rienks. Samarium hexaboride is a trivial surface conductor. *Nature Communications*, 9:517, 2018.

[25] H. Hermann, P. Hlawenka, K. Siemensmeier, E. Weschke, J. Sánchez-Barriga, A. Varykhalov, N. Y. Shitsevalova, A. V. Dukhnenko, V. B. Filipov, S. Gabáni, K. Flachbart, O. Rader, M. Sterrer, and E. D. L. Rienks. Contrast reversal in scanning tunneling microscopy and its implications for the topological classification of SmB_6. *Advanced Materials*, 32:1906725, 2020.

[26] B. S. Tan, Y.-T. Hsu, B. Zeng, M. Ciomaga Hatnean, N. Harrison, Z. Zhu, M. Hartstein, M. Kiourlappou, A. Srivastava, M. D. Johannes, T. P. Murphy, J.-H. Park, L. Balicas, G. G. Lonzarich, G. Balakrishnan, and S. E. Sebastian. Unconventional Fermi surface in an insulating state. *Science*, 349:6245, 2015.

[27] M. Hartstein, W. H. Toews, Y.-T. Hsu, B.Zeng, X. Chen, M. C. Hatnean, Q. R. Zhang, S. Nakamura, A. S. Padgett, G. Rodway-Gant, J. Berk, M. K. Kingston, G. H. Zhang, M. K. Chan, S. Yamashita, T. Sakakibara, Y. Tanako, J.-H. Park, L. Balicas, N. Harrison, N. Shitsevalova, G. Balakrishnan, G. G. Lonzarich, R. W. Hill, M. Sutherland, and S. E. Sebastian. Fermi surface in the absence of a Fermi liquid in the Kondo insulator SmB_6. *Nature Physics*, 14:166, 2017.

[28] H. C. Longuet-Higgins and M. de V. Roberts. The electronic structure of the borides MB_6. *Proceedings of the Royal Society A*, 224(1158):336–347, 1954.

[29] S. von Molnar, T. Theis, A. Benoit, A. Briggs, J. Flouquet, J. Ravex, and Z. Fisk. Study of the energy gap in single crystal SmB_6. In P. Wachter and H. Boppart, editors, *Valence Fluctuations*, page 389. North-Holland Publishing Company, 1982.

[30] Yu. B. Paderno, S. Pokrzywnicki, and B Stalinski. Magnetic properties of some rare earth hexaborides. *Phys. Stat. Sol.*, 24:K73–K76, 1967.

[31] J. C. Nickerson, R. M. White, K. N. Lee, R. Bachmann, T. H. Geballe, and G. W. Hull, Jr. Physical Properties of SmB_6. *Physical Review B*, 3(6):2030, 1971.

[32] V. V. Glushkov, A. V. Kuznetsov, O. A. Churkin, S. V. Demishev, Yu. B. Paderno, N. Yu. Shitsevalova, and N. E. Sluchanko. Spin gap formation in SmB_6. *Physica B*, 378-380:614–615, 2006.

[33] S. Yeo, K. Song, N. Hur, Z. Fisk, and P. Schlottmann. Effects of Eu doping on SmB_6 single crystals. *Physical Review B*, 85:115125, 2012.

[34] J. W. Allen and R. M. Martin. Surface mixed valence in Sm and SmB_6. *Physical Review B*, 21(4):1335, 1980.

[35] C. M. Varma. Mixed-valence compounds. *Reviews of Modern Physics*, 48:219, 1976.

[36] M. B. Maple and D. Wohlleben. Nonmagnetic 4f shell in the high-pressure phase of SmS. *Physical Review Letters*, 27:511, 1971.

[37] F. Lapierre, M. Ribault, F. Holtzberg, and J. Flouquet. New states in SmS? *Solid State Communications*, 40:347, 1981.

[38] G. K. Wertheim, W. Eib, E. Kaldis, and M. Campagna. Mixed valency of TmSe. *Physical Review B*, 22:6240, 1980.

[39] E. Beaurepaire, J. P. Kappler, and G. Krill. X-ray-absorption near-edge structure study in mixed-valent samarium systems. *Physical Review B*, 41(10):6768, 1990.

[40] T. Kasuya, K. Kojima, and M. Kasaya. Theory and experiment on SmB_6. In R. D. Parks, editor, *Valence Instabilities and Related Narrow-Band Phenomena*, page 137. Plenum Press, 1977.

[41] M. Kasaya, J. M. Tarascon, and J. Etourneau. Study of the valence transition in La- and Yb-substituted SmB_6. *Solid State Communications*, 33:1005–1007, 1980.

[42] J. M. Tarascon, Y. Isikawa, B. Chevalier, J. Etourneau, P. Hagenmuller, and M. Kasaya. Valence transition of samarium in hexaboride solid solutions $Sm_{1-x}M_xB_6$ (M = Yb^{2+}, Sr^{2+}, La^{3+}, Y^{3+}, Th^{4+}. *J. Physique*, 51:3877, 1980.

[43] I. V. Berman, N. B. Brandt, V. V. Moschalkov, S. N. Pashkevich, V. I. Sidorov, E. S. Konovalova, and Yu. B.Paderno. Effect of pressure on the correlation gap in a compound with intermediate valency SmB_6. *JETP Letters*, 38:477, 1983.

[44] N. P. Butch, J. Paglione, P. Chow, Y. Xiao, C. A. Marianetti, C. H. Booth, and J. R. Jeffries. Pressure-resistant intermediate valence in the Kondo insulator SmB_6. *Physical Review Letters*, 116:156401, 2016.

[45] J. Beille, M. B. Maple, J. Wittig, Z. Fisk, and L. E. DeLong. Suppression of the energy gap in SmB_6 under pressure. *Mat. Res. Bull*, 28(12):7397, 1983.

[46] Y. Zhou, Q. Wu, P. F. S. Rosa, R. Yu, J. Guo, W. Yi, S. Zhang, Z. Wang, H. Wang, S. Cai, K. Yang, A. Li, Z. Jiango, S. Zhang, X. Wei, Y. Huang, Y. Yang, Z. Fisk, Q. Si, L. Sun, and Z. Zhao. Quantum phase transition and destruction of Kondo effect in pressurized SmB_6. *Science Bulletin*, page 1439, 2017.

[47] T. Kasuya, K. Takegahara, Y. Aoki, K. Hanzawa, M. Kasaya, S. Kunii, T. Fujita, N. Sato, H. Kimura, T. Komatsubara, T. Furuno, and J. Rossat-Mignod. Anomalous properties of valence fluctuating CeB_6 and SmB_6. In L.M. Falicov, W. Hanke, and M.B. Maple, editors, *Valence Fluctuations in Solids*, page 215. North-Holland Publishing Company, 1981.

[48] S. Nozawa, T. Tsukamoto, K. Kanai, T. Haruna, S. Shin, and S. Kunii. Ultrahigh-resolution and angle-resolved photoemission study of SmB_6. *Journal of Physics and Chemistry of Solids*, 63:1223–1226, 2002.

[49] S. Souma, H. Kumigashira, T. Ito, T. Takahashi, and S. Kunii. Direct observation of pseudogap of SmB_6 using ultrahigh-resolution photoemission spectroscopy. *Physica B*, 312-313:329–330, 2002.

[50] H. Miyazaki, T. Hajiri, T. Ito, S. Kunii, and S. Kimura. Momentum-dependent hybridization gap and dispersive in-gap state of the Kondo semiconductor SmB_6. *Physical Review B*, 86:075105, 2012.

[51] A. Barla, J. Derr, J. P. Sanchez, B. Salce, G. Lapertot, B. P. Doyle, R. Ruffer, R. Lengsdorf, M. M. Abd-Elmeguid, and J. Flouquet. High-Pressure Ground State of SmB_6: Electronic Conduction and Long Range Magnetic Order. *Physical Review Letters*, 94:166401, 2005.

[52] J. Derr, G. Knebel, D. Braithwaite, B. Salce, J. Flouquet, K. Flachbart, S. Gabani, and N. Shitsevalova. From unconventional insulating behavior towards conventional magnetism in the intermediate-valence compound SmB_6. *Physical Review B*, 77:193107, 2008.

[53] A. Lacerda, D. Rickel, M. F. Hundley, P. C. Canfield, J. D. Thompson, Z. Fisk, P. Haen, and F. Lapierre. High field magnetoresistance in SmB_6. *Physica B*, 199-200:469–470, 1994.

[54] J. C. Cooley, M. C. Aronson, A. Lacerda, Z. Fisk, P. C. Canfield, and R. P. Guertin. High magnetic fields and the correlation gap in SmB_6. *Physical Review B*, 52(10):7322, 1995.

[55] Y. Nakajima, P. Syers, X. Wang, R. Wang, and J. Paglione. One-dimensional edge state transport in a topological Kondo insulator. *Nature Physics*, 12:213, 2015.

[56] S. Wolgast, Y. S. Eo, T. Ozturk, G. Li, Z. Xiang, C. Tinsman, T. Asaba, B. Lawson, F. Yu, J. W. Allen, K. Sun, L. Li, Ç. Kurdak, D.-J. Kim, and Z. Fisk. Magnetotransport measurements of the surface states of samarium hexaboride using Corbino structures. *Physical Review B*, 92:115110, 2015.

[57] J. C. Cooley, C. H. Mielke, W. L. Hults, J. D. Goettee, M. M. Honold, R. M. Modler, A Lacerda, D. G. Rickel, and J. L. Smith. High field gap closure in the Kondo insulator SmB_6. *Journal of Superconductivity*, 12(1):7322, 1999.

[58] K. Flachbart, S. Gabáni, E. Konovalova, Y. Paderno, and V. Pavlik. Pulsed magnetic field study of the spin gap in intermediate-valent SmB_6. *Physica B*, 404:2985–2987, 2009.

[59] K. v. Klitzing, G. Dorda, and M. Pepper. New Method for Hihg-Accuracy Determination of the Fine-Structure Constant Based on Quantized Hall Resistance. *Physical Review Letters*, 45:494, 1980.

[60] D. J. Thouless, M. Kohmoto, M. P Nightingale, and M. den Nijs. Fractionalized Fermi liquid on the surface of a topological Kondo insulator. *Physical Review Letters*, 49:405, 1982.

[61] C. L. Kane and E. J. Mele. Quantum spin Hall effect in graphene. *Physical Review Letters*, 95:226801, 2005.

[62] C. L. Kane and E. J. Mele. Z_2 topological order and the quantum spin Hall effect. *Physical Review Letters*, 95:146802, 2005.

[63] B. A. Bernevig, T. L. Hughes, and S.-C. Zhang. Quantum spin Hall effect and topological phase transition in HgTe quantum wells. *Science*, 314(5806):1757, 2006.

[64] M. Konig and S. Wiedmann and C. Brune and A. Roth and H. Buhmann and L. W. Molenkamp and X.-L. Qi and S.-C. Zhang. Quantum spin Hall insulator state in HgTe quantum wells. *Science*, 318(5851):766, 2007.

[65] L. Fu, C. L. Kane, and G. Mele. Topological insulators in three dimensions. *Physical Review Letters*, 98:106803, 2007.

[66] J. E. Moore and L. Balents. Topological invariants of time-reversal-invariant band structures. *Physical Review B*, 75:121306, 2007.

[67] L. Fu and C. L. Kane. Topological insulators with inversion symmetry. *Physical Review B*, 76:045302, 2007.

[68] M. Z. Hasan and C. L. Kane. Topological Insulators. *Reviews of Modern Physics*, 82:3045, 2010.

[69] Y. Ando. Topological Insulator Materials. *Journal of the Physical Society of Japan*, 82:102001, 2013.

[70] F. Lu, J. Zhao, H. Weng, Z. Fang, and X. Dai. Correlated topological insulators with mixed valence. *Physical Review Letters*, 110:096401, 2013.

[71] J. D. Denlinger, J. W. Allen, J.-S. Kang, K. Sun, B. I. Min, Dae-Jeong Kim, and Z. Fisk. SmB_6 Photoemission: Past and Present. In *Proceedings of the International Conference on Strongly Correlated Electron Systems*, volume 3, page 017038. JPS, 2014.

[72] J. D. Denlinger, S. Jang, G. Li, L. Chen, B. J. Lawson, T. Asaba, C. Tinsman, F. Yu, K. Sun, J. W. Allen, Ç. Kurdak, D.-J. Kim, Z. Fisk, and L. Li. Consistency of photoe-

mission and quantum oscillations for surface states of SmB_6, 2016. arXiv:1601.07408 [cond-mat.str-el].

[73] Z.H. Zhu, Z. Nicolaou, G. Levy, N. P. Butch, P. Syers, X. F. Wang, J. Paglione, G. A. Sawatzky, I. S. Elfimov, and A. Damascelli. Polarity-driven surface metallicity in SmB_6. *Physical Review Letters*, 111:216402, 2013.

[74] M. M. Yee, Y. He, A. Soumyanarayanan, D.-J. Kim, Z. Fisk, and J. E. Hoffman. Imaging the Kondo insulating gap on SmB_6, 2013. arXiv:1308.1085 [cond-mat.str-el].

[75] S. Rößler, T.-H. Jang, D.-J. Kim, L. H. Tjeng, Z. Fisk, F. Steglich, and S. Wirth. Hybridization gap and Fano resonance in SmB_6. *Proc. Natl. Acad. Sci. USA*, 111:4798, 2014.

[76] S. Rößler, L. Jiao, D.-J. Kim, S. Seiro, K. Rasim, F. Steglich, L. H. Tjeng, Z. Fisk, and S. Wirth. Surface and electronic structure of SmB_6 through scanning tunneling microscopy. *Philosophical Magazine*, 96(31):3262–3273, 2016.

[77] C. E. Matt, H. Pirie, A. Soumyanarayanan, M. M. Yee, Y. He, D. T. Larson, W. S. Paz, J. J. Palacios, M. H. Hamidian, and J. E. Hoffman. Consistency between ARPES and STM measurements on SmB_6. *Physical Review B*, 101:085142, 2020.

[78] Y. Ohtsubo, Y. Yamashita, K. Hagiwara, S. Ideta, K. Tanaka, R. Yukawa, K. Horiba, H. Kumigashira, K. Miyamoto, T. Okuda, W. Hirano, F. Iga, and S. Kimura. Non-trivial surface states of samarium hexaboride at the (111) surface. *Nature Communications*, 10:2298, 2019.

[79] H. Pirie, Y. Liu, A. Soumyanarayanan, P. Chen, Y. He, M. M. Yee, P. F. S. Rosa, J. D. Thompson, D.-J. Kim, Z. Fisk, X. Wang, J. Paglione, D. K. Morr, M. H. Hamidian, and J. E. Hoffmann. Imaging emergent heavy Dirac fermions of a topological Kondo insulator. *Nature Physics*, 16:52, 2020.

[80] Q. Song, J. Mi, D. Zhao, T. Su, W. Yuan, W. Xing, Y. Chen, T. Wang, T. Wu, X. H. Chen, X. C. Xie, C. Zhang, J. Shi, and W. Han. Spin injection and inverse

Edelstein effect in the surface states of topological Kondo insulator SmB_6. *Nature Communications*, 7:13485, 2016.

[81] S. Thomas, D. J. Kim, S. B. Chung, T. Grant, Z. Fisk, and J. Xia. Weak antilocalization and linear magnetoresistance in the surface state of SmB_6. *Physical Review B*, 94:205114, 2016.

[82] S. Biswas, R. Nagarajan, S. Sarkar, K. R. Amin, M. C. Hatnean, S. Tewari, G. Balakrishnan, and A. Bid. Robust local and nonlocal transport in the topological Kondo insulator SmB_6 in the presence of a high magnetic field. *Physical Review B*, 92:085103, 2015.

[83] F. Chen, C. Shang, Z. Jin, D. Zhao, Y. P. Wu, Z. J. Xiang, Z. C. Xia, A. F. Wang, X. G. Luo, T. Wu, and X. H. Chen. Magnetoresistance evidence of a surface state and a field-dependent insulating state in the Kondo insulator SmB_6. *Physical Review B*, 91:205133, 2015.

[84] M. Shahrokhvand, S. Pezzini, M. R. van Delft, U. Zeitler, N. E. Hussey, and S. Wiedmann. Bulk and in-gap states in SmB_6 revealed by high-field magnetotransport. *Physical Review B*, 96:205125, 2017.

[85] G. Li, Z. Xiang, F. Yu, T. Asaba, B. Lawson, P. Cai, C. Tinsman, A. Berkley, S. Wolgast, Y. S. Eo, D.-J. Kim, C. Kurdak, J. W. Allen, K. Sun, X. H. Cheng, Y. Y. Wang, Z. Fisk, and L. Li. Two-dimensional Fermi surfaces in Kondo insulator SmB_6. *Science*, 346:1208, 2014.

[86] Z. Xiang, B. Lawson, T. Asaba, C. Tinsman, L. Chen, C. Shang, X. H. Chen, and L. Li. Bulk rotational symmetry breaking in Kondo insulator SmB_6. *Physical Review X*, 7:031054, 2017.

[87] S. Gabáni, K. Flachbart, E. Konovalova, M. Orendáč, Y. Paderno, V. Pavlík, and J. Šebek. Properties of the in-gap states in SmB_6. *Solid State Communications*, 117:641–644, 2001.

[88] Y. Xu, S. Cui, J. K. Dong, D. Zhao, T. Wu, X. H. Chen, K. Sun, H. Yao, and S. Y. Li. Bulk Fermi surface of charge-neutral excitations in SmB_6 or not: a heat-transport study. *Physical Review Letters*, 116:246403, 2016.

[89] M.-E. Boulanger, F. Laliberté, M. Dion, S. Badoux, N. Doiron-Leyraud, W. A. Phelan, S. M. Koohpayeh, W. T. Fuhrman, J. R. Chamorro, T. M. McQueen, X. F. Wang, Y. Nakajima, T. Metz, J. Paglione, and L. Taillefer. Field-dependent heat transport in the topological Kondo insulator SmB_6: Phonons scattered by magnetic impurities. *Physical Review B*, 97:245141, 2018.

[90] S. M. Thomas, X. Ding, F. Ronning, V. Zapf, J. D. Thompson, Z. Fisk, J. Xia, and P. F. S. Rosa. Quantum oscillations in flux-grown SmB_6 with embedded aluminum. *Physical Review Letters*, 122:166401, 2019.

[91] M. Hartstein, H. Liu, Y.-T. Hsu, B. S. Tan, M. Ciomaga Hatnean, G. Balakrishnan, and S. E. Sebastian. Intrinsic bulk quantum oscillations in a bulk unconventional insulator SmB_6. *iScience*, 23:101632,, 2020.

[92] J. Knolle and N. R. Cooper. Excitons in topological Kondo insulators: Theory of thermodynamic and transport anomalies in SmB_6. *Physical Review Letters*, 118:096604, 2017.

[93] D. Chowdhury, I. Sodemann, and T. Senthil. Mixed-valence insulators with neutral Fermi surfaces. *Nature Communications*, 9:1766, 2018.

[94] G. Baskaran. Majorana Fermi sea in insulating SmB_6: A proposal and a theory of quantum oscillations in Kondo insulators, 2015. arXiv:1507.03477v1 [cond-mat.str-el].

[95] O. Erten, P. Ghaemi, and P. Coleman. Kondo breakdown and quantum oscillations in SmB_6. *Physical Review Letters*, 116:046403, 2016.

[96] O. Erten, P. Ghaemi, and P. Coleman. Kondo breakdown and quantum oscillations in SmB_6. *Physical Review Letters*, 116:046403, 2016.

[97] P. S. Riseborough and Z. Fisk. Critical examination of quantum oscillations in SmB_6. *Physical Review B*, 96:195122, 2017.

[98] J. Knolle and N. R. Cooper. Quantum oscillations without a Fermi surface and the anomalous de Haas-van Alphen effect. *Physical Review Letters*, 115:146401, 2015.

[99] L. Zhang, X. Y. Song, and F. Wang. Quantum oscillation in narrow-gap topological insulators. *Physical Review Letters*, 116:046404, 2016.

[100] H. Shen and L. Fu. Quantum oscillation from in-gap states and a non-Hermitian Landau level problem. *Physical Review Letters*, 121:026403, 2018.

[101] N. Harrison. Highly asymmetric nodal semimetal in bulk SmB_6. *Physical Review Letters*, 121:026602, 2018.

[102] W. T. Fuhrman, J. R. Chamorro, P. A. Alekseev, J.-M. Mignot, T. Keller, J. A. Rodriguez-Rivera, Y. Qiu, P. Nikolić T. M. McQueen, and C. Broholm. Screened moments and extrinsic in-gap states in samarium hexaboride. *Nature Communications*, 9:1539, 2018.

[103] W. T. Fuhrman and P. Nikolić. Magnetic impurities in Kondo insulators and the puzzle of samarium hexaboride, 2018. arXiv:1807.00005v1 [cond-mat.str-el].

[104] M. Abele, X. Yuan, and P. S. Riseborough. Topological nonmagnetic impurity states in topological Kondo insulators. *Physical Review B*, 101:094101, 2020.

[105] B. Skinner. Properties of the donor impurity band in mixed valence insulators. *Physical Review Materials*, 3:104601, 2019.

[106] S. Wolgast, Y. S. Eo, K. Sun, L. Li, Ç. Kurdak, F. F. Balakirev, M. Jaime, D.-J. Kim, and Z. Fisk. Reduction of the low-temperature bulk gap in samarium hexaboride under high magnetic fields. *Physical Review B*, 95:245112, 2017.

[107] W. A. Phelan, S. M. Koohpayeh, P. Cottingham, J. A. Tutmaher, J. C. Leiner, M. D. Lumsden, C. M. Lavelle, X. P. Wang, C. Hoffmann, M. A. Siegler, N. Haldolaarachchige, D. P. Young, and T. M. McQueen. On the chemistry and physical

properties of flux and floating zone grown SmB_6 single crystals. *Scientific Reports*, 6:20860, 2016.

[108] P. C. Canfield and Z. Fisk. Growth of single crystals from metallic fluxes. *Philosophical Magazine B*, 65:6:1117, 1992.

[109] S. M. Koohpayeh, D. Fort, and J. S. Abell. The optical floating zone technique: A review of experimental procedures with special reference to oxides. *Progress in Crystal Growth and Characterization of Materials*, 54:121–137, 2008.

[110] Y. S. Eo, A. Rakoski, J. Lucien, D. Mihaliov, Ç. Kurdak, P. F. S. Rosa, and Z. Fisk. Transport gap in SmB_6 protected against disorder. *Proceedings of the National Academy of Sciences*, 116(26):12638, 2019.

[111] B. Gorshunov, N. Sluchanko, A. Volkov, M. Dressel, G. Knebel, A. Loidl, and S. Kunii. Low-energy electrodynamics of SmB_6. *Physical Review B*, 59(3):1808, 1999.

[112] X. Zhang, N. P. Butch, P. Syers, S. Ziemak, R. L. Greene, and J. Paglione. Hybridization, inter-ion correlation and surface states in the Kondo insulator SmB_6. *Physical Review X*, 3:011011, 2013.

[113] K. Flachbart, K. Gloos, E. Konovalova, Y. Paderno, M. Reiffers, P. Samuely, and P. Švec. The energy gap of intermediate-valent SmB_6 studied by point-contact spectroscopy. *Physical Review B*, 64:085104, 2001.

[114] M. Dressel, B. P. Gorshunov, N. E. Sluchanko, A. A. Volkov, B. Hendersen, G. Grüner, G. Knebel, A. Loidl, and S. Kunii. Dielectric response of SmB_6 in the millimeter wave range. *Phys. Stat. Solidi B*, 215:161, 1999.

[115] N. E. Sluchanko, V. V. Glushkov, B. P. Gorshunov, S. V. Demishev, M. V. Kondrin, A. A. Pronin, A. A. Volkov, A. K. Savchenko, G. Grüner, Y. Bruynseraede, V. V. Moshchalkov, and S. Kunii. Intragap states in SmB_6. *Physical Review B*, 61:9906, 2000.

[116] B. Amsler, Z. Fisk, J. L. Sarrao, S. von Molnar, M. W. Meisel, and F. Sharifi. Electron-tunneling studies of the hexaboride materials SmB_6, EuB_6, CeB_6, and SrB_6. *Physical Review B*, 57:8747, 1998.

[117] S. Gabáni, E. Bauer, S. Berger, K. Flachbart, Y. Paderno, C. Paul, V. Pavlík, and N. Shitsevalova. Pressure-induced Fermi liquid behavior in the Kondo insulator SmB_6: Possible transition through a quantum critical point. *Physical Review B*, 67:172406, 2003.

[118] Y. Zhou, P. F. S. Rosa, J. Guo, S. Cai, R. Yu, S. Jiang, K. Yang, A. Li, Q. Si, Q. Wu, Z. Fisk, and L. Sun. Hall coefficient diagnostics of surface state in pressurized SmB_6, 2019. arXiv:1909.13462 [cond-mat.str-el].

[119] P. Coleman. *Introduction to Many-Body Physics*. Cambridge University Press, 1 edition, 2015.

[120] W. T. Fuhrman, J. C. Leiner, J. W. Freeland, M. van Veenendaal, S. M. Koohpayeh, W. A. Phelan, T. M. McQueen, and C. Broholm. Diamagnetic Sm^{3+} in the topological Kondo insulator SmB_6. *Physical Review B*, 99:020401(R), 2019.

[121] J. C. Souza, P. F. S. Rosa, J. Sichelschmidt, M. Carlone, P. A. Venegas, M. O. Malcolms, P. M. Menegasso, R. R. Urbano, Z. Fisk, and P. G. Pagliuso. Metallic islands in the Kondo insulator SmB_6, 2020. arXiv:2010.03719 [cond-mat.str-el].

[122] S. Gabáni, M. Orendáč, G. Pristáš, E. Gažo, P. Diko, S. Piovarči, V. Glushkov, N. Sluchanko, A. Levchenko, N. Shitsevalova, and K. Flachbart. Transport properties of variously doped SmB_6. *Philosophical Magazine*, 96(31):3274–3283, 2016.

[123] J. Stankiewicz, M. Evangelisti, P. F. S. Rosa, P. Schlottmann, and Z. Fisk. Physical properties of Sm_xB_6 single crystals. *Physical Review B*, 99:045138, 2019.

[124] L. J. van der Pauw. A method of measuring specific resistivity and Hall effect of discs of arbitrary shape. *Philips Research Reports*, 13:1:1–9, 1958.

[125] O. M. Corbino. Azioni elettromagnetiche dovute agli ioni dei metalli deviati dalla traiettoria normale per effetto di un campo. *Nuovo Cimento*, 1:397, 1911.

[126] Y. S. Eo, K. Sun, Ç. Kurdak, D.-J. Kim, and Z. Fisk. Inverted resistance measurements as a method for characterizing the bulk and surface conductivities of three-dimensional topological insulators. *Physical Review Applied*, 9:044006, 2018.

[127] Y. S. Eo. *Surface and bulk transport of samarium hexaboride*. PhD thesis, University of Michigan, 2017.

[128] P. K. Liao, K. E. Spear, and M. E. Schlesinger. The B-Sm (boron-samarium) system. *Journal of Phase Equilibria*, 17(4):348, 1996.

[129] Z. Fisk, A. S. Cooper, P. H. Schmidt, and R. N. Castellano. Preparation and lattice parameter of the rare earth tetraborides. *Mat. Res. Bull*, 7:285–288, 1972.

[130] G. D. Sturgeon, J.-P. Mercurio, J. Etourneau, and P. Hagenmuller. Single crystals of SmB_6 for conductivity and other measurements. *Mat. Res. Bull*, 9:117–120, 1974.

[131] Y. Luo, H. Chen, J. Dai, Z. Xu, and J. D. Thompson. Heavy surface state in a possible topological Kondo insulator: Magnetothermoelectric transport on the (001) plane of SmB_6. *Physical Review B*, 91:075130, 2015.

[132] V. N. Gurin, M. M. Korsukova, S. P. Nikanorov, I. A. Smirnov, N. N. Stepanov, and S. G. Shulman. The preparation of single crystals of the rare earth borides by the solution method and a study of their properties. *Journal of the Less-Common Metals*, 67:115–123, 1979.

[133] G. I. Solovyev and K. E. Spear. Phase behavior in the Sm-B system. *J. Am. Chem. Soc*, 55:475, 1972.

[134] K. A. Gschneider and F. W. Calderwood. The Al-Sm (Aluminum-Samarium) System. *Bulletin of Alloy Phase Diagrams*, 10(1):37, 1989.

[135] S. Kimura and K. Kitamura. Floating zone crystal growth and phase equilibria: a review. *Journal of the American Ceramic Society*, 75(6):1440–46, 1992.

[136] Yu. B. Paderno and T. Lundstrom. On the homogeneity ranges of LaB_6, EuB_6, and SmB_6. *Acta Chemica Scandinavica A*, 37:609–616, 1983.

[137] A. Ourmazd. The electrical properties of dislocations in semiconductors. *Contemporary Physics*, 25:251, 1984.

[138] R. Hall and J. C. Bean. Misfit dislocations in lattice-mismatched epitaxial films. *Critical Reviews in Solid State and Material Sciences*, 17:507, 1992.

[139] D. Hull and D. J. Bacon. *Introduction to Dislocations*. Elsevier, Ltd., 5 edition, 2011.

[140] S. Wolgast, Y. S. Eo, Ç. Kurdak, D.-J. Kim, and Z. Fisk. Conduction through subsurface cracks in bulk topological insulators, 2015. arXiv:1506.08233 [cond-mat.str-el].

[141] A. Kebede, M. C. Aronson, C. M. Buford, P. C. Canfield, J. H. Cho, B. R. Coles, J. C. Cooley, J. Y. Coulter, Z. Fisk, J. D. Goettee, W. L. Hults, A. Lacerda, T. D. McLendon, P. Tiwari, and J. L. Smith. Studies of the correlated electron system SmB_6. *Physica B*, 223-224:256–259, 1996.

[142] N. I. Kato. Reducing focused ion beam damage to transmission electron microscopy samples. *Journal of Electron Microscopy*, 53(5):451, 2004.

[143] C. A. Volkert and A. M. Minor. Focused ion beam microscopy and micromachining. *Materials Research Society Bulletin*, 32:389, 2007.

[144] J. Mayer, L. A. Giannuzzi, T. Kamino, and J. Michael. TEM sample preparation and FIB-induced damage. *Materials Research Society Bulletin*, 32:400, 2007.

[145] A. Rakoski, Y. S. Eo, K. Sun, and Ç. Kurdak. Understanding low-temperature bulk transport in samarium hexaboride without relying on in-gap bulk states. *Physical Review B*, 95:195133, 2017.

[146] X.-L. Qi and S.-C. Zhang. Topological insulators and superconductors. *Reviews of Modern Physics*, 83:1057, 2011.

[147] S. M. Sze. *Semiconductor Devices Physics and Technology, 2nd ed.* John Wiley and Sons, 1985.

[148] W. Kohn. Effective mass theory in solids from a many-particle standpoint. *Physical Review*, 105:509, 1957.

[149] H. Ohta, R. Tanaka, M. Motokawa, S. Kunii, and T. Kasuya. Far-infrared transmission spectra of SmB_6. *Journal of the Physical Society of Japan*, 60:1391, 1991.

[150] T. Nanba, H. Ohta, M. Motokawa, S. Kimura, S. Kunii, and T. Kasuya. Gap state of SmB_6. *Physica B*, 186-188:440, 1993.

[151] G. Travaglini and P. Wachter. Intermediate-valent SmB_6 and the hybridization model: an optical study. *Physical Review B*, 29:893, 1984.

[152] N. E. Sluchanko, A. A. Volkov, V. V. Glushkov, B. P. Gorshunov, S. V. Demishev, M. V. Kondrin, A. A. Pronin, N. A. Samarin, Y. Bruynseraede, V. V. Moshchalkov, and S. Kunii. Nature of the low-temperature anomalies in the physical properties of the intermediate-valent compound SmB_6. *Journal of Experimental and Theoretical Physics*, 88:533, 1999.

[153] J. Stankiewicz, P. F. S. Rosa, P. Schlottmann, and Z. Fisk. Electrical transport properties of single-crystal CaB_6, SrB_6, and BaB_6. *Physical Review B*, 94:125141, 2016.

[154] J. Bardeen, L. N. Cooper, and J.R. Schreiffer. Theory of Superconductivity. *Physical Review*, 108(5):1175, 1957.

[155] M. A. Woolf and F. Reif. Effect of magnetic impurities on the density of states of superconductors. *Physical Review*, 137:557, 1965.

[156] V. Alexandrov, M. Dzero, and P. Coleman. Cubic topological insulators. *Physical Review Letters*, 111:226403, 2013.

[157] Y. Ishida, T. Otsu, T. Shimada, M. Okawa, Y. Kobayashi, F. Iga, T. Takabatake, and S. Shin. Emergent photovoltage on SmB_6 surface upon bulk-gap evolution revealed by pump-and-probe photoemission spectroscopy. *Scientific Reports*, 5:8160, 2015.

[158] V. Alexandrov, P. Coleman, and O. Erten. Cubic topological insulators. *Physical Review Letters*, 114:177202, 2015.

[159] R. Peters, T. Yoshida, H. Sakakibara, and N. Kawakami. Coexistence of light and heavy surface states in a topological multiband insulator. *Physical Review B*, 93:235159, 2016.

[160] J. M. Ziman. *Electrons and Phonons*. Oxford University Press, 1960.

[161] J. C. Cooley. *High Pressure Transport Measurements on the Rare Earth Systems SmB_6, $Ce_3Bi_4Pt_3$, and EuB_6*. PhD thesis, University of Michigan, 1997.

[162] M. Kasaya, H. Kimura, Y. Isikawa, T. Fujita, and T. Kasuya. Valence instabilities and electrical properties of the La- and Yb-substituted SmB_6. In L.M. Falicov, W. Hanke, and M.B. Maple, editors, *Valence Fluctuations in Solids*, page 251. North-Holland Publishing Company, 1981.

[163] R. Takahashi and S. Murakami. Thermoelectric transport in topological insulators. *Semiconductor Science and Technology*, 27:124005, 2012.

[164] A. Rakoski, Y. S. Eo, K. Sun, and Ç. Kurdak. Investigation of high-temperature bulk transport characteristics and skew scattering in samarium hexaboride. *Journal of Superconductivity and Novel Magnetism*, 33(1):265, 2020.

[165] A. Fert and P. M. Levy. Theory of the Hall effect in heavy fermion compounds. *Physical Review B*, 36(4):1907, 1987.

[166] P. Coleman, P. W. Anderson, and T. V. Ramakrishnan. Theory for the anomalous Hall constant of mixed-valence systems. *Physical Review Letters*, 55:414, 1985.

[167] H. Kontani and K. Yamada. Theory of anomalous Hall effect in heavy fermion system. *Journal of the Physical Society of Japan*, 63:2627, 1994.

[168] W. A. Phelan, S. M. Koohpayeh, P. Cottingham, J. W. Freeland, J. C. Leiner, C. L. Broholm, and T. M. McQueen. Correlation between bulk thermodynamic measurements and the low-temperature resistance plateau in SmB_6. *Physical Review X*, 4:031012, 2014.

[169] P. P. Debye and E. M. Conwell. Electrical properties of n-type germanium. *Physical Review*, 93:693, 1954.

[170] P. W. Chapman, O. N. Tufte, J. D. Zook, and D. Long. Electrical properties of heavily doped silicon. *Journal of Applied Physics*, 34:3291, 1963.

[171] H. Hamasaki, Y. Tokumoto, and K. Edagawa. Dislocation conduction in Bi-Sb topological insulators. *Applied Physics Letters*, 110:092105, 2017.

[172] Y. Ran, Y. Zhang, and A. Vishwanath. One-dimensional topologically protected modes in topological insulators with lattice dislocations. *Nature Physics*, 5:298, 2009.

[173] Y. S. Eo, S. Wolgast, A. Rakoski, D. Mihaliov, B. Y. Kang, M. S. Song, B. K. Cho, M. Ciomaga Hatnean, G. Balakrishnan, Z. Fisk, S. R. Saha, X. Wang, J. Paglione, and Ç. Kurdak. Comprehensive surface magnetotransport study of SmB_6. *Physical Review B*, 101:155109, 2020.

[174] K. Flachbart, S. Gabáni, E. Konovalova, Y. Paderno, and V. Pavlik. Ground state formation in intermediate-valent SmB_6. *Physica B*, 293:417–421, 2001.

[175] S. Gabáni, G. Pristás, I. Takaáčová, N. Sluchanko, K. Siemensmeyer, N. Shitsevalova, V. Filipov, and K. Flachbart. Surface and bulk components of electrical conductivity in the (presumably special topological) Kondo insulator SmB_6 at lowest temperatures. *Solid State Sciences*, 47:17, 2015.

[176] T. H. Geballe, A. Menth, E. Buehler, and G. W. Hull. Properties of SmB_6 doped with Eu and Gd. *Journal of Applied Physics*, 41:904, 1970.

[177] J. T. Ye, S. Inoue, K. Kobayashi, Y. Kasahara, H. T. Yuan, H. Shimotani, and Y. Iwasa. Liquid-gated interface superconductivity on an atomically flat film. *Nat. Mater.*, 9(2):125, 2010.

[178] T. Sato, S. Marukane, and T. Morinag. Ionic Liquids for the Electric Double Layer Capacitor Applications. In Scott Handy, editor, *Applications of Ionic Liquids in Science and Technology*, chapter 6. IntechOpen, 2011.

[179] D. M. McCann, M. Misek, K. V. Kamenev, and A. D. Huxley. Pressure-Temperature Phase Diagram of Ionic Liquid Dielectric DEME-TFSI. *Physics Procedia*, 75:252, 2015.

[180] H. Yuan, H. Shimotani, A. Tsukazaki, A. Ohtomo, M. Kawasaki, and Y. Iwasa. High-density carrier accumulation in ZnO field-effect transistors gated by electric double layers of ionic liquids. *Advanced Functional Materials*, 19:1046, 2009.

[181] A. Rakoski, S. Diez, H. Li, S. Keller, E. Ahmadi, and C. Kurdak. Electron transport in N-polar GaN-based heterostructures. *Applied Physics Letters*, 114:162102, 2019.

[182] S. Kolluri, S. Keller, S. P. DenBaars, and U. K. Mishra. N-polar AlGaN/GaN MIS-HEMTs on SiC with a 16.7 W/mm power density at 10 GHz using an Al_2O_3 based etch stop technology for the gate recess. *69th Annual Device Research Conference*, page 215, 2011.

[183] V. Zomorrodian, U. K. Mishra, and R. A. York. A high-efficiency class F MMIC power amplifier at 4.0 GHz using AlGaN/GaN HEMT technology. *IEEE Compound Semiconductor Integrated Circuit Symposium*, page 4, 2012.

[184] D. Denninghoff, J. Lu, E. Ahmadi, S. Keller, and U. K. Mishra. N-polar GaN/InAlN/AlGaN MIS-HEMTs with 1.89 S/mm extrinsic transconductance, 4 A/mm drain current, 204 GHz f T and 405 GHz f max. *71st Annual Device Research Conference*, 20:4807, 2013.

[185] S. Chowdhury and U. K. Mishra. Lateral and Vertical Transistors Using the AlGaN/GaN Heterostructure. *IEEE Trans. Electron Devices*, 60(10):3060, 2013.

[186] T. Palacios, A. Chakraborty, S. Heikman, S. Keller, S. P. DenBaars, and U. K. Mishra. AlGaN/GaN high electron mobility transistors with InGaN back-barriers. *IEEE Electron Device Letters*, 27(1):13, 2006.

[187] N. A. Fichtenbaum, T. E. Mates, S. Keller, S. P. DenBaars, and U. K. Mishra. Impurity incorporation in heteroepitaxial N-face and Ga-face GaN films grown by metalorganic chemical vapor deposition. *J. Cryst. Growth*, 310(6):1124, 2008.

[188] E. Arslan, S. Bütün, S. B. Lisesivdin, M. Kasap, S. Ozcelik, and E. Ozbay. The persistent photoconductivity effect in AlGaN/GaN heterostructures grown on sapphire and SiC substrates. *J. Appl. Phys.*, 103(10):103701, 2008.

[189] N. Biyikli, Ü. Özgür, X. Ni, Y. Fu, H. Morkoç, and Ç. Kurdak. Illumination and annealing characteristics of two-dimensional electron gas systems in metal-organic vapor-phase epitaxy grown $Al_xGa_{1x}N$/AlN/GaN heterostructures. *J. Appl. Phys.*, 100(10):103702, 2006.

[190] J. Z. Li, J. Y. Lin, H. X. Jiang, M. A. Khan, and Q. Chen. Persistent photoconductivity in a two-dimensional electron gas system formed by an AlGaN/GaN heterostructure. *J. Appl. Phys.*, 82(3):1227, 1998.

[191] X. Z. Dang, C. D. Wang, E. T. Yu, K. S. Boutros, and J. M. Redwing. Persistent photoconductivity and defect levels in n-type AlGaN/GaN heterostructures. *Appl. Phys. Lett.*, 72(21):2745, 1998.

[192] Ç. Kurdak, N Biyikli, Ü. Özgür, H. Morkoç, and V. I. Litvinov. Weak antilocalization and zero-field electron spin splitting in $Al_xGa_{1-x}N$/AlN/GaN heterostructures with a polarization-induced two-dimensional electron gas. *Phys. Rev. B*, 74(11):113308, 2006.

[193] H. Cheng, Ç. Kurdak, J. H. Leach, M. Wi, and H. Morkoç. Two-subband conduction in a gated high density InAlN/AlN/GaN heterostructure. *Appl. Phys. Lett.*, 97(11):112113, 2010.

[194] M. J. Manfra, L. N. Pfeiffer, K. W. West, H. L. Stormer, K. W. Baldwin, J. W. P. Hsu, D. V. Lang, and R. J. Molnar. High-mobility AlGaN/GaN heterostructures grown by molecular-beam epitaxy on GaN templates prepared by hydride vapor phase epitaxy. *Appl. Phys. Lett.*, 77:2888, 2000.

[195] I. R. Walker and C. J. Moss. Spot welder for making small electrical contacts. *Review of Scientific Instruments*, 69:2747, 1998.

[196] I. R. Walker and C. J. Moss. Further considerations on the preparation of small electrical contacts by spot welding. *Review of Scientific Instruments*, 71:2228, 2000.

[197] W. T. Fuhrman, J. R. Chamorro, P. Alekseev, J.-M. Mignot, T. Keller, P. Nikolić, T. M. McQueen, and C. Broholm. Screened moments in a Kondo insulator, 2017. arXiv:1707.03834 [cond-mat.str-el].

[198] J. C. Cooley, M. C. Aronson, Z. Fisk, and P. C. Canfield. High pressure insulator-metal transition in SmB_6. *Physica B*, 199-200:486–488, 1994.

[199] A. Stern, M. Dzero, V. M. Galitski, Z. Fisk, and J. Xia. Surface-dominated conduction up to 240 K in the Kondo insulator SmB_6 under strain. *Nature Materials*, 16:708–711, 2017.

[200] N. J. Laurita, C. M. Morris, S. M. Koohpayeh, P. F. S. Rosa, W. A. Phelan, Z. Fisk, T. M. McQueen, and N. P. Armitage. Anomalous 3D bulk AC conduction within the Kondo gap of SmB_6 single crystals. *Physical Review B*, 94:78, 2016.

[201] N. J. Laurita, C. M. Morris, S. M. Koohpayeh, W. A. Phelan, T. M. McQueen, and N. P. Armitage. Impurities or a neutral Fermi surface? A further examination of the low-energy ac optical conductivity of SmB_6. *Physica B*, 536:165154, 2018.

[202] I. Morke, V. Dvorák, and P. Wachter. Raman scattering in intermediate valent SmB_6. *Solid State Communications*, 40:331–334, 1981.

[203] T. H. Nguyen, T. M. H. Nguyen, B. Kang, B. Cho, M. Han, H. J. Choi, M. Kong, Y. Lee, and I. Yang. Raman spectroscopic evidence of impurity-induced structural distortion in SmB_6. *Journal of Raman Spectroscopy*, 50(11):1661, 2019.

[204] W. T. Fuhrman, J. Leiner, P. Nikolić, G. E. Granroth, M. B. Stone, M. D. Lumsden, L. DeBeer-Schmidtt, P. A. Alekseev, J.-M. Mignot, S. M. Mignot, S. M. Koohpayeh, P. Cottingham, W. A. Phelan, L. Schoop, T. M. Schoop, T. M. McQueen, and C. Broholm. Interaction driven subgap spin exciton in the Kondo insulator SmB_6. *Physical Review Letters*, 114:036401, 2015.